Abstract We review the physical properties, linear and nonlinear optical characteristics, and phase-matching configurations of BiB_3O_6 (BIBO), the first low-symmetry (monoclinic) inorganic nonlinear crystal that has found broad applications for frequency conversion of laser sources from the UV, across the visible, to the near-IR based on three-wave interactions. We describe in detail the most relevant optical properties that make this material an attractive candidate for nonlinear frequency conversion of laser light in general, and ultrafast femtosecond laser sources in particular. With special focus on ultrafast frequency conversion, characteristics such as group-velocity mismatch and spectral acceptance, parametric gain bandwidth, group-velocity dispersion, as well as angular acceptance and spatial walk-off are evaluated and optimum configurations for the attainment of maximum conversion efficiency, minimum pulse duration, and highest spatial beam quality are identified and compared with the most widely established alternative borate crystal, β-BaB_2O_4. Experimental results are presented on both parametric up- and down-conversion of femtosecond pulses, from the high-energy, low-repetition-rate (1 kHz) to the low-energy, high-repetition-rate (56–76 MHz) regime, demonstrating the unique versatility of BIBO for efficient frequency conversion of femtosecond pulses with broad tunability from 250 nm in the UV, throughout the visible, up to $\sim$3000 nm in the IR.

Photograph of a femtosecond synchronously pumped optical parametric oscillator (SPOPO) based on BiB_3O_6 emitting in the yellow region of the spectrum. Pumped near 400 nm in the blue by the second harmonic of a Kerr-lens mode-locked Ti:sapphire laser, the SPOPO can generate femtosecond pulses across the full visible range of 480–710 nm, from the blue-green, through to yellow, orange and red.

Femtosecond nonlinear frequency conversion based on BiB_3O_6

Valentin Petrov[1,*], *Masood Ghotbi*[1,2], *Omid Kokabee*[2], *Adolfo Esteban-Martin*[2], *Frank Noack*[1], *Alexander Gaydardzhiev*[1,3], *Ivaylo Nikolov*[3], *Pancho Tzankov*[1], *Ivan Buchvarov*[3], *Kentaro Miyata*[1,4], *Andrzej Majchrowski*[5], *Ivan V. Kityk*[6], *Fabian Rotermund*[1,7], *Edward Michalski*[5], *and Majid Ebrahim-Zadeh*[2,8]

[1] Max-Born-Institute for Nonlinear Optics and Ultrafast Spectroscopy, Max-Born-Str. 2A, 12489 Berlin, Germany
[2] ICFO – Institut de Ciencies Fotoniques, Mediterranean Technology Park, 08860 Castelldefels, Barcelona, Spain
[3] Department of Physics, Sofia University, 5 James Bourchier Blvd., 1164 Sofia, Bulgaria
[4] Chitose Institute of Science and Technology, 758-65 Bibi, Chitose, Hokkaido, 066-8655, Japan
[5] Institute of Applied Physics, Military University of Technology, 2 Kaliskiego Str., 00-908 Warsaw, Poland
[6] Chemical Department, Silesian Technological University, 9 M. Strzody, 44-100 Gliwice, Poland
[7] Division of Energy Systems Research, Ajou University, 443-749 Suwon, Republic of Korea
[8] Institucio Catalana de Recerca i Estudis Avancats (ICREA), Passeig Lluis Companys 23, 08010 Barcelona, Spain

Received: 25 November 2008, Revised: 3 March 2009, Accepted: 23 March 2009
Published online: 8 June 2009

Key words: Bismuth triborate, biaxial nonlinear crystals, monoclinic symmetry, phase matching, effective nonlinearity, three-wave interactions, spectral acceptance, parametric gain bandwidth, femtosecond pulses, second-harmonic generation, synchronously pumped optical parametric oscillators, optical parametric amplifiers, optical parametric generators, white-light continuum generation and amplification, pulse compression.

PACS: 42.65.Ky, 42.65.Re, 42.65.Yj, 42.70.Mp, 42.79.Nv

* Corresponding author: e-mail: petrov@mbi-berlin.de

1. Introduction

Coherent optical sources with femtosecond pulse duration and wide tunability are of considerable interest for a wide range of scientific and technological applications in time-resolved spectroscopy, nonlinear optical microscopy, frequency metrology, quantum optics, biotechnology, and nanoscience. However, despite tremendous progress in ultrafast laser technology, substantial portions of the optical spectrum from the ultraviolet (UV) to the infrared (IR) still remain inaccessible to conventional mode-locked laser sources and ultrafast amplifiers. The advent of novel vibronic laser gain media, most notably Ti:sapphire, has provided a new class of practical ultrafast solid-state lasers and amplifiers, but even in such cases the maximum spectral coverage available is limited to at best $\sim$ 300–400 nm. At the same time, the restricted availability of suitable solid-state laser gain materials has confined the wavelength coverage of existing ultrafast lasers and amplifiers, including Ti:sapphire, mainly to limited regions in the near-IR.

Nonlinear optical techniques based on frequency conversion of laser light in second-order nonlinear materials offer a highly effective method to expand the spectral range of existing laser sources. Optical second-harmonic generation (SHG) and sum-frequency generation (SFG) can provide spectral extension of laser sources to shorter wavelengths (up-conversion) while difference-frequency generation (DFG) can extend the spectral coverage to longer wavelengths (down-conversion). Optical parametric generators (OPG), optical parametric amplifiers (OPA), and optical parametric oscillators (OPO) are also down-conversion devices that can, on the other hand, provide widely tunable spectral coverage at longer wavelengths using fixed-frequency laser sources with limited or no intrinsic tuning capability. At the same time, the instantaneous nature of nonlinear gain allows frequency-conversion processes to retain the temporal characteristics of the input pump laser, hence enabling wavelength generation in all temporal regimes from continuous-wave (CW) to ultrafast femtosecond time scales by an appropriate choice of pump laser or amplifier. These properties make nonlinear frequency-conversion processes attractive and practical techniques for the generation of widely tunable radiation in spectral and temporal regions where existing lasers and amplifiers or alternative technologies are not available.

The vital element in any frequency-conversion process is the nonlinear optical crystal. Together with the pump source, it constitutes the essential ingredient in the practical development of any frequency conversion system. In the 1990s, the emergence of a new generation of birefringent nonlinear crystals for the UV, visible, and near-IR, primarily β-BaB_2O_4 (BBO), LiB_3O_5 (LBO) and $KTiOPO_4$ (KTP), with superior linear and nonlinear properties, provided new impetus for the advancement of frequency-conversion sources in these spectral regions. Combined with the availability of novel crystalline solid-state and fiber lasers and amplifiers with improved spectral and spatial coherence and high power, this led to practical development of new generations of frequency-conversion devices offering unprecedented performance capabilities and operating in all temporal regimes, from the CW to the femtosecond time scales. Subsequently, the advent of quasi-phase-matched ferroelectric nonlinear materials, such as periodically poled $LiNbO_3$ (PPLN) and KTP (PPKTP), and periodically poled stoichiometric $LiTaO_3$ (PPSLT), had a profound impact on the advancement of frequency-conversion sources, particularly in the low-intensity operating regimes. These developments have led to remarkable progress in frequency-conversion sources over the past two decades, vastly extending the wavelength range of existing laser sources to new regions from the UV and visible to the near-IR. Yet, in different device configurations and operating regimes, major limitations still exist and important challenges still remain, requiring the continued search for alternative new nonlinear materials, laser pump sources and innovative design concepts.

This review is devoted to one particular nonlinear material, bismuth triborate, BiB_3O_6 (BIBO), and more specifically to its unique properties and application potential in frequency conversion of ultrafast (femtosecond) laser pulses. BIBO offers large second-order optical nonlinearity, wide transparency from the UV to near-IR, flexible phase-matching and spectral properties, and high optical damage tolerance. It is also not hygroscopic and readily available in high optical quality, large size, and at low cost. Once the linear and nonlinear characteristics of BIBO were studied [1], a number of groups demonstrated a wide range of nonlinear frequency-conversion processes in different time scales.

In the CW regime, these include intracavity SHG of Nd:YAG lasers at 532 nm [2], Nd:YVO_4 lasers at 532 nm [3–5] and 542 nm [5], Nd:YAG lasers at 473 nm [6–11], Nd:$GdVO_4$ laser at 456 nm [12–14], Nd:YVO_4 laser at 671 nm [15], Nd:$YLiF_4$ laser at 661 nm [16], Ti:sapphire lasers at 423 nm [17], 392 and 405 nm [18, 19] as well as continuously tunable from 373 to 435 nm [20], optically pumped semiconductor disk laser at 529 nm [21], diode-pumped Rb vapour laser at 397.4 nm [22, 23], and from 425 to 489 nm with a singly resonant OPO based on PPSLT [24]; SHG in an enhancement cavity of diode lasers at 423 and 390 nm [25, 26] and of Ti:sapphire lasers at 384–425 nm [17, 27–30]; and intracavity SFG of dual-wavelength Nd:YVO_4 lasers at 593.5 nm [31, 32], 537 nm [5], and 491 nm [33]. Recently CW SHG at $\sim$ 491 nm has been demonstrated extracavity, using an Yb-doped single-mode fiber laser [34]. The advantages of BIBO in the CW regime include a high optical nonlinearity combined with the large angular acceptance and the small spatial walk-off, which are important under the conditions of tight focusing. Impressive conversion efficiencies have been achieved, such as 63% for SHG with respect to the intracavity power at 946 nm [6], and second-harmonic powers, for example 6.2 W at 456 nm [12] or $\sim$ 450 mW single frequency at 460 nm [24].

Pumping with powerful nanosecond pulses generally does not require tight focusing and issues such as angu-

lar acceptance or walk-off are not particularly critical, while lower effective nonlinearity can be compensated by using thicker crystals or smaller beam sizes if the damage threshold is sufficiently high. With BIBO this regime has been deployed for both up- and down-conversion processes: intracavity SHG has been studied at 532 nm with an acousto-optically Q-switched Nd:YVO_4 laser operating at 10–50 kHz [35], at 671 nm with similar lasers operating at 15–70 kHz [15] and 10.1 kHz [36]; extracavity SHG was demonstrated at 473 nm with passively Q-switched Nd:YAG lasers operating at up to $\sim$40 kHz [37, 38], at 375–480 nm with a gain-switched Ti:sapphire laser operating at 1 kHz [39], and between 450 and 495 nm with the signal wave of a 10-kHz OPO [40, 41]; extracavity third-harmonic generation (THG) has been studied at 355 nm with a Q-switched Nd:YVO_4 laser operating at 10 kHz [36] and at 374 nm with a Q-switched Nd:YAG laser operating at $\sim$6.5 kHz [42]; an OPO based on type-I interaction in BIBO was pumped at 532 nm to produce tunable radiation from 735.6 to 970 nm (signal) and 1180 to 1930 nm (idler) at 10 kHz repetition rate or at a reduced repetition rate of 10 Hz for increased output energy [43], efficient type-II interaction has also been reported for an OPO pumped at 532 nm with a resonated idler wave at 1215 nm and a repetition rate of 10 Hz [44], whereas a 1064-nm pumped noncritical OPO at 10 Hz was temperature tunable from 1.625 to 3.083 µm [45]. The high effective nonlinearity of BIBO has also led to high conversion efficiencies and powers with nanosecond pulses, including 59% for SHG at 671 nm [36] and 4.38 W at the same wavelength [15], 39% conversion efficiency for THG at 355 nm [36] and 48% efficiency with a total energy (signal plus idler) of 49.7 mJ for a 10-Hz OPO [43].

Picosecond experiments have also been performed for both up- and down-conversion processes. These include SHG at 532 nm using 35-ps long fundamental pulses at 10 Hz [2, 7, 46–50] and 25 Hz [51]; THG at 355 nm using the same pump sources [7, 51, 52]; SHG at 370–500 nm of the signal pulses of a BIBO based OPG / OPA system operating at 25 Hz [53]; 532-nm pumped OPG / OPA system at 25 Hz providing tunable picosecond pulses from 676 to 2497 nm [53], a similar OPG / OPA system pumped at 355 nm with tunability from 450 to 1674 nm [53]; and SHG at 370–450 nm of a mode-locked Ti:sapphire laser operating at 76 MHz [54]. The up-conversion experiments (SHG and THG) have always been extracavity. High conversion efficiencies have been obtained not only for low repetition rate amplified systems, for example 68% for SHG [2, 7, 47–50] or $>$ 50% for THG [51], but also under the conditions of tight focusing, namely with low-energy mode-locked lasers operating at high repetition rates. Thus, for example, a conversion efficiency of 52% and an average second-harmonic power of 990 mW were achieved by frequency doubling the 2.4-ps long pulses at 76 MHz [54]. In the latter case the advantages of using BIBO over BBO, in addition to the higher effective nonlinearity, include the superior angular acceptance (for higher efficiency) and low spatial walk-off (for a circular output beam profile).

The present discussion will review the application of BIBO in the femtosecond time domain. These experiments have been realized, without exception, at ICFO and MBI, and partially summarized in previous conference papers [55–58]. Several new experimental demonstrations will also be included. Before presenting the complete set of experimental results, however, we will review the relevant properties of BIBO that make this crystal a unique nonlinear material and analyze its phase-matching and spectral properties in more detail in separate sections.

Finally, we wish to highlight in this Introduction some more exotic applications of BIBO as a nonlinear optical material from the literature: These include the SHG and SFG of subnanosecond supercontinuum at 400–525 nm [59], the nonlinear cavity dumping of a Nd:$GdVO_4$ laser by nanosecond intracavity SFG at 491 nm [60], the phase-mismatched SHG as a stabilizer for a mode-locked Nd:$GdVO_4$ laser [61], and the direct THG at 355 nm in BIBO based on its $\chi^{(3)}$ nonlinearity [62, 63]. Note that very recently BIBO was used as the nonlinear crystal in an optical parametric chirped pulse amplifier [64].

2. BIBO: relevant properties

BIBO crystallizes in the noncentrosymmetric monoclinic space group $C2$ with cell parameters $a_0 = 7.116$ Å, $b_0 = 4.993$ Å, $c_0 = 6.508$ Å, monoclinic angle $\beta = 105.62°$, and $Z = 2$, see [65] and references therein. The crystal structure consists of $(B_3O_6)^{3-}$ rings that form sheets of corner-sharing $(BO_3)^{3-}$ triangles and $(BO_4)^{5-}$ tetrahedra in the ratio of 1:2 linked by six-coordinated bismuth cations. It was suggested that the extraordinarily high, for a borate crystal, second-order nonlinearity of BIBO is in fact due to the $(BiO_4)^{5-}$ anionic groups [66].

Tensor properties, such as the second-order nonlinear optical susceptibility, are generally reported in an orthogonal crystallophysical frame *XYZ* which is fixed to the crystallographic frame *abc* by certain conventions: For monoclinic crystals, $Y \equiv b$ and $Z \equiv c$ [67]. This is shown in Fig. 1, where all frames are right-handed. It was in this

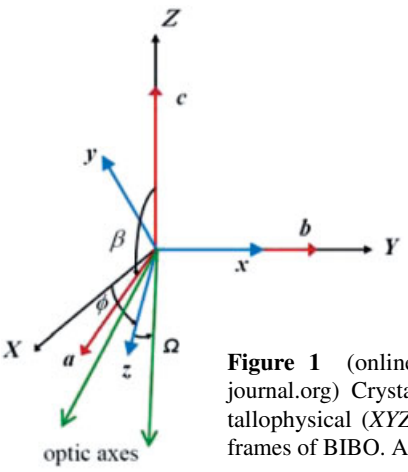

Figure 1 (online color at: www.lpr-journal.org) Crystallographic (*abc*), crystallophysical (*XYZ*) and dielectric (*xyz*) frames of BIBO. All frames right-handed.

Table 1 Effective nonlinearity d_{eff} of BIBO in the principal optical planes (Kleinman symmetry assumed).

plane, interaction type, angles	ooe, oeo≡eoo	eeo, eoe≡oee
x–*y*, ooe (I^-), eoe≡oee ($II^-\equiv III^-$)		
$\theta = 90°$	$-d_{13}\sin\varphi$	$d_{14}\sin 2\varphi$
y–*z*, eeo (I^+), oeo≡eoo ($II^+\equiv III^+$)		
$\varphi = \pm 90°$	0	$\mp d_{12}\cos^2\theta \mp d_{13}\sin^2\theta + d_{14}\sin 2\theta$
x–*z*, eeo (I^+), oeo≡eoo ($II^+\equiv III^+$)		
$\varphi = 0°$, $\Omega < \theta < 180° - \Omega$	$d_{12}\cos\theta$	$-d_{14}\sin 2\theta$
$\varphi = 180°$, $\Omega < \theta < 180° - \Omega$	$-d_{12}\cos\theta$	$-d_{14}\sin 2\theta$
x–*z*, ooe (I^-), eoe≡oee ($II^-\equiv III^-$)		
$\varphi = 0°$, $0 < \theta < \Omega$ or $180° - \Omega < \theta < 180°$	$-d_{12}\cos\theta$	$-d_{14}\sin 2\theta$
$\varphi = 180°$, $0 < \theta < \Omega$ or $180° - \Omega < \theta < 180°$	$-d_{12}\cos\theta$	$d_{14}\sin 2\theta$

crystallophysical frame *XYZ,* where the 8 independent nonlinear coefficients of BIBO were measured by the Maker fringe technique at 1079.5 nm [68]. For practical applications, however, it is highly desirable to operate with the contracted nonlinearity tensor d_{il} in the frame of the optical indicatrix or the principal optical axes *xyz*, the same frame in which the phase-matching properties are analysed. In fact, this corresponds to the tradition established in the nonlinear optics of monoclinic crystals [69]. Indeed, it was not before the nonlinear coefficients were transformed into this orthogonal dielectric *xyz* frame [70] that BIBO attracted the interest of several groups working in the field of nonlinear frequency conversion.

For point group 2 symmetry, one of the principal optical axes (the x-axis in BIBO [1]) coincides with the 2-fold symmetry axis b, but the position of the other two axes depends both on wavelength and temperature (the *xyz* frame rotates about the b-axis). The rotation of the y- and z-axes with wavelength does not exceed $\pm 1°$ in the main part of the transparency range of BIBO [1] and has only a weak effect on the calculated effective nonlinearity [36]. The change with temperature is also rather small [71, 72], about 0.24° at 1064 nm for a temperature change of 100 °C.

Thus, the transformation of the components of the nonlinearity tensor, d_{il}, was performed assuming an angle of $\phi = 47°$ between the z- and X-axes, as shown in Fig. 1, which corresponds to a wavelength of 810 nm [70]. The results summarized in Table 1 of [70] indicate that the deviation from the Kleinman conjecture [67] does not exceed $\pm 10\%$, which equals the experimental error [68]. Thus, it is justified to assume that Kleinman symmetry holds and average the corresponding d_{il} values. In this way, one arrives at [73]: $d_{14} = d_{25} = d_{36} = 1.66$ pm/V, $d_{11} = 2.53$ pm/V, $d_{12} = d_{26} = 3.2$ pm/V, and $d_{13} = d_{35} = -1.76$ pm/V, with d_{il} defined in the *xyz* dielectric frame.

So far the nonlinear coefficients of BIBO were estimated only by the Maker fringe technique [68, 74]. Several rough estimates of d_{eff} for various phase-matched processes will not be discussed here, because they essentially confirm the results in [1] and, most importantly, they confirm the relative signs of the tensor components. Theoretical models provide close values only for some of the tensor elements, but do not necessarily reproduce the relative signs obtained from the experiment [66, 75–78].

In the principal planes of the same frame, the expressions for d_{eff} of a crystal with point group symmetry 2 are given in Table 1 [73]. Here, θ and φ are the standard polar and azimuthal angles (spherical coordinates) in the *xyz* frame, while the notations "o" and "e" for the ordinary and extraordinary waves with respect to the corresponding principal plane, used in a sequence, always follow the convention $\lambda_1\lambda_2\lambda_3$ for three wave interactions with $\lambda_1 \geqslant \lambda_2 > \lambda_3$. The superscripts "+" and "−" assigned to the type-I, -II, and -III interaction denote "positive-" and "negative-" type interaction in the principal planes in analogy with uniaxial crystal notations.

Note that Table 1 lists the expressions for effective nonlinearity in all 8 octants. For monoclinic crystals, symmetry considerations indicate that only two octants with common principal plane are sufficient to uniquely describe all possible three-wave interactions. Normally, this is the first octant ($0 \leqslant \varphi \leqslant 90°$, $0 \leqslant \theta \leqslant 90°$) and one adjacent octant but no specific convention exists. We will further assume that the second octant is ($0 \leqslant \varphi \leqslant 90°$, $90° \leqslant \theta \leqslant 180°$). Thus, all cases with $\varphi = 180°$ and 270° in Table 1 will be irrelevant because they simply duplicate others. The profile of d_{eff} in the remaining 6 octants can be obtained simply by the $2/m$ symmetry, that is by reflections across the mirror plane and rotations about the two-fold axis. This is related to the fact that the conversion efficiency in nonlinear optics obeys inversion symmetry in addition to crystallographic symmetry and the sign of d_{eff} is unimportant because it is the profile of d_{eff}^2 that specifies conversion efficiency along a given phase-matching direction. In terms of d_{eff}^2, both acentric monoclinic classes exhibit a net symmetry of $2/m$, a consequence of the well-known fact that in the presence of inversion symmetry a two-fold axis becomes a normal to a mirror plane and vice versa [67]. While the sign of d_{eff} is unimportant, and in what follows we will use the absolute value, one should be careful with relative signs when more coefficients are involved, for example in the d_{eff} expression in the *y*–*z* plane (Table 1).

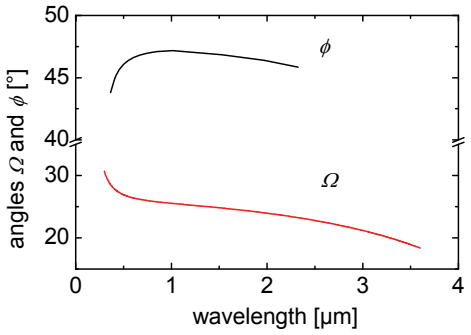

Figure 2 (online color at: www.lpr-journal.org) Wavelength dispersion of the angles ϕ (data from [1]) and Ω (calculated with the fits from [63]). See also Fig. 1.

The angle Ω in Table 1, which separates the different interaction types in the x–z plane, is defined by

$$\Omega = \arcsin\left[\frac{n_z}{n_y}\sqrt{\frac{n_y^2 - n_x^2}{n_z^2 - n_x^2}}\right] . \qquad (1)$$

This is the angle between each of the two optic axes shown in Fig. 1 and the z-axis. Propagation along the optic axes in a biaxial crystal corresponds to a phase velocity, c/n, which is independent of polarization.

Assuming $n_x < n_y < n_z$ for the principal values of the refractive index, biaxial crystals for which $\Omega < 45°$ are termed positive, in analogy with uniaxial crystals, and those for which $\Omega > 45°$ is satisfied, are referred to as negative. As can be seen from Fig. 2, BIBO is a positive biaxial crystal and the wavelength dispersion of angle Ω is more pronounced than that of angle ϕ. Nevertheless, to derive the simplified relations in Table 1, it is necessary to neglect the dispersion of Ω, that is to assume the same angle for the three interacting wavelengths. Moreover, these expressions are approximate, since the spatial walk-off due to birefringence is also neglected. However, formalism for walk-off corrections of d_{eff} expressions for biaxial crystals exists [67].

More general expressions for d_{eff}, in terms of fast and slow waves for propagation outside the principal planes can be found in [73]. In this case, the angle Ω not only enters the expressions for d_{eff}, it also defines (together with θ and φ) the polarization directions of the two orthogonal eigenpolarizations. Obviously, also in this case its dispersion is normally neglected.

As can be seen from Table 1, the effective nonlinearity for point group 2 vanishes in the plane normal to the two-fold axis if two of the three interacting waves are ordinary [73]. In this plane, the dependence of d_{eff} in BIBO on the polar angle is neither even nor odd. The maxima and minima of d_{eff} occur in this plane in directions that do not coincide with the principal optical axes, as is the case in orthorhombic biaxial crystals [69]. Hence, in this plane it is possible to phase match one and the same three-wave process with the same type of interaction (I, II or III) at two different angles θ. This leads to different d_{eff} (in planes with $\sin 2\varphi$ or $\sin 2\theta$ dependence of the effective nonlinearity, maximum d_{eff} occurs at 45°, but different values for the same phase-matching process are not possible). This is the fundamental difference between monoclinic acentric crystals and biaxial crystals with higher (orthorhombic) symmetry, where one octant is sufficient to describe both linear (dispersion and birefringence) and nonlinear (d_{eff}) properties. As a consequence, in low-symmetry crystals such as BIBO, one has an additional degree of freedom for achieving maximum d_{eff}. As can be seen from Table 1, for three given wavelengths that satisfy $\lambda_1 \geqslant \lambda_2 > \lambda_3$, the phase- matching directions in the other principal planes will correspond to different d_{eff}, but in each case the interaction type (I, II, or III) is also different.

There is no certainty that all possible polarization configurations with nonvanishing d_{eff} in Table 1 are phase matchable. The latter depends on the dispersive properties. The first refractive index measurements for BIBO at 1079.5 and 539.75 nm appeared in [68], and Sellmeier equations containing one UV pole and a quadratic IR correction term were first derived in [1] by fitting measurements extending from 365 to 2325 nm. Note that the difference between n_x and n_y in BIBO is much smaller compared with the difference with n_z, which is reflected in the fact that $\Omega \ll 90°$ (quasi-uniaxiality). The refinement in [45, 71] was based on OPO data and had validity from 474 to 3083 nm. More recently, the same authors published a further refinement of the Sellmeier equations based on direct THG (four-wave process) for propagation along the x principal optical axis, where the second-order nonlinearity d_{eff} (see Table 1) vanishes [63]. These equations, reproduced in Table 2, which are used in the present work, are valid between 326.3 and 3083 nm. It should be noted that OPO, SHG and SFG processes have also been used to derive thermo-optic dispersion formulae for BIBO [45, 63, 71, 72], important for temperature dependent phase matching in the 20–120 °C range.

Table 2 Sellmeier coefficients of BIBO: $n^2 = A + B/(\lambda^2 - C) - D\lambda^2$ valid in the 0.32–3.09 μm range (from [63]).

	A	B [μm^2]	C [μm^2]	D [μm^{-2}]
n_x	3.0759	0.03169	0.03323	0.01402
n_y	3.1698	0.03666	0.03599	0.01819
n_z	3.6546	0.05116	0.03713	0.02299

Other refractive index measurements of BIBO appeared in [2] and other measurements of the thermo-optic coefficients can be found in [79]. In [80] the refractive indices were measured at four temperatures for four wavelengths and four sets of Sellmeier equations were fitted for different temperatures. However, the obtained thermo-optic coefficients are very different from those in [63], see Table 3. A possible explanation for this discrepancy is that in [80] the effect of the thermal expansion on the index values had not

Table 3 Some physical properties of the monoclinic BIBO crystal.

Properties		[Ref.]
melting point (congruent)	726 °C [a]	[81]
crystal structure (space group – point group)	monoclinic noncentrosymmetric ($C2 \equiv C_2^3 - 2$)	[65]
lattice constants	$a_0 = 7.116(2)$ Å, $b_0 = 4.993(2)$ Å, $c_0 = 6.508(2)$ Å, $\beta = 105.62(3)^\circ$, $Z = 2$	[65][b]
cell volume and density	222.69 Å^3 and 5.033 g/cm^3	[65][c]
UV cut-off edge / bandgap	270 nm / 4.59 eV	[46,47,50,82]
transparency range (1 cm^{-1} level)	286–2600 nm	[82]
absorption / scattering losses at 1064 nm	< 0.0009 cm^{-1}	[83]
refractive index at 632.8 nm / 1064 nm	$n_x = 1.77668/1.75752$, $n_y = 1.80641/1.78400$, $n_z = 1.94582/1.91711$	[63]
optical ellipsoid orientation (632.8 nm)	$\boldsymbol{x} \parallel \boldsymbol{b}$, $\angle(\boldsymbol{a},\boldsymbol{z}) = 31.1^\circ$, $\angle(\boldsymbol{c},\boldsymbol{y}) = 46.72^\circ$	[1]
angle between the two optic axes at 1064 nm	$2\Omega = 52.6^\circ$ (optically positive)	[63]
strongest phonon mode / Debye temperature	1485 cm^{-1} / 2140 K	[84]
specific heat	500 J/kg K @ 57 °C	[50][d]
thermo-optic coefficients at 632.8 nm	$dn_x/dT = 8.6 \times 10^{-6}$ K^{-1}, $dn_y/dT = -3.7 \times 10^{-6}$ K^{-1}, $dn_z/dT = -6.3 \times 10^{-6}$ K^{-1}	[63]
at 1064 nm	$dn_x/dT = 3.5 \times 10^{-6}$ K^{-1}, $dn_y/dT = -5.6 \times 10^{-6}$ K^{-1}, $dn_z/dT = -6.8 \times 10^{-6}$ K^{-1}	
thermal expansion coefficients α and orientation of the thermal expansion ellipsoid, $\boldsymbol{X}_1\boldsymbol{X}_2\boldsymbol{X}_3$	$\alpha_{11} = -28.9 \times 10^{-6}$ K^{-1}, $\alpha_{22} = 53.7 \times 10^{-6}$ K^{-1}, $\alpha_{33} = 9.3 \times 10^{-6}$ K^{-1}, $\boldsymbol{X}_2 \parallel \boldsymbol{b}$, $\angle(\boldsymbol{X}_3, \boldsymbol{c}) = 8.4^\circ$	[85][e]
two-photon absorption coefficient at 355 nm	$\beta_x = 0.71$ cm/GW, $\beta_{yz} = 1.37$ cm/GW	[51][f]
	$\beta_x = 7.1$ cm/GW, $\beta_{yz} = 16$ cm/GW	[36][g]
Kerr type nonlinearity n_2 at 1064 nm	$n_{2x} = 9.5 \times 10^{-16}$ cm^2/W, $n_{2y} = 11.4 \times 10^{-16}$ cm^2/W, $n_{2z} = 19.6 \times 10^{-16}$ cm^2/W	[86][h]
damage threshold	> 300 GW/cm^2 (45 fs @ 800 nm)	[87]
	> 48 GW/cm^2 (56 ps @ 1064 nm)	[86]
	> 3.5 GW/cm^2 (40 ps @ 532 nm), > 1 GW/cm^2 (29 ps @ 355 nm)	[51]
	0.6 GW/cm^2 (5 ns @ 1064 nm), 0.4 GW/cm^2 (< 5 ns @ 532 nm)	[4][i]
	55 MW/cm^2 ($E \parallel x$), 59 MW/cm^2 ($E \perp x$)* (7.8 ns @ 355 nm)	[36]
	~ 160 kW/cm^2 ($E \parallel x$, CW @ 473 nm)	[6]
Moh's hardness	5–6	[49,88,89]

[a] 708 °C in [90,91];
[b] slightly different parameters measured in [47,48] while the assignment in the preliminary work [92] seems different;
[c] 4.897 g/cm^3 estimated in [47–49] by the buoyancy method;
[d] measured in the 40–210 °C range;
[e] measurement from –100 to 300 °C by dilatometry – the fits contain also quadratic terms, similar measurements in the 25–299.5 °C range gave the values $\alpha_{11} = -26.43 \times 10^{-6}$ K^{-1}, $\alpha_{22} = 50.4 \times 10^{-6}$ K^{-1}, $\alpha_{33} = 8.53 \times 10^{-6}$ K^{-1} and $\angle(\boldsymbol{X}_3, \boldsymbol{c}) = 8.9^\circ$ [93,94];
[f] measurements with 29-ps pulses at 355 nm with a crystal cut of $\varphi = 90^\circ$, $\theta = 146^\circ$;
[g] measurements with 7.8 ns pulses at 355 nm with a crystal cut of $\varphi = 90^\circ$, $\theta = 123.7^\circ$;
[h] measured with 56-ps pulses using the Z-scan technique, values increased here by a factor of ~ 1.23 to account for the actual beam waist;
[i] 6–7 GW/cm^2 given in [74] for 6 ns pulses at 1064 nm;
* see [g] for the cut.

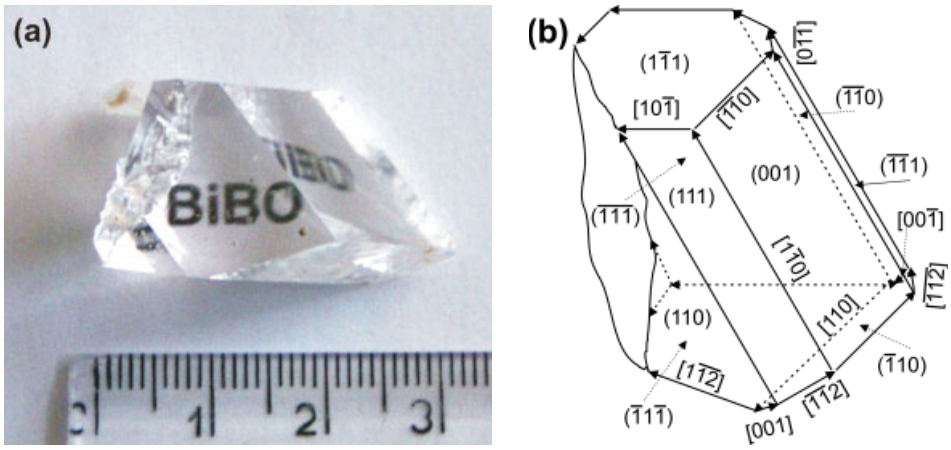

Figure 3 (online color at: www.lpr-journal.org) As-grown from the melt single crystal of BiB_3O_6, BiBO or BIBO, (a) and its morphology (b). The seed used can be seen in the upper left corner of (a). The crystal is confined with perfect crystallographic faces except its part surrounding the seed.

been accounted for, whereas this effect was taken into account in [79]. In any case, the results of [63] should be most reliable because the refinement is based on phase-matched nonlinear processes and not simply index data.

The UV cut-off wavelength in BIBO is at 270 nm [46, 47, 50, 82]. Theoretical calculations of the electronic structure indicate an indirect bandgap in this region [95, 96]. At the 1 cm^{-1} absorption level, the transmission of BIBO extends from 286 to 2600 nm [82]. The absorption feature near 2400 nm is seen only in thick samples [1, 46, 47, 50, 82]. The same also holds for the OH^- peak near 2800 nm [46, 50, 82]. The transparency of BIBO extends up to 6250 nm [47], but the practical upper limit is determined by two-phonon absorption.

Several studies were devoted to the vibrational spectra of BIBO: Raman scattering [84, 97–100], IR spectroscopy [99], and polarized reflectivity measurements [101]. Stimulated Raman scattering has also been observed [98]. The strongest phonon mode determined in all these studies has almost the same frequency (see Table 3). The vibrational frequencies of BIBO were calculated from first principles in [102]. Twice the energy of the strongest phonon mode corresponds to a wavelength of $\sim$3370 nm, which matches well with the onset of strong absorption in the IR spectrum of BIBO [47].

BIBO is in fact one of the crystals offering highest characterized optical quality and homogeneity [83, 103]. The linear losses measured at 1064 nm, see Table 3, are comparable to the losses in high-quality KTP, and roughly two times lower than those typically observed in BBO and LBO. BIBO is a chemically stable and nonhygroscopic crystal [47–49]. Besides the damage levels listed in Table 3, photorefractive effects have been observed in SHG with tightly focused CW beams [17, 27, 104]. Information on other characteristics such as electro-optic, piezoelectric and elastic properties, can be found in [79] and [105].

Finally, at present BIBO can be grown by top-seeded growth from stoichiometric melts. Maximum sizes of $\sim 20 \times 20 \times 30\,mm^3$ [81], $\sim 44 \times 24 \times 10\,mm^3$ [47], and $\sim 30 \times 30 \times 40\,mm^3$ [7, 106], see Fig. 3, and weight of 120 g [93, 106] have been reported in the literature.

3. Phase matching in BIBO

There exists no universal nonlinear crystal that can simultaneously meet the requirements for all nonlinear frequency-conversion processes. When discussing the unique properties of BIBO, one considers comparison to other crystals for applications in similar spectral range. Typical borate crystals used in nonlinear optics, such as LBO or BBO, although widely exploited for the visible and near-IR, are the crystals of choice for the UV down to 160 nm. In contrast, BIBO does not possess such deep-UV transparency. Hence, within its transparency range, it should also be compared with crystals such as KTP and its isomorphs that exhibit nonlinearities higher than the borates. Indeed, for certain three-wave interactions, such as frequency doubling of 1-μm lasers [1], BIBO has been demonstrated to possess higher effective nonlinearity than KTP. Combined with the fact that BIBO exhibits larger bandgap, and consequently higher damage threshold and lower two-photon absorption, this implies really unique capabilities in the visible and near-IR. However, if and to what extent such properties come into play depends on the phase-matching characteristics, which are determined by the dispersion and birefringence properties of BIBO. Although most of the following experimental results will be related to down-conversion, the phase-matching properties can be presented in a more compact and illustrative form for SHG (the reverse process in the case of degeneracy).

The Hobden diagrams for collinear type-I and type-II SHG in BIBO are shown in Figs. 4 and 5. The points where possible loci of directions change their topological pattern correspond to the fundamental wavelengths for which the transitions between the different Hobden classes take place [107], see Table 4.

Note that the transition wavelengths correspond to the so-called noncritical phase matching along one of the three principal optical axes, either for type-I or type-II SHG. However, in several cases the fundamental or second harmonic lie outside the clear transmission range where the Sellmeier fits (Table 2) are also only extrapolated. Furthermore, d_{eff} for this crystal symmetry vanishes for propaga-

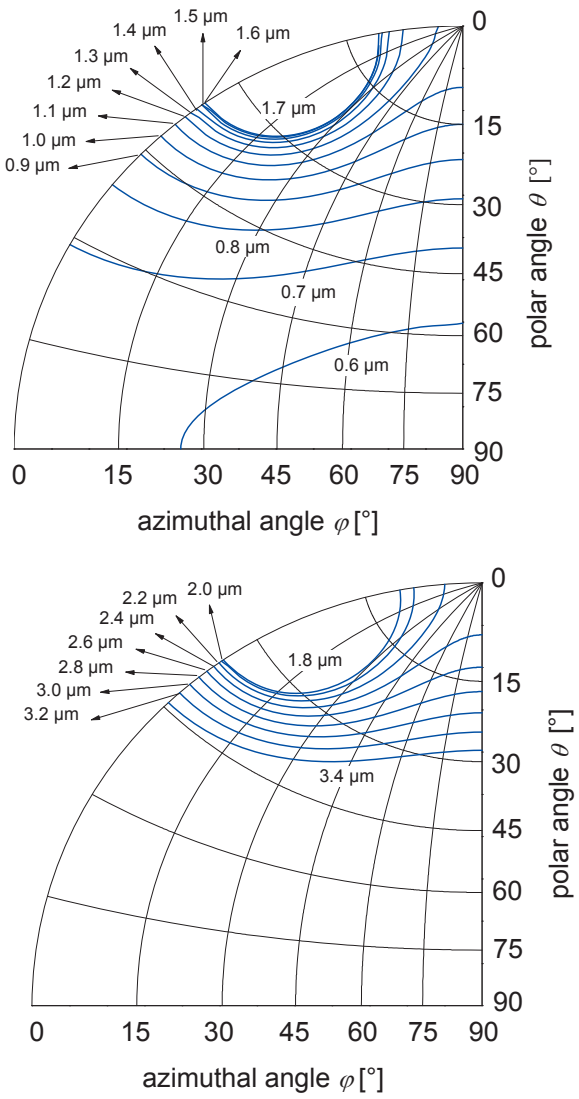

Figure 4 (online color at: www.lpr-journal.org) Hobden diagrams for type-I SHG in BIBO.

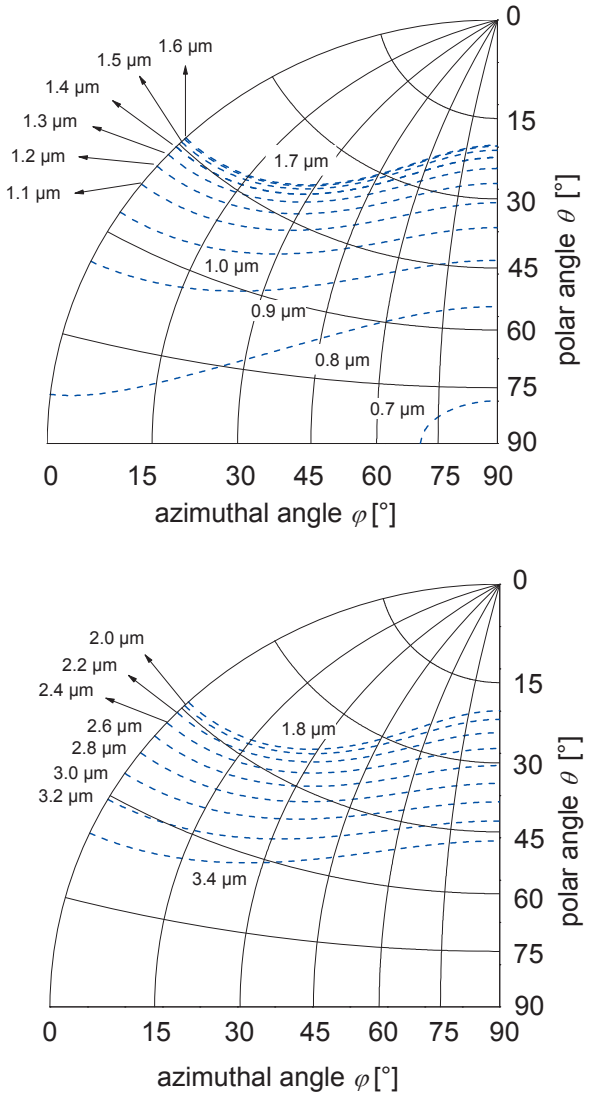

Figure 5 (online color at: www.lpr-journal.org) Hobden diagrams for type-II SHG in BIBO.

Table 4 Hobden classes for collinear SHG and transition (fundamental) wavelengths with the corresponding noncritical directions (dielectric axes) and types of phase matching (I or II).

class	transition wavelength [nm]	axis	type
14→13	545.7	y	I
13→8	614.3	x	I
8→7	690.0	y	II
7→6	793.7	x	II
6→2	1181.5	z	I
2→6	2272.8	z	I
6→7	3800	x	II
7→8	4330	y	II
8→13	5107	x	I

tion along the x-axis and also for propagation along the y-axis and type-II phase matching, as can be seen from Table 1. Thus, the only practical cases of noncritical phase matching remain for type-I interaction along the z-axis at 1181.5 and 2272.8 nm, which are characterized by maximum effective nonlinearity $|d_{\text{eff}}| = d_{12}$.

The behavior of d_{eff} in two octants, calculated using the general analytical formula from [73], is shown for two representative fundamental wavelengths and type-I interaction in Fig. 6. The profiles for a fundamental wavelength of 800 nm in Fig. 6a indicate maximum $|d_{\text{eff}}|$ in the y–z principal plane for the ($0 \leqslant \varphi \leqslant 90°$, $90° \leqslant \theta \leqslant 180°$) octant. In contrast, at a fundamental wavelength of 1600 nm, the absolute maximum is also in the same octant, but not in a principal plane. Very high d_{eff} is available, however, also in the x–z plane. For any wavelength, the values in the x–z plane are equal for the two octants (see Table I).

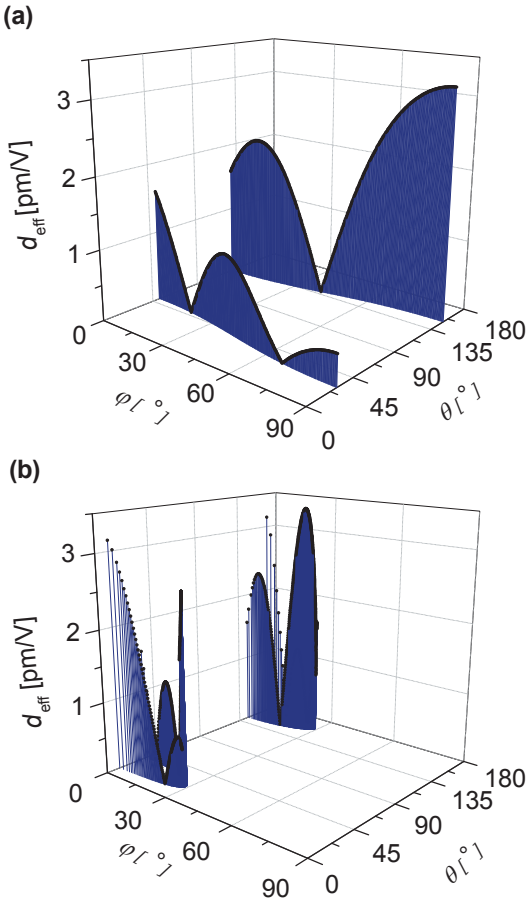

Figure 6 (online color at: www.lpr-journal.org) Effective nonlinearity of BIBO for collinear type-I SHG and fundamental wavelengths of 800 nm (a) and 1600 nm (b) along the phase-matching loci in two octants.

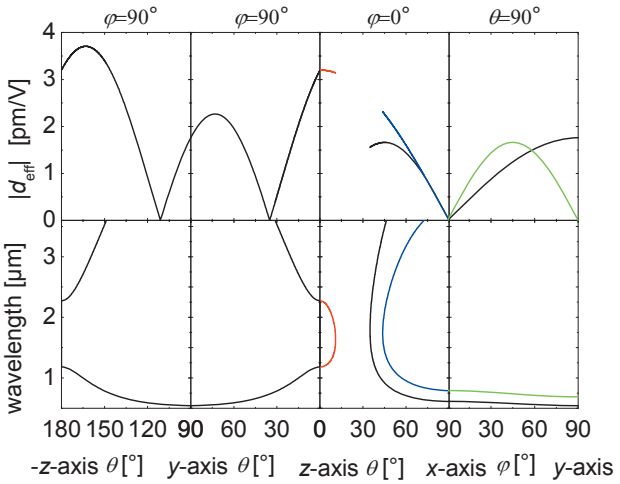

Figure 7 (online color at: www.lpr-journal.org) Fundamental wavelength and effective nonlinearity versus phase-matching angle for type-I (black and red curves) and type-II (blue and green curves) SHG in the principal planes of BIBO for the cases when $d_{\text{eff}} \neq 0$.

The phase-matching configurations for collinear SHG in the three principal optical planes, together with the absolute value of the effective nonlinearity, are depicted in Fig. 7. In the x–y plane, negative type-I phase matching is possible from 545.7 nm ($|d_{\text{eff}}| = d_{13}$, but strongly absorbed second harmonic) to 614.3 nm, where d_{eff} vanishes. Negative type-II phase matching in this plane is possible between 690 and 793.7 nm. The effective nonlinearity has a maximum value of $|d_{\text{eff}}| = d_{14}$ near 738 nm but vanishes at both limits.

In the x–z plane, both positive and negative type-I phase matching are possible. Negative type-I extends from 1181.5 to 2272.8 nm and, as already mentioned, is characterized by maximum$|d_{\text{eff}}| = d_{12}$ in the two limits. Since the polar angle increases only up to about $\theta = 11°$ throughout the whole wavelength range, the effective nonlinearity remains generally high (of the order of d_{12}). The positive type-I phase matching covers wavelengths from 614.3 nm, where d_{eff} vanishes, up to above the IR transparency limit of BIBO. The effective nonlinearity is maximized at 920 and 3479 nm, with $|d_{\text{eff}}| = d_{14}$. Thus, across the entire wavelength range, the effective nonlinearity is roughly two times lower than for the case of negative type-I phase matching in the same plane. Only positive type-II phase matching is possible in the x–z plane. It starts from 793.7 nm, where d_{eff} again vanishes, and extends beyond the IR transmission limit. The effective nonlinearity is maximized at 1739 nm, reaching a value $|d_{\text{eff}}| = 0.72 d_{12}$.

In accordance with our selection of the two octants, although the phase matching is symmetric across the y-axis, the effective nonlinearity in the y–z plane, which is nonzero only for type-I phase matching (Table 2), has to be considered in the $0 \leqslant \theta \leqslant 180°$ interval. One branch of the solutions extends from 545.7 nm ($\theta = 90°$, $|d_{\text{eff}}| = |d_{13}|$) to 1181.5 nm ($\theta = 0°$, 180°, where $|d_{\text{eff}}| = d_{12}$). Although the effective nonlinearity has the same limiting values in both octants, in between it is different. For $0 \leqslant \theta \leqslant 90°$, maximum effective nonlinearity ($|d_{\text{eff}}| = 2.26$ pm/V) is obtained at 584 nm for $\theta = 73.2°$, while it vanishes at 811 nm. For $90 \leqslant \theta \leqslant 180°$, maximum effective nonlinearity ($|d_{\text{eff}}| = 3.70$ pm/V) is obtained at 895 nm for $\theta = 163.3°$, while it vanishes at 583 nm.

There is a second branch of solutions in this plane, which starts from 2272.8 nm at $\theta = 0°$, 180° ($|d_{\text{eff}}| = d_{12}$) and extends beyond the IR transmission cut-off. For this branch of the solution, the effective nonlinearity is always higher for the $\varphi = 90°$, $90 \leqslant \theta \leqslant 180°$ octant where $|d_{\text{eff}}| \geqslant d_{12}$.

The above analysis of the SHG phase matching in the principal planes of BIBO refers to collinear propagation of the waves. Noncollinear SHG in the principal planes of BIBO has also been considered in [108].

Let us now consider the more practical comparison with BBO in terms of effective nonlinearity, internal angular ac-

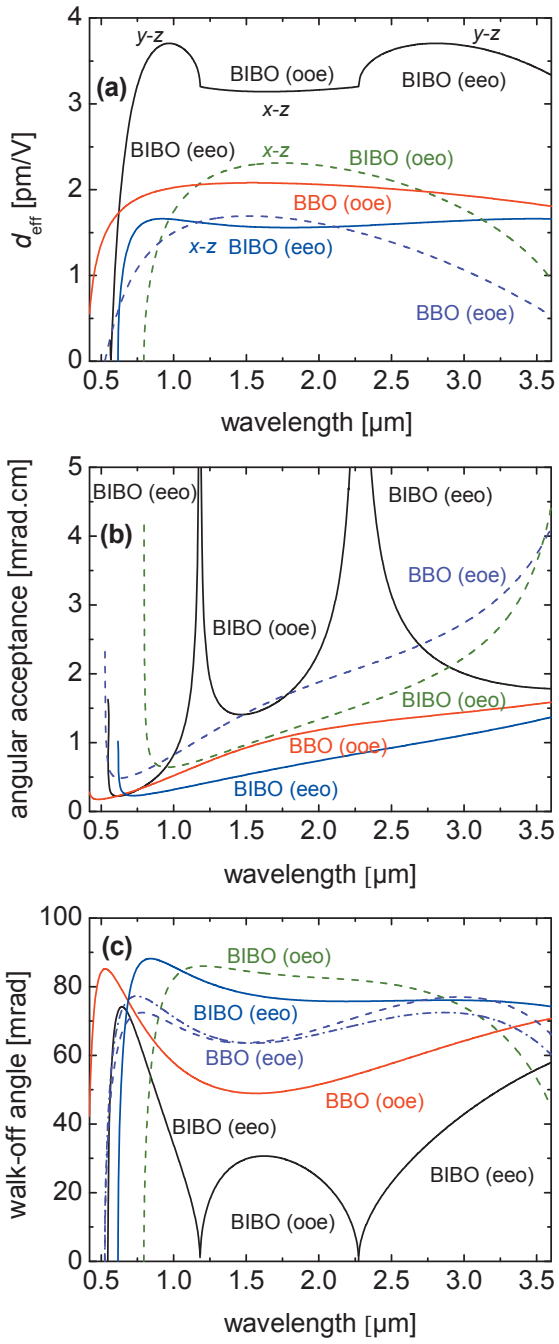

Figure 8 (online color at: www.lpr-journal.org) Effective nonlinearity (a), internal angular acceptance (b) and spatial walk-off (c) versus fundamental wavelength for SHG in the principal planes of BIBO in comparison to BBO. In (a) and (b), dashed curves refer to type-II interaction, in (c) dashed curves refer to the walk-off angle for the fundamental wave and the dash-dotted curve – for the second harmonic.

ceptance bandwidth, and spatial walk-off in the principal planes of BIBO as a function of fundamental wavelength. As can be seen from Fig. 8b, the angular acceptance could be a limiting factor under conditions of tight focusing of low-intensity laser beams, but in general it is maximized near the principal optical axes, where the effective nonlinearity is also maximum. As is well known, in the case of critical phase matching away from the principal optical axes, the walk-off angle caused by birefringence (Fig. 8c) is inversely proportional to the angular acceptance. However, in the vicinity of these axes, this parameter tends to zero. Apart from the case of eeo phase matching in the x–z plane, which has no advantages, both angular acceptance and spatial walk-off are more favorable in BIBO than in BBO for type-I phase matching, and with higher effective nonlinearity (Fig. 8a). This increases the tolerance of phase matching to tight focusing (or poor spatial beam quality) of the fundamental in the SHG process, resulting in improved SHG output power, conversion efficiency, and spatial beam profile. In type-II phase matching, BIBO is superior in some respects and inferior with regard to other characteristics, see Fig. 8, and this depends on the fundamental wavelength (if it is below or above 0.9 μm).

Also, interestingly, for wavelengths near 1.2 μm, the walk-off angle approaches zero. This makes BIBO very attractive for SHG of CW or low-intensity pulsed Nd-lasers under type-I noncritical phase-matching condition [36].

On the basis of the SHG phase-matching analysis in this section, it can be concluded that propagation in the vicinity of the z-axis and type-I interaction are definitely most important for BIBO, because one can simultaneously achieve high effective nonlinearity, large angular acceptance and minimum spatial walk-off, all of which are highly desirable for any nonlinear frequency-conversion process. However, the situation with the spectral parameters, which are closely related to interaction of ultrashort (femtosecond) pulses, is different, and we devote a special section to this analysis.

4. Spectral acceptance and parametric gain bandwidth

In this section, due to the relevance to the experimental results, we will consider the SHG process in more detail, as a degenerate SFG process, and down-conversion in BIBO, focusing on the potential of the material for frequency conversion of ultrashort (femtosecond) laser pulses. In all cases, the simplest analytical treatment of the temporal limitations is based on the spectral acceptance, and with the convention $\lambda_1 \geqslant \lambda_2 > \lambda_3$ one can simultaneously describe several processes. However, OPG and OPA are travelling-wave devices without an optical cavity, which require much higher pump intensities, and hence consideration of the parametric gain bandwidth is desirable. This parameter is proportional to the spectral acceptance but, in addition, takes into account a gain factor. On the other hand, the OPO is a device that operates under low to moderate pump intensities and, as such, requires an optical cavity. It can be pumped directly by CW, microsecond, or nanosecond pulses, or synchronously by ultrafast picosecond and femtosecond pulses. Femtosecond synchronously pumped OPOs (SPOPOs) are generally

pumped by mode-locked lasers at repetition rates of the order of 100 MHz, while femtosecond OPGs and OPAs are pumped by regenerative and/or multipass laser amplifiers operating at typical repetition rates of 1 kHz or higher.

BIBO is a useful nonlinear crystal throughout its entire transparency range and in any time scale, from femtosecond pulses to CW laser radiation. In general, its performance could be compared to a number of other nonlinear crystals, such as the birefringent BBO, LBO, KTP, $KNbO_3$, or periodically poled materials such as PPKTP or PPSLT. However, concerning the ultrashort (femtosecond) time scale, its dispersion properties indicate that only a comparison with BBO is appropriate (LBO could also compete with regard to low dispersion, but its nonlinearity is already much lower than that of BIBO). For this reason, in the following analysis, we will compare the properties of BIBO primarily with BBO.

The spectral acceptance for SHG, derived from the phase-matching condition by considering the conversion efficiency [69], is given by

$$\Delta\nu_1 = \Delta\nu_2 = 0.886/(L|\Delta|)\,, \tag{2}$$

where L denotes the crystal length and $\Delta = 1/v_1 + 1/v_2 - 2/v_3$, with v_1, v_2, and v_3 denoting the group velocities of the fundamental (possibly two different polarizations and hence group velocities) and the second harmonic, respectively. The above equation refers to the fundamental. At the second harmonic, the bandwidth is twice as large, $\Delta\nu_3 = 2\Delta\nu_1$ (in terms of wavelengths this relation is reversed, $2\Delta\lambda_3 = \Delta\lambda_1$). Only in the vicinity of the wavelength at which the group velocity mismatch (GVM) parameter, Δ, vanishes, is it necessary to consider next-order terms in the expansion of wave mismatch [69]. This leads to

$$\Delta\nu_1 = \sqrt{\frac{1.772}{\pi L\,|k_1'' + k_2'' - 4k_3''|}}\,, \tag{3}$$

where the group velocity dispersion, GVD (k''), at the second-harmonic predominates (see Fig. 9). Equations (2) and (3) are strictly valid only in the fixed-field approximation [69], equivalent to low conversion efficiency. Moreover, they are derived assuming monochromatic waves and neglecting the different group velocities. When operating with femtosecond pulses, type-I phase matching is generally preferable, because there is no additional reduction in efficiency caused by the GVM between the two fundamental waves as in type-II interaction.

Fig. 9 shows the GVM and GVD parameters calculated for type-I BIBO and BBO (data for BBO taken from [69, 88]). It is clear that both crystals have very broad and similar spectral acceptance near 1600 nm, where the GVD starts to play a role in the broadening of second-harmonic pulses. Hence, in this wavelength region, which is interesting for mode-locked Er-fiber lasers generating sub-100 fs pulses at ∼ 100 MHz repetition rates, BIBO is the best candidate for efficient SHG if short pulse durations

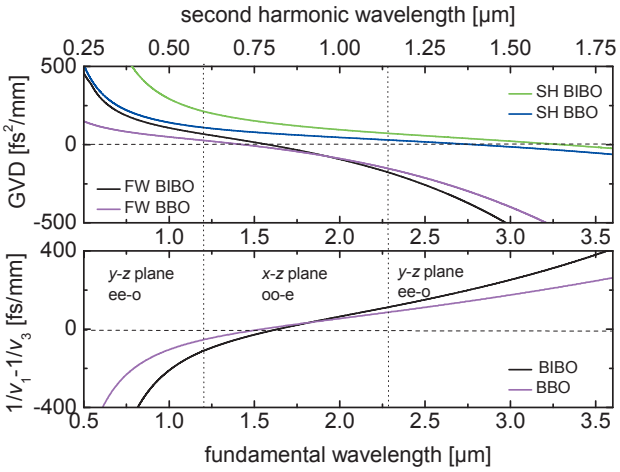

Figure 9 (online color at: www.lpr-journal.org) Group velocity mismatch (GVM), bottom, and group-velocity dispersion (GVD, k"), top, for type-I SHG in BIBO and BBO versus fundamental wavelength. FW: fundamental, SH: second harmonic.

are to be maintained. This is so because the effective nonlinearity of BIBO is superior to BBO, and this plays a major role in obtaining higher efficiency when using tight focusing with such low-power, high-repetition-rate femtosecond sources. The conversion efficiency with BIBO will also be higher at other wavelengths, for example near 800 nm, but this advantage could be matched by using a thicker BBO crystal, offering lower GVM at such wavelengths (see Fig. 9). Nevertheless, BIBO can still be advantageous at other wavelengths because for a given crystal length its larger angular acceptance and smaller spatial walk-off can result in superior output beam quality.

Figs. 10 and 11 show the important case of SPOPO pumped near 800 nm, where mode-locked Ti:sapphire lasers at ∼ 100 MHz repetition rate can be used as the pump source. Only negative type-I phase matching in the x–z plane of BIBO is shown in Fig. 10, because the positive type exhibits much lower effective nonlinearity, whereas Fig. 11 covers both oeo and eoo type-II phase matching in the x–z plane.

The phase-matching curves for type-I phase matching in BIBO, shown in Fig. 10a, cover the full transparency range. After reaching a maximum polar angle (slightly above 11°), the curves change their character of dependence on pump wavelength, and exhibit retracing behavior (two pairs of signal and idler phase matched simultaneously), which is an indication of broad spectral acceptance (extremely weak dependence on the critical angle). The behavior of BBO is, in principle, similar (shown, for brevity, only for $\lambda_3 = 800$ nm). The effective nonlinearity is almost constant with wavelength in both crystals but much higher in BIBO.

The spectral acceptance in nondegenerate three-wave interactions can be calculated analytically only under additional assumptions. Generally, for OPOs, OPGs and OPAs,

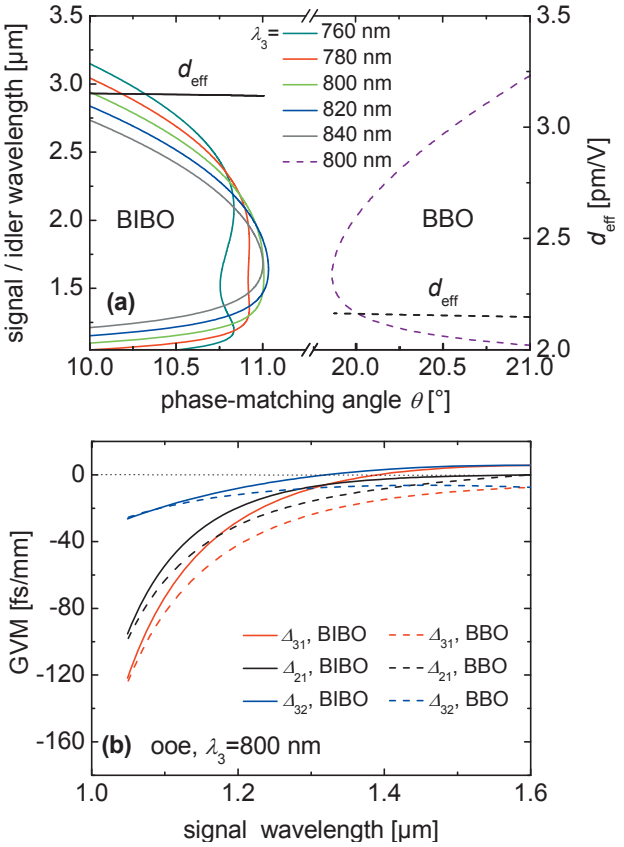

Figure 10 (online color at: www.lpr-journal.org) Down-conversion in BIBO and BBO for negative type-I (ooe) phase matching at five pump wavelengths near 800 nm (a). The effective nonlinearity in both crystals is shown only for $\lambda_3 = 800$ nm. GVM in BIBO and BBO for the same phase matching and pump wavelength equal to 800 nm (b).

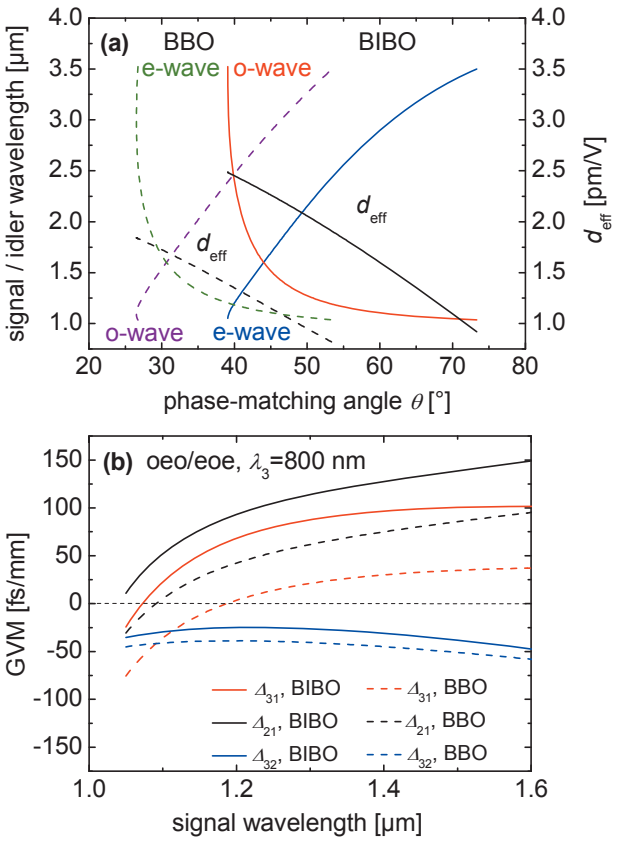

Figure 11 (online color at: www.lpr-journal.org) Down-conversion for type-II phase matching, positive in BIBO and negative in BBO, at a pump wavelength of $\lambda_3 = 800$ nm (a). The effective nonlinearity in both crystals is also shown. GVM in BIBO and BBO for the left branches of the phase-matching curves, oeo type in BIBO and eoe in BBO (b).

it is assumed that the pump wave at λ_3 has a much narrower bandwidth than the signal and idler waves. In that case, the spectral acceptance is given by

$$\Delta\nu_1 = \Delta\nu_2 = 0.886/(L|\Delta_{12}|)\,. \qquad (4)$$

For completeness, Fig. 10b shows all the GVM parameters of BIBO and BBO for $\lambda_3 = 800$ nm. Moving with the signal wavelength towards degeneracy, one can see that BIBO always exhibits a smaller GVM parameter Δ_{21}, equivalent to a larger spectral acceptance. There is also a fairy broad spectral range, only in the case of BIBO, near $\lambda_2 = 1340$ nm, where the signal and idler pulses travel with group velocities very close to that of the pump. This interesting property of BIBO, which will be discussed in more detail later in this section, is related to the fact that pump wavelengths near 800 nm are close to the point where, in the SHG process, the second harmonic has the same group velocity as the fundamental (see lower part of Fig. 9). At degeneracy, the temporal walk-off of the signal/idler pulses from the pump, which determines the efficiency of the parametric down-conversion, is almost the same in BIBO and BBO (Fig. 10b).

In both crystals, type-II phase matching has two branches (Fig. 11a). In both branches, the effective nonlinearity varies with wavelength, but it is always higher for the left branch (oeo in BIBO and eoe in BBO), which alone can cover the entire transparency range with smaller variation of the critical angle. In all cases, the effective nonlinearity is substantially higher for BIBO than for BBO.

The GVM parameters, for only the left branches, are shown in Fig. 11b. The temporal walk-off between the pump and signal waves is smaller in BIBO, but the spectral acceptance, as defined by Eq. (4), is also smaller. Note that finite spectral acceptance is maintained in both crystals up to degeneracy, in contrast to type-I phase matching, Fig. 10, where higher-order terms have to be considered in this limit.

The situation for pumping near 400 nm (second harmonic of femtosecond Ti:sapphire lasers) is shown in Figs. 12 and 13. Type-I eeo phase matching in BIBO (Fig. 12) is realized in the $90° \leqslant \theta \leqslant 180°$ part of the

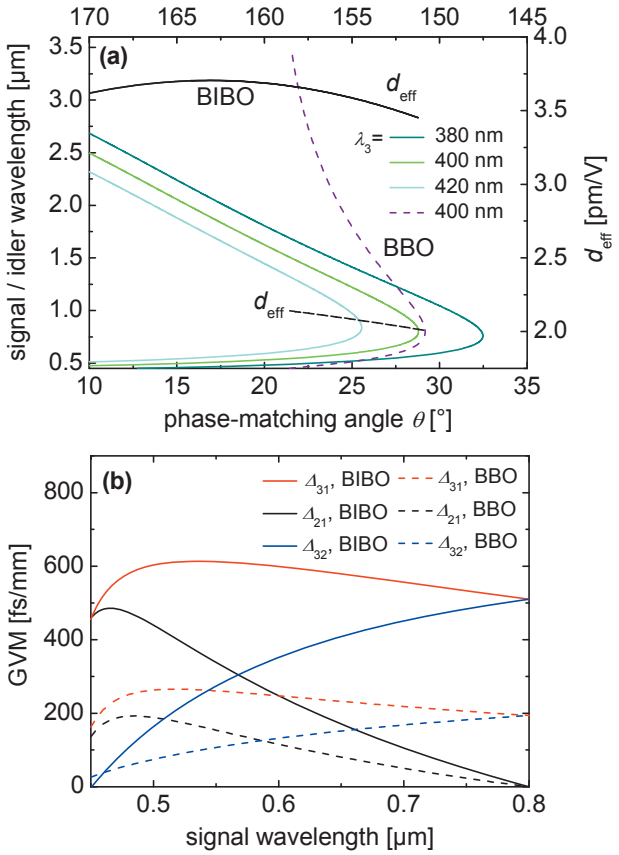

Figure 12 (online color at: www.lpr-journal.org) Down-conversion in BIBO (positive type-I, eeo) and BBO (negative type-I, ooe) at three pump wavelengths near 400 nm (a). The lower abscissa refers to BBO and the upper one to BIBO. The effective nonlinearity in both crystals is shown only for $\lambda_3 = 400$ nm. GVM in BIBO and BBO for the same phase matching and pump wavelength equal to 400 nm (b).

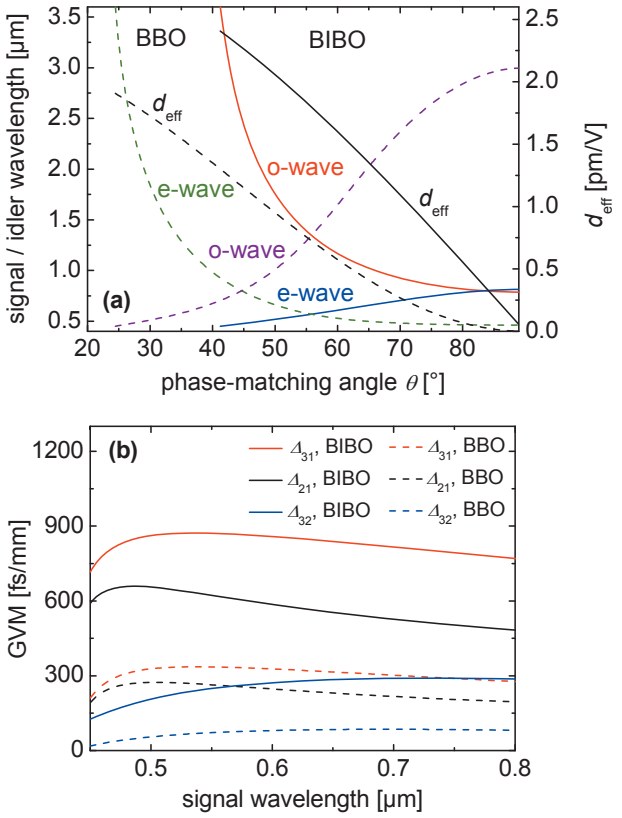

Figure 13 (online color at: www.lpr-journal.org) Down-conversion for type-II phase matching, positive in BIBO and negative in BBO, at a pump wavelength of $\lambda_3 = 400$ nm (a). The effective nonlinearity in both crystals is also shown. GVM in BIBO and BBO for the left branches of the phase-matching curves, oeo type in BIBO and eoe in BBO (b).

y–z plane in order to exploit higher effective nonlinearity (see Table 1). Type-II phase matching (Fig. 13) utilizes the same configuration as for pumping near 800 nm.

Also for pumping near 400 nm, type-I phase matching in BIBO exhibits much higher effective nonlinearity than BBO, see Fig. 12a, The GVM parameters are, however, in general roughly two times larger (Fig. 12b).

The situation with type-II phase matching is different when pumping near 400 nm, because $d_{\rm eff}$ of BIBO is in fact comparable or even lower, depending on the visible signal wavelength, than that of BBO, see Fig. 13a. For both crystals, the GVM parameters change to a lesser extent with wavelength. Their values are much higher for BIBO, and it can be concluded that there are no advantages in using this polarization configuration.

The extreme spectral bandwidths that can be accommodated by BIBO type-I when pumped near 800 nm, seen from Fig. 10, where higher-order dispersion terms are deliberately not considered, deserve special attention. The bandwidth can be further increased at high parametric gain (high pump intensity), and that is why we will consider this case in more detail. Note that similar properties are also expected for BBO with type-I interaction. On the other hand, pumping near 400 nm does not exhibit a similar property. In general, pumping near 400 nm is feasible only in low-power schemes such as the SPOPO, since in OPG or OPA devices strong two-photon absorption will occur.

In the discussion to follow, we will use the most common notations $\lambda_P = \lambda_3$ for the pump, $\lambda_S = \lambda_2$ for the signal, and $\lambda_I = \lambda_1$ for the idler wavelength, which apply to OPO/SPOPO and OPG/OPA. In the plane-wave approximation, in the absence of pump depletion, the steady-state gain for the signal wave at λ_S (intensity) is given by [109, 110]:

$$G = 1 + \frac{\Gamma^2}{g^2}\sinh^2(gL)\,, \tag{5}$$

with $g = \sqrt{\Gamma^2 - (\Delta k/2)^2}$, where $\Delta k = k_S + k_I - k_P$ is the wave mismatch and the exponential gain coefficient, Γ, is defined by $\Gamma^2 = \frac{8\pi^2 d_{\rm eff}^2 I_{\rm P}}{n_{\rm P} n_{\rm S} n_{\rm I} \lambda_{\rm I} \lambda_{\rm S} \varepsilon_0 c}$. In the limit of large

gain ($\Gamma L \gg 1$) the above equation simplifies to:

$$G = \tfrac{1}{4}\exp(2gL)\,. \tag{6}$$

In order to obtain analytical expressions for parametric gain bandwidth, the wave mismatch is usually expanded in a series as a function of frequency, assuming in a first approximation that the pump is monochromatic,

$$\begin{aligned}\Delta k = \Delta k_0 &+ \left(\frac{\partial k_\mathrm{S}}{\partial \omega_\mathrm{S}} - \frac{\partial k_\mathrm{I}}{\partial \omega_\mathrm{I}}\right)\Delta\omega \\ &+ \frac{1}{2!}\left(\frac{\partial^2 k_\mathrm{S}}{\partial \omega_\mathrm{S}^2} + \frac{\partial^2 k_\mathrm{I}}{\partial \omega_\mathrm{I}^2}\right)(\Delta\omega)^2 \\ &+ \frac{1}{3!}\left(\frac{\partial^3 k_\mathrm{S}}{\partial \omega_\mathrm{S}^3} - \frac{\partial^3 k_\mathrm{I}}{\partial \omega_\mathrm{I}^3}\right)(\Delta\omega)^3 \\ &+ \frac{1}{4!}\left(\frac{\partial^4 k_\mathrm{S}}{\partial \omega_\mathrm{S}^4} + \frac{\partial^4 k_\mathrm{I}}{\partial \omega_\mathrm{I}^4}\right)(\Delta\omega)^4 \ldots\,, \end{aligned} \tag{7}$$

where $\Delta\omega = \Delta\omega_S$ denotes the frequency change of the signal wave and, by energy conservation, the idler frequency change will be $\Delta\omega_I = -\Delta\omega$. The phase-matching condition means that $\Delta k_0 = 0$. The individual terms in Eq. (7) are used to evaluate the points, in terms of frequency, where the gain function G from Eq. (6) drops to 50% of its maximum value, which corresponds to the wave vector mismatch $\Delta k_{1/2} \approx \pm 2(\ln 2)^{1/2}(\Gamma/L)^{1/2}$. The results, when using the first derivative (GVM approximation) and the second derivative (GVD approximation), are well known [109, 110] and read, in terms of FWHM, for $\Delta\nu = \Delta\omega/2\pi$

$$\Delta\nu = \frac{2\,(\ln 2)^{1/2}}{\pi}\left(\frac{\Gamma}{L}\right)^{1/2}\left|\frac{1}{v_\mathrm{S}} - \frac{1}{v_\mathrm{I}}\right|^{-1} \tag{8}$$

$$\Delta\nu = \frac{2\,(\ln 2)^{1/4}}{\pi}\left(\frac{\Gamma}{L}\right)^{1/4}\left|\frac{\partial^2 k_\mathrm{S}}{\partial \omega_\mathrm{S}^2} + \frac{\partial^2 k_\mathrm{I}}{\partial \omega_\mathrm{I}^2}\right|^{-1/2}. \tag{9}$$

Considering the next terms one obtains from Eqs. (6) and (7):

$$\Delta\nu = \frac{(144\ln 2)^{1/6}}{\pi}\left(\frac{\Gamma}{L}\right)^{1/6}\left|\frac{\partial^3 k_\mathrm{S}}{\partial \omega_\mathrm{S}^3} - \frac{\partial^3 k_\mathrm{I}}{\partial \omega_\mathrm{I}^3}\right|^{-1/3} \tag{10}$$

$$\Delta\nu = \frac{2\,(9\ln 2)^{1/8}}{\pi}\left(\frac{\Gamma}{L}\right)^{1/8}\left|\frac{\partial^4 k_\mathrm{S}}{\partial \omega_\mathrm{S}^4} + \frac{\partial^4 k_\mathrm{I}}{\partial \omega_\mathrm{I}^4}\right|^{-1/4}. \tag{11}$$

It is clear that for collinear type-I interaction, the third-order term (10) also vanishes near degeneracy, and this makes it necessary to consider the fourth-order term [111]. From our consideration, this term is given by Eq. (11). From the four approximations, one should use, depending on the signal wavelength, the term which predicts the smallest gain bandwidth. In the $\lambda_S = 1100$–1300 nm range, for ooe interaction in the x–z plane of BIBO pumped at 800 nm, this is the solution based on the GVM term. Approaching degeneracy, however, the GVD term also vanishes as a consequence of the fact that for polarization parallel to the y-axis (o-wave for the present interaction scheme), it is zero at 1578 nm.

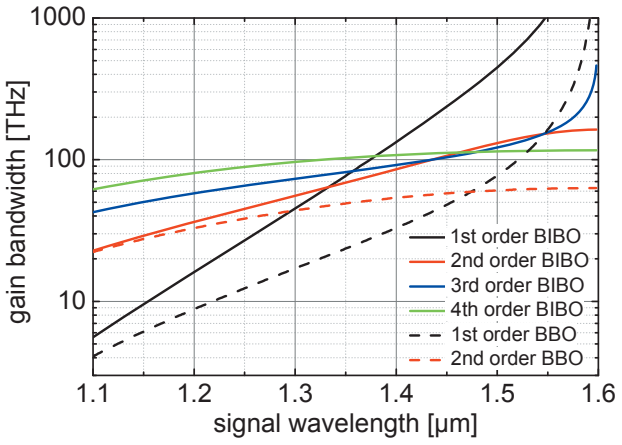

Figure 14 (online color at: www.lpr-journal.org) Gain bandwidth (FWHM) of BIBO and BBO, analytically calculated for collinear type ooe interaction at $\lambda_P = 800$ nm, a crystal length of 5 mm and pump intensity of 50 GW/cm^2 using only the first-, second-, third- and fourth-order Taylor series expansion terms of the wavevector mismatch Δk, respectively.

It is interesting that the fourth-order approximation should be used for BIBO starting already from 1500 nm, see Fig. 14. This approximation predicts a gain bandwidth (FWHM intensity) of about 3800 cm^{-1} (116 THz) near degeneracy. In contrast, the spectral bandwidth of BBO for the same crystal and pump parameters is determined near degeneracy by the second-order derivatives and amounts to 63 THz, which is roughly two times smaller, see Fig. 14.

Direct calculations of the parametric gain G using Eq. (5) at the exact phase-matching angle are presented in Fig. 15. It can be seen that the gain bandwidth at first increases but then decreases with the pump wavelength. There exists an optimum pump wavelength near $\lambda_P = 780$ nm, where the gain bandwidth is maximized. This can be seen in Fig. 16 where the gray area depicts the range limited by the 50% drop in gain from its maximum value. The left part of the figure corresponds to the retracing behavior of the phase-matching curves, see Fig. 10a, where "satellites" appear in Fig. 15, corresponding to the second pair of signal and idler waves phase matched at the same angle θ.

Thus, for pump wavelengths near 800 nm, collinear ooe interaction in BIBO possesses the exclusive property of simultaneous vanishing of the first three terms that determine the gain bandwidth. Many other nonlinear crystals with sufficient birefringence in fact possess the same property, provided the three wavelengths lie within the transparency range. This is related to the existence of retracing behavior of the phase-matching curves [111, 112], which can be traced back to the material dispersive properties. In any case, it happens at a certain pump wavelength that does not necessarily coincide with the wavelengths of the available

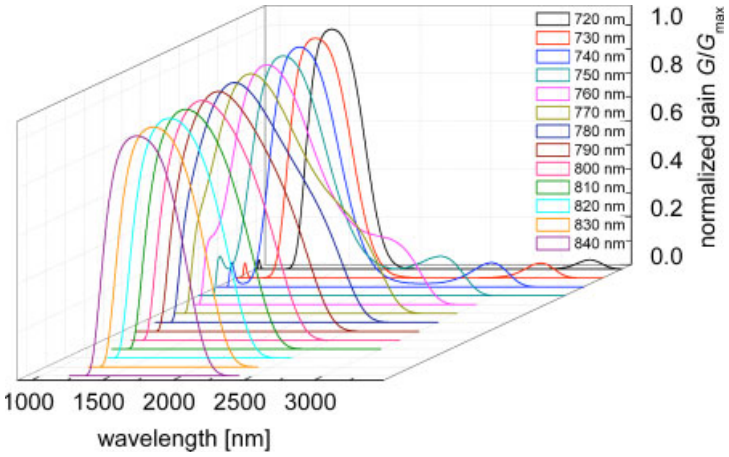

Figure 15 (online color at: www.lpr-journal.org) Normalized parametric gain in BIBO (negative type-I ooe interaction in the x–z plane) for different pump wavelengths (indicated) at exact phase-matching angles, for a crystal length of 5 mm and pump intensity of 50 GW/cm^2.

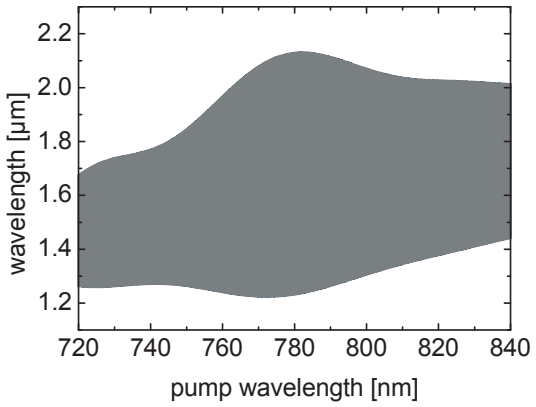

Figure 16 Gain bandwidth (FWHM) as estimated from Fig. 15. The absolute gain G decreases from 1.41×10^8 at $\lambda_P = 720$ nm to 2.91×10^7 at $\lambda_P = 780$ nm and to 5.56×10^6 at $\lambda_P = 840$ nm.

femtosecond sources that can be used for pumping OPAs or OPGs. As can be seen from Table 5, this same property is also characteristic of periodically poled materials (type-0 interaction), where quasi-phase-matching is realized by suitable choice of the poling period. Note that retracing behavior (and the gain bandwidth) can also be controlled by varying the crystal temperature.

Moreover, there is another favorable property related to the dispersion characteristics of BIBO that directly affects the interaction length with the pump, and consequently the achievable conversion efficiency. The retracing behavior occurs at angles for which the phase-matching curves reverse their curvature as a function of the pump wavelength, see Fig. 10a and [113]. The critical angle for which

Table 5 Parameters of several crystals that can be used in ultrabroadband OPA/OPG schemes pumped below 1 µm: λ_P is the "magic" pump wavelength for which the signal/idler GVD vanishes near degeneracy, λ_F is the fundamental wavelength for broadband SHG, $\Delta\lambda/\Delta\nu$ correspond to the wavelength/frequency range for maximum gain bandwidth calculated directly from Eq. (5) at the 1/2 level (crystal length 5 mm, pump intensity 50 GW/cm^2), θ/φ and Λ are the phase-matching angle and the period for degenerate operation at the given λ_P in birefringent and quasi-phase-matching, respectively, and the GVM parameter $1/v_P - 1/v_{S,I}$ is calculated for degenerate operation at λ_P.*

crystal	λ_P [µm]	λ_F [µm]	$\Delta\lambda$ [µm]	$\Delta\nu$[THz]	θ/φ [°] or Λ [µm]	$1/v_P - 1/v_{S,I}$ [fs/mm]
KDP (ooe)	0.493	1.035	0.746–1.444	402–208	42.11	14.0
LBO (ooe/eeo) x–y/x–z	0.599	1.304	1.043–1.408	288–213	1.35	17.9
CLBO (ooe)	0.627	1.3375	0.987–1.713	304–175	28.57	10.8
BBO (ooe)	0.716	1.541	1.203–1.767	249–170	21.33	15.2
BIBO (ooe) x–z	0.789	1.637	1.233–2.189	243–137	10.97	11.9
BIBO (eeo) x–z	0.810	1.794	1.237–2.345	243–128	35.11	31.5
PPSLT (eee)	0.825	2.378	1.486–1.856	202–162	21.56	189
PPKTP (eee)	0.895	2.503	1.471–2.286	204–131	32.54	141
$LiNbO_3$ (ooe)	0.949	2.028	1.624–2.284	185–131	46.27	37.2
PPLN (eee)	0.957	2.699	1.647–2.272	182–132	27.93	161
$KNbO_3$ (ooe) x–y	0.988	2.138	1.665–2.442	180–123	47.71	46.3
$KNbO_3$ (ooe) y–z	1.004	2.066	1.681–2.497	178–120	15.63	17.8
$LiIO_3$ (ooe)	1.040	2.235	1.784–2.488	168–107	20.13	16.0

* The Sellmeier and nonlinear coefficient data used for the table, with the exception of BIBO, is from [88]: For KH_2PO_4 (KDP), LBO, $CsLiB_6O_{10}$ (CLBO), BBO, PPKTP, $LiIO_3$, and $KNbO_3$, the so-called "best dispersion relations" were used; for $LiNbO_3$ and PPLN, the data chosen was for congruent material, and in the case PPSLT the data used was for stoichiometric lithium tantalate. The validity of the Sellmeier expansion does not always cover the full $\Delta\lambda$ ranges.

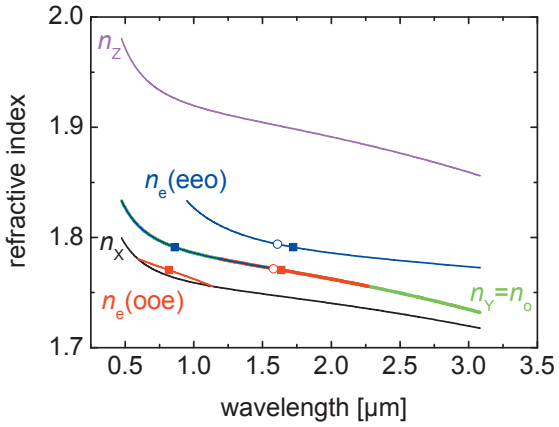

Figure 17 (online color at: www.lpr-journal.org) Refractive index of BIBO for type-I SHG in the x–z plane. Red curves correspond to ooe and blue curves to eeo phase matching. The squares indicate the points where the first derivatives of the refractive index for the fundamental and second harmonic are equal (broadband SHG phase matching corresponding to λ_F in Table 5) and the circles indicate the points of vanishing second derivative (corresponding to twice the "magic" pump wavelength or $2\lambda_P$ in Table 5).

this happens in ooe type-I BIBO is in the vicinity of the phase-matching curve turning point for the inverse process of SHG, see Fig. 7. Such a turning point (at λ_F) in the dependence of the fundamental wavelength on the phase-matching angle in SHG means nothing but broadband phase matching, which is equivalent to vanishing GVM between the fundamental and the second harmonic. Indeed, it can be easily shown that this GVM vanishes at the point where $(\partial\theta/\partial\lambda)_{\lambda_F} = 0$ for the SHG phase-matching curve [114], see Fig. 10a. The existence of a turning point in the SHG phase-matching curve, see Fig. 7, is attributed to anomalous dispersion [114]. It, in fact, determines the existence of the retracing phenomenon in the OPA/OPG curves, which can be characterized by three or more turning points [112]. This can be easily seen from Fig. 10a but the origin of the phenomenon can be traced back to the refractive-index dependences, shown for BIBO in Fig. 17.

Similar analytical relations cannot be derived for the GVM with the pump in the case of three waves, because both the signal and idler are broadband. However, it is clear that an OPA/OPG operating in the vicinity of the phase-matching angle, where the SHG phase-matching curve has a turning point, will also be characterized by very low GVM between the pump and the other two waves. For example, for the considered type of interaction in BIBO, the turning point of the SHG phase-matching curve occurs at a fundamental wavelength of $\lambda_F = 1637$ nm. Both this wavelength and the "magic" pump wavelength for ultrabroadband parametric amplification were calculated and are presented in Table 5 for several crystals applicable in the near-IR.

In the other type-I interaction scheme in BIBO, the deviation of λ_F from $2\lambda_P$ is larger and, consequently, the GVM with the pump is also larger. In fact, Table 5 shows that the only crystal for which the GVM with the pump at the "magic" pump wavelength is smaller than for ooe BIBO is CLBO. Similar arguments also hold for quasi-phase-matched materials, where the turning point is defined with respect to the phase-matching period. Since, in this case, the polarization of the three waves is the same, one can expect the deviation of λ_F from $2\lambda_P$ to be larger, see Fig. 17, leading to larger GVM with the pump. For instance, the GVM with the pump in the degenerate PPKTP-OPA pumped at the "magic" wavelength amounts to 141 fs/mm, in PPSLT it is as high as 189 fs/mm, while it is only 11.9 fs/mm in BIBO (ooe).

Thus, it should be emphasized that there is nothing unique in the dispersive properties of BIBO with respect to the achievable gain bandwidths. The only advantage of BIBO over other existing crystals is that it exhibits these important properties in collinear interaction, at a pump wavelength coinciding with the most widely used and technologically developed ultrafast Ti:sapphire laser amplifiers, which are routinely deployed as pumps for ultrafast OPAs/OPGs. It can be seen from Table 5 that the achievable bandwidths, in the four borates considered and in KDP, exceed 100 THz. However, as a result of the specific behavior of its three refractive indices (presumably related to anomalous infrared dispersion), the two characteristic wavelengths, λ_F and $2\lambda_P$, in BIBO are very close, especially for type ooe phase matching, leading to low GVM among all the three waves in a degenerate OPA/OPG pumped near 800 nm.

5. SHG of low-power, high-repetition-rate femtosecond pulses

In this section, we present experimental results on extracavity SHG of low-power high-repetition-rate laser sources operating in the 800-nm spectral range (mode-locked Ti:sapphire laser) and near 1600 nm (mode-locked Er-fiber laser), as well as intracavity SHG of signal pulses in a PPLN-based femtosecond SPOPO. Extracavity SHG of femtosecond pulses from a mode-locked Yb:$KGd(WO_4)_2$ laser operating at 1040 nm has been studied in [115].

5.1. SHG of a mode-locked femtosecond Ti:sapphire laser operating at 76 MHz

These SHG experiments were performed with a commercial mode-locked Ti:sapphire laser (Coherent, Mira) delivering ~ 130 fs pulses at 76 MHz repetition rate with an average power of up to 1.9 W, tunable over 750–950 nm. From the calculations of effective nonlinearity described in earlier sections, see Figs. 7 and 8, eeo type-I interaction in the y–z plane was chosen as the most effective phase-matching scheme. The BIBO crystals used were grown by the top-seeded techniques [116]. They were cut at $\theta = 156°$. Three

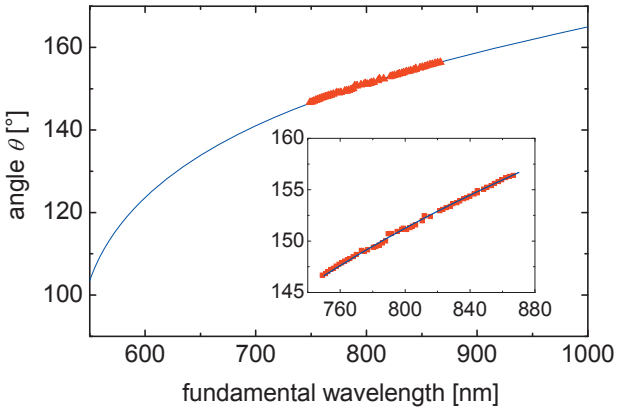

Figure 18 (online color at: www.lpr-journal.org) Angular phase-matching range for eeo type-I SHG in the y–z plane of BIBO as a function of fundamental wavelength**.** The inset shows the angular tuning range over an expanded scale, calculation (lines) and experiment (symbols).

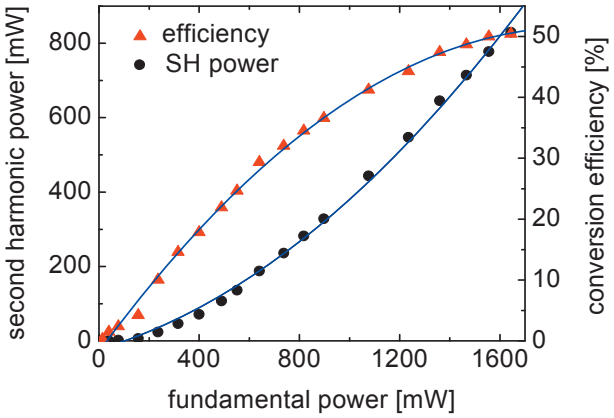

Figure 19 (online color at: www.lpr-journal.org) Second-harmonic (SH) average power at 406 nm and conversion efficiency as functions of input fundamental power for a 1.4-mm thick crystal of BIBO.

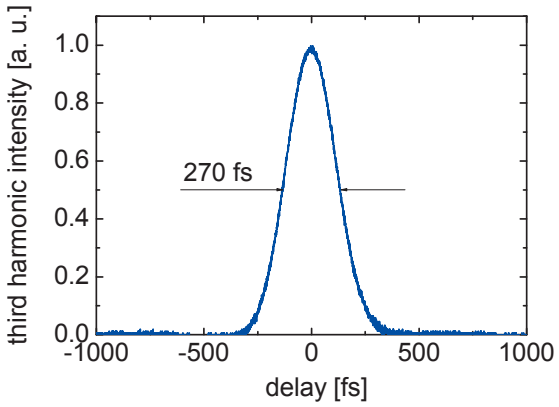

Figure 20 (online color at: www.lpr-journal.org) Cross-correlation function recorded for the second-harmonic pulses at 406 nm generated with a 0.4-mm thick BIBO crystal.

uncoated crystals of lengths 0.4, 0.7, and 1.4 mm were used in these experiments.

Fig. 18 shows typical SHG tuning data obtained with the 1.4-mm crystal and the corresponding calculated tuning curve. We were able to achieve wavelength tuning from 375 to 435 nm, limited by the crystal aperture at larger angles.

To obtain maximum SHG efficiency in a circular output beam, an important parameter, in addition to the effective nonlinearity, is spatial walk-off, as depicted in Fig. 8. For eeo type-I phase matching in y–z plane, the calculated walk-off angle varies between 40 and 65 mrad over the tuning range of our fundamental laser (750–950 nm). This has been experimentally confirmed in [117] using a similar Ti:sapphire laser. It implies that for a focused beam waist radius of $w_0 \sim 50\,\mu$m, say, the generated SHG pulses produced at the focus will be separated from the fundamental after $\sim$ 2–4 mm of propagation. However, this length will also depend on the exact position of the focus within the crystal, so that maximization of efficiency for a given crystal length will require the optimization of focusing strength and position within the crystal. Therefore, to obtain the optimum conditions for SHG output power and efficiency, we varied the focusing conditions in each BIBO sample, using different lenses with focal lengths of 60 to 160 mm, with the beam-waist location within each sample carefully optimized. The highest SHG output power and efficiency was obtained with the thickest crystal, 1.4 mm in length, with the results shown in Fig. 19. The maximum average second-harmonic power generated in this crystal was 830 mW for 1.65 W of input fundamental power, corresponding to a conversion efficiency of 50.3%. At the maximum input power, there is evidence of saturation in SHG efficiency, with the value remaining close to $\sim$ 50%.

Another important parameter in the attainment of high conversion efficiency, under conditions of tight focusing, is the phase-matching acceptance angle for SHG. For eeo type-I phase matching in the y–z plane, the angular acceptance varies from 0.28 to 0.58 mrad cm across the fundamental tuning range of 750 to 950 nm, see Fig. 8. The calculated angular acceptance bandwidths were experimentally verified through measurements of second-harmonic power in the 1.4-mm crystal by using the Ti:sapphire laser in the CW regime [118].

Temporal characterization of the blue pulses was performed using cross-correlation measurements in a thin crystal of BBO type-I. Fig. 20 shows the recorded signal at the third harmonic using an AlGaN detector, for a BIBO crystal of 0.4 mm length, at a second-harmonic wavelength of 406 nm. From GVM consideration in the BBO crystal ($\sim$ 315 fs/mm between 812 and 406 nm pulses), we chose a 100- µm thick crystal to ensure a reliable estimate of the second-harmonic pulse duration. For the 0.4-mm BIBO crystal, by deconvolving the curve from Fig. 20, we ob-

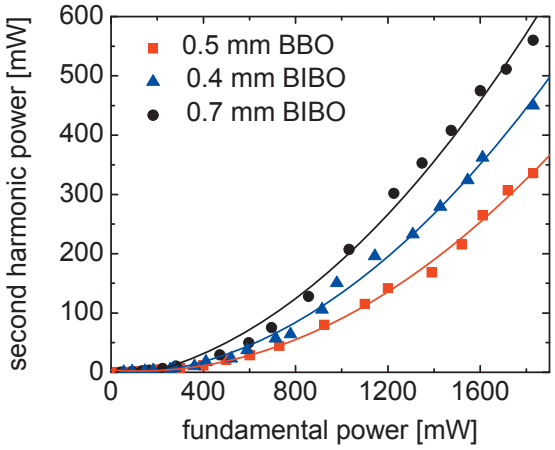

Figure 21 (online color at: www.lpr-journal.org) Comparison of the generated second-harmonic power at 406 nm in BIBO and BBO as a function of input fundamental power.

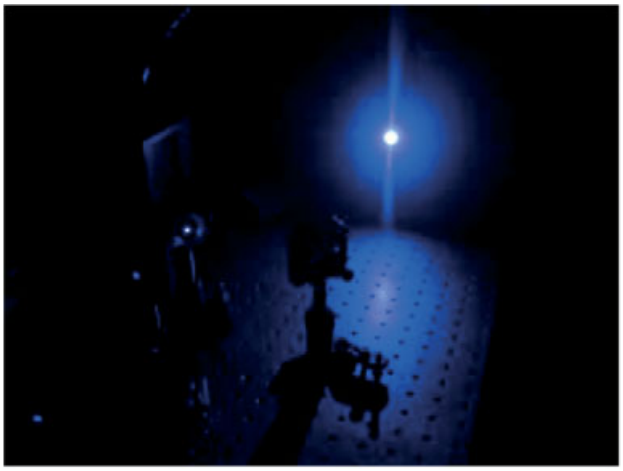

Figure 22 (online color at: www.lpr-journal.org) Photograph of the generated second-harmonic beam in the blue (406 nm).

tained ~ 220 fs (assuming sech^2 pulse shape), indicating broadening from the fundamental pulse.

We also compared the performance of BIBO with BBO. Using the two BIBO crystals of lengths 0.4 and 0.7 mm, we compared the second-harmonic output power with a 0.5-mm BBO crystal, under the same experimental conditions. Optimized focusing using an $f = 80$ mm focal length lens ensured maximum output power. The results are shown in Fig. 21. The data correspond to a second-harmonic wavelength of 406 nm. The maximum average blue power generated with the 0.4-mm BIBO was 450 mW, compared to 336 mW obtained with BBO, implying $\sim 34\%$ power enhancement despite a shorter crystal length.

A photograph of the generated blue beam is shown in Fig. 22. The beam exhibits excellent spatial quality with minimum ellipticity due to low spatial walk-off in the BIBO crystal. This result provided new impetus for the development of ultrafast femtosecond SPOPOs in wavelength regions that have been previously difficult to access. With the availability of high optical powers and exceptional conversion efficiencies in single-pass SHG experiments in BIBO, described above, the development of ultrafast femtosecond SPOPOs pumped in the blue to provide tunability across the visible spectrum has become a practical reality. Such a SPOPO operating in the visible and UV will be described in Sect. 6.

5.2. SHG of a mode-locked femtosecond Er-fiber laser operating at 56 MHz

While the previous subsection dealt with comparison of BIBO and BBO in terms of average power at the second harmonic and conversion efficiency, a more conclusive comparison coupled to the pulse duration can be realized in the wavelength range near 1600 nm, where the GVM for SHG tends to vanish for both crystals, see Fig. 9. It is the reverse process, but in fact the same case of extremely broad spectral acceptance as discussed in Fig. 10.

Frequency doubling in this spectral range is rather interesting, because mode-locked Er-fiber lasers operate in this region, providing high-repetition-rate trains of femtosecond pulses. Owing to the broad tunability of existing femtosecond OPG / OPA systems pumped near 800 nm by amplified Ti:sapphire laser systems, there is a trend to simplify such pump sources by fixing their wavelength using an all solid-state oscillator design based on frequency-doubled femtosecond Er-lasers as seed. However, the output power of such lasers, even preamplified in Er-fiber amplifiers, is rather low in the 100-fs regime, and this makes SHG inefficient. Thus, 10% conversion efficiency was achieved for 86-fs pulses at 771 nm using a 1-cm thick BBO for SHG [119]. At a repetition rate of 31.8 MHz, this corresponds to 270 pJ. A higher conversion efficiency of 25% was reported with PPLN, but at longer pulse durations, 190 fs at 777 nm, with a corresponding single pulse energy of 90 pJ at 88 MHz [120]. Here, we present a rigorous comparison between BIBO and BBO for such SHG.

According to Fig. 10, very large spectral acceptance can be expected both for ooe type-I BIBO in the x–z plane and for type-I interaction in BBO. However, the spatial walk-off is larger and the angular acceptance is lower in BBO, Fig. 8, while BIBO exhibits roughly 1.5 times higher effective nonlinearity. Given the spectral bandwidth of a transform-limited 60-fs long sech^2-shaped pulse at the fundamental, optimum crystal lengths to preserve this pulse duration at the second harmonic are between 5 and 6 mm. We compared two crystals of BIBO, 5- and 6-mm thick, cut at $\theta = 11.4°$ in the x–z plane with a BBO crystal of 6 mm, cut at $\theta = 19.9°$ [121]. This choice is related to the fact that the spectral acceptance in BBO, determined by the second-order terms, see Eq. (3), is somewhat larger at the exact operating wavelength. All samples used were uncoated.

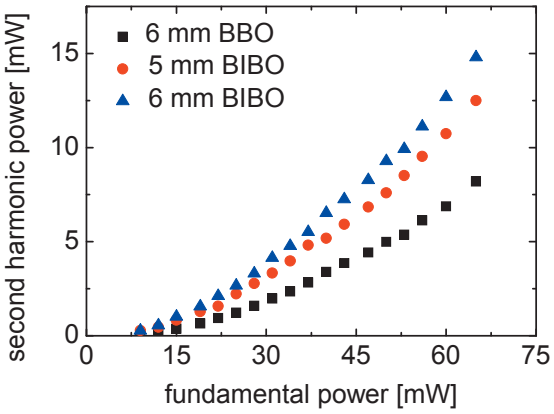

Figure 23 (online color at: www.lpr-journal.org) Average power at the second harmonic versus fundamental power.

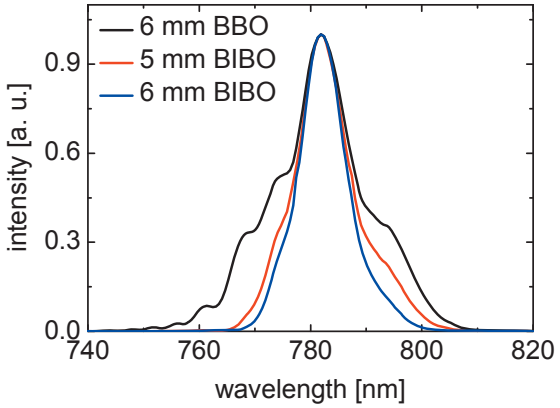

Figure 24 (online color at: www.lpr-journal.org) Spectra at the second harmonic at 782 nm.

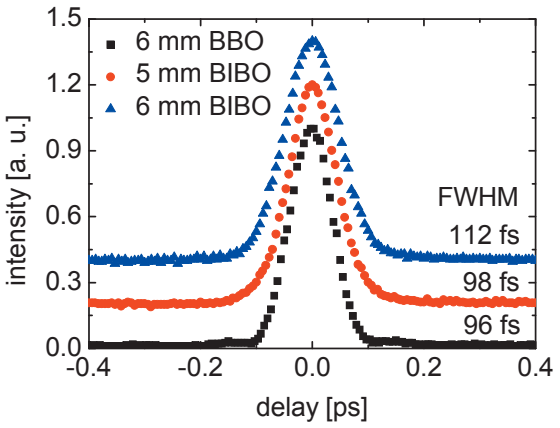

Figure 25 (online color at: www.lpr-journal.org) Autocorrelation traces of the second-harmonic pulses. FWHM values refer to the autocorrelation traces.

The SHG experiments were carried out with a diode-pumped mode-locked (by polarization rotation) Er-fiber laser-amplifier system. The passively mode-locked pulse train at a repetition rate of 56 MHz was amplified up to an average power of 65 mW, corresponding to the output energy of 1.16 nJ at 1564 nm. The intensity autocorrelation measurement with a 2-mm thick BBO crystal indicates a fundamental pulse duration of 59 fs, assuming a sech^2 pulse shape. The linearly polarized, diffraction-limited ($M^2 \sim 1.0$) beam, after coupling out of the amplifier, was collimated (or nearly collimated) with two lenses. Several different lenses were tested for focusing into the SHG crystals, with $f = 75$ mm chosen to achieve maximum SHG powers, where the beam spot radius at the focus was measured to be $w_o(1/\mathrm{e}^2) \sim 25$ µm. The fundamental power was adjusted by a combination of a thin achromatic wave-plate and a calcite polarizer, and observed with a thermopile detector. A KDP crystal was placed after the SHG crystals to block the fundamental beam, and the transmitted SHG signal was detected with a calibrated Si-photodiode. (The KDP filter was removed during the spectral and autocorrelation measurements).

Fig. 23 shows the average power dependence between fundamental and second-harmonic beams measured with the 5- and 6-mm thick uncoated BIBO samples. At the maximum incident fundamental power of 65 mW, second-harmonic powers of 12.5 and 14.8 mW were obtained with the 5- and 6-mm thick BIBO samples, corresponding to an internal conversion efficiency as high as 23% and 27%, respectively. These results were compared with the 6-mm thick type-I BBO sample under identical conditions (Fig. 23). The measured output power was approximately 2.0 to 1.5 and 2.3 to 1.8 times higher with the 5- and 6-mm thick BIBO samples, respectively, from the low to high input power levels. Note that the large conversion efficiency for BIBO has caused a small saturation of the SHG output power at the highest input power level, indicating the depletion of fundamental power. The maximum pulse energy achieved at the second harmonic was 265 pJ.

The results of the spectral and temporal characterization of the second-harmonic pulses are shown in Figs. 24 and 25, respectively. The irregular spectrum obtained with the BBO sample replicates the structure of the fundamental spectrum. A pulse duration of 62 fs is obtained in this case, assuming a sech^2-shaped pulse, which, for a spectral FWHM bandwidth of 15 nm, results in $\tau\Delta\nu = 0.44$. In contrast, smooth spectra have been observed from the two BIBO samples, but with narrower bandwidths. The almost identical pulse duration of 64 fs obtained with the 5-mm thick BIBO sample implies a higher-quality second-harmonic pulse ($\tau\Delta\nu = 0.35$), while the longer pulse duration of 73 fs for the 6-mm thick sample indicates that the slightly smaller acceptance bandwidth elongates the pulse. Nevertheless, with this BIBO sample the second-harmonic pulses were also bandwidth limited, with $\tau\Delta\nu = 0.34$.

The present results that confirm the higher second-harmonic conversion efficiency at the same pulse duration are a clear indication of the superiority of BIBO over BBO

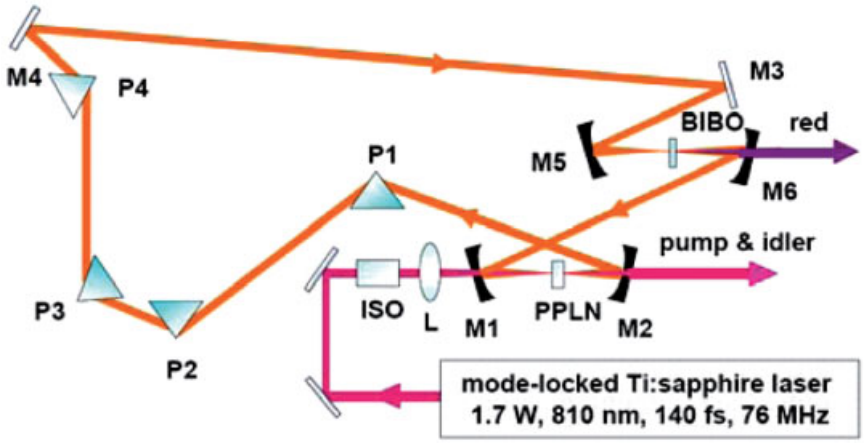

Figure 26 (online color at: www.lpr-journal.org) Schematic of the PPLN femtosecond SPOPO with internal SHG in BIBO for the generation of red pulses.

for this application [119, 121]. The conversion efficiency achieved is similar to that reported in [120] but the pulse durations are roughly 3 times shorter, which would obviously be impossible with PPLN.

5.3. Intracavity SHG in a femtosecond SPOPO

As described in the previous subsection, BIBO is highly suitable for SHG of low-power, high-repetition-rate femtosecond laser sources in the 1600-nm spectral range. This region can be covered with broad tunability using SPOPOs pumped at 800 nm by mode-locked Ti:sapphire lasers. Such a SPOPO can also be developed directly using BIBO as the nonlinear gain material [122]. However, here we present results on intracavity SHG realized with BIBO to provide broadband tuning in the visible (red) using a more conventional SPOPO based on PPLN [123].

The configuration of the femtosecond SPOPO based on PPLN and internally frequency doubled in BIBO is shown in Fig. 26. The SPOPO is pumped by a mode-locked Ti:sapphire laser operating at 810 nm, providing 140-fs pulses at 76 MHz. After transit through an isolator (ISO), the pulses have duration of 185 fs and an average power of 1.51 W. The SPOPO uses a 1-mm PPLN crystal containing eight gratings (Λ = 20.6 to 21.0 µm) and is operated at a fixed temperature of 100 °C to avoid photorefractive damage. The crystal faces are antireflection (AR)-coated ($R < 1\%$) over 1.3–1.6 µm and have high transmission ($T > 95\%$) for the pump. A lens, L, of focal length f = 5 cm and AR-coated ($R < 1\%$) at 810 nm is used to focus the pump beam into the PPLN crystal. To achieve maximum useful output power in the red, the SPOPO cavity is configured in a bifocal ring, comprising four concave reflectors and two plane mirrors. The concave mirrors, M1 and M2 (*RC* = –100 mm), provide the focus for the PPLN crystal, whereas M5 (*RC* = –100 mm) and M6 (*RC* = –75 mm) allow focusing into the BIBO crystal. The plane mirror, M3, is mounted on a translation stage that allows variation of the cavity length with precision of micrometers. All mirrors are highly reflecting ($R > 99\%$) over 1.35–1.55 µm. M1 and M2 are also highly transmitting ($T > 90\%$) at 810 nm. The ring resonator allows extraction of red output in one direction through M6, which has high but variable transmission ($T > 95\%$ to 70%) over 665–785 nm. Dispersion compensation is implemented using two pairs of SF-11 prisms, P1-P4, spaced 28 cm tip-to-tip internal to the OPO cavity.

For internal frequency doubling, we used a 1-mm thick crystal of BIBO in ooe type-I phase matching in *x*–*z* plane, providing high effective nonlinearity and large spectral acceptance, see Fig. 8. The crystal was cut at $\theta = 10°$ for frequency doubling at $\sim$ 1.4 µm at normal incidence. The crystal faces were AR-coated ($R < 1\%$) for the signal wave. The high nonlinearity of PPLN ($d_{\text{eff}} \sim 16$ pm/V) permits simplified wavelength tuning across the red through adjustment of the SPOPO cavity length, only, without the need to vary any other parameters. The PPLN crystal temperature, grating period and position, and pump wavelength all remained fixed.

The BIBO crystal was also maintained at a fixed angle at normal incidence. The spectral acceptance bandwidth for SHG in the 1-mm thick BIBO crystal varies between $\sim$ 19 and $\sim$ 140 nm (calculated at the second harmonic) for fundamental wavelengths from 1.33 to 1.57 µm. We found that the red output could be tuned across the entire 120-nm range of 665–785 nm at a fixed crystal angle by adjusting the cavity delay over 46 µm. It can be expected that the high intracavity fundamental signal intensity permits efficient SHG also away from the exact phase-matching wavelength. A photograph of the femtosecond OPO generating red pulses is shown in Fig. 27.

The static cavity-length tuning avoided the need for realignment of the SPOPO during tuning, resulting in simplified tuning and improved efficiency. The cavity length tuning range is shown in Fig. 28a, and the corresponding red spectra are shown in Fig. 28b, where spectral bandwidths ranging from $\sim$ 2.4 to $\sim$ 5.6 nm are measured. The total tuning range in the red was limited only by the reflectivity of the available SPOPO mirrors at the signal wavelength, and so could be readily extended to longer or shorter wavelengths using better optimized mirror coatings.

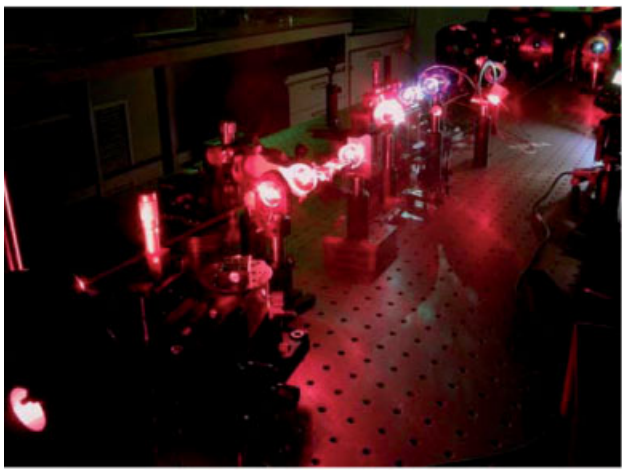

Figure 27 (online color at: www.lpr-journal.org) Photograph of the intracavity frequency-doubled femtosecond SPOPO generating red pulses.

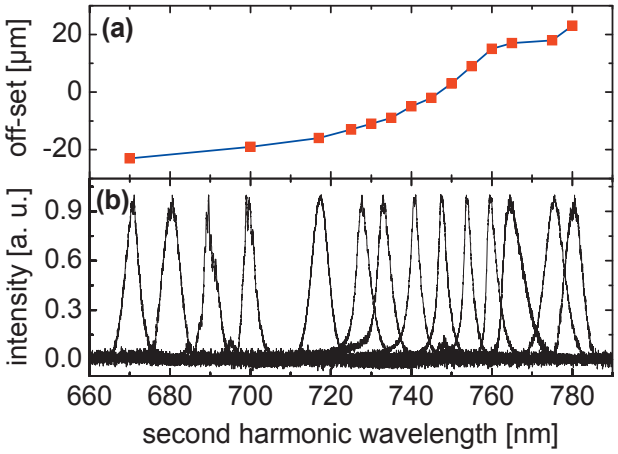

Figure 28 (online color at: www.lpr-journal.org) Cavity length detuning versus second harmonic red wavelength (a) and typical spectra of generated red pulses across the tuning range (b).

Fig. 29 is a plot of the red average output power and conversion efficiency at 670 nm, where the highest power was obtained, versus pump power at 810 nm. The generated red power reaches 260 mW at the maximum available pump power of 1.51 W, corresponding to a conversion efficiency of 17.2%. The pump depletion is 70% at the maximum input pump power of 1.51 W. We were able to generate average powers in excess of 150 mW over ~ 60% and more than 100 mW over ~ 70% of the tuning range. At the extreme of the tuning range at 785 nm, practical powers of 70 mW were still generated. The decline in the generated red power above 770 nm is mainly due to reduction in reflectivity of the cavity mirrors. The pump power threshold for the red SPOPO was 200 mW.

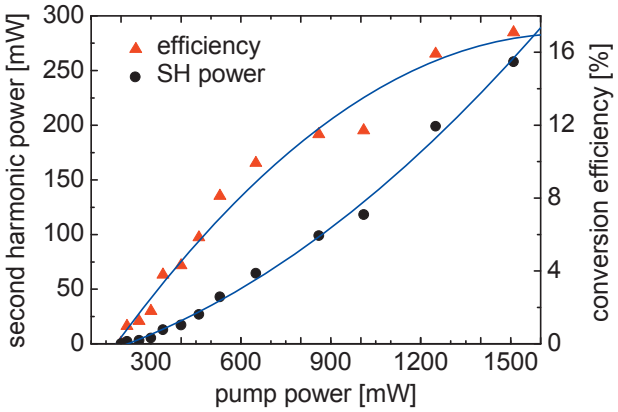

Figure 29 (online color at: www.lpr-journal.org) The generated second-harmonic average power and conversion efficiency at 670 nm versus pump power at 810 nm.

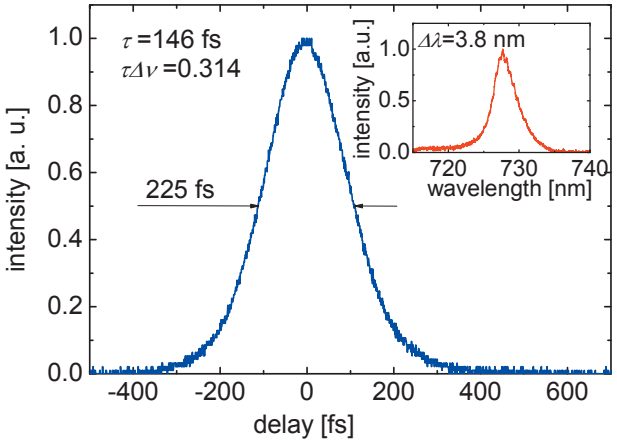

Figure 30 (online color at: www.lpr-journal.org) Intensity autocorrelation trace and spectrum (inset) of the red pulses at 728 nm, indicating transform-limited pulses.

Temporal measurements of the generated red pulses were performed using SHG in a 0.3-mm KDP crystal cut at $\theta = 60°$ for type-I phase matching, recording background-free autocorrelation profiles. The measurements resulted in pulse durations from 140 to 270 fs, with time-bandwidth products from 0.31 to 0.46, implying near-transform-limited pulses. The variation in pulse duration across the tuning range was consistent with the variation in the corresponding spectra in Fig. 28b. A typical autocorrelation profile and spectrum at 728 nm are shown in Fig. 30, confirming a time-bandwidth product of $\tau\Delta\nu = 0.314$ (assuming a sech^2 pulse shape).

6. SPOPO for the visible and UV

The development of SPOPOs operating in the near-IR and pumped near 800 nm by mode-locked Ti:sapphire lasers

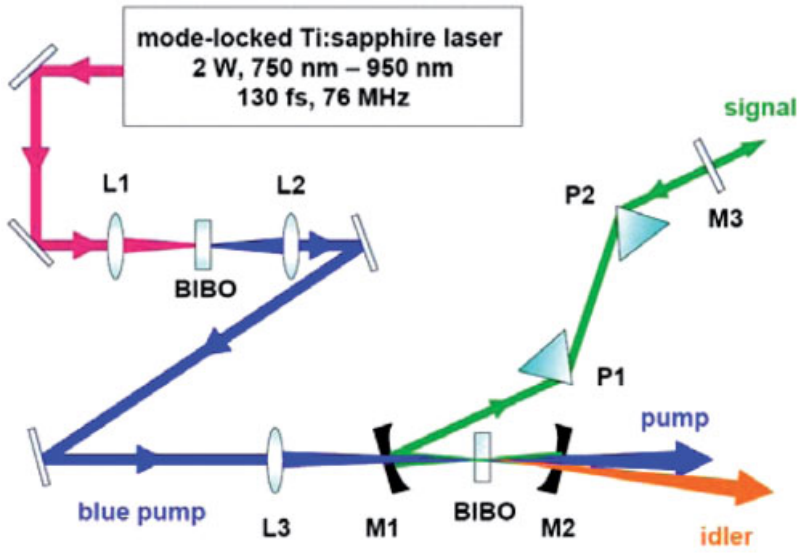

Figure 31 (online color at: www.lpr-journal.org) Configuration of the visible BIBO femtosecond SPOPO pumped by the second harmonic of a mode-locked Ti:sapphire laser in the blue.

using a number of nonlinear crystals, for example PPLN, is now routine. As described in the previous section, the tunability of such SPOPOs can be extended using intracavity SHG, but wavelength coverage cannot be readily extended to the UV range with a further conversion stage. A SPOPO pumped in the UV by the second harmonic of such a Ti:sapphire laser could directly provide femtosecond pulses in the visible with the potential for extension into the UV by intracavity SHG. Such schemes based on BIBO and the experimental results obtained, are presented in this section.

6.1. Femtosecond SPOPO for the visible

The configuration of the visible femtosecond SPOPO is shown in Fig. 31. The SPOPO is pumped in the blue by the second harmonic of a Ti:sapphire laser and exploits BIBO, both as the doubling crystal for the pump (as described in Sect. 5.1) and as the nonlinear gain medium. Using a 1-mm thick uncoated BIBO crystal cut at $\theta \sim 152°$ for SHG in the y–z plane produces an average power > 1 W at 415 nm at $> 50\%$ efficiency. The blue pulses have duration of ~ 220 fs. The blue pump beam is focused to a waist radius $w_0 \sim 25$ µm inside a second BIBO crystal, the gain element for the SPOPO. We use collinear phase matching of the same type as in the SHG process and a crystal cut at $\theta \sim 159°$. From considerations of GVM between the blue pump and visible signal pulses, see Fig. 12b, we chose a 0.5 mm crystal thickness. The crystal faces are AR-coated for signal ($R < 0.5\%$ at 500–700 nm) and have high transmission for pump ($T > 95\%$ at 375–435 nm). The SPOPO is configured in a standing-wave, three-mirror cavity with two concave reflectors (M1, M2: $RC = -100$ mm) and a plane output coupler (M3). The concave mirrors have $> 99\%$ reflectivity for signal wavelengths over 500–680 nm and $> 90\%$ transmission for the pump over 380–450 nm. The mirrors also have $> 80\%$ transmission for the idler over 900–3000 nm, thus ensuring singly resonant oscillation. Two Brewster-cut fused silica prisms provide intracavity GVD compensation.

Fig. 32 shows the visible signal tuning range of the SPOPO at room temperature, as a function of crystal internal angle, obtained at a fixed pump wavelength of 415 nm. The solid curve represents the predicted tuning range for collinear eeo type-I phase matching in the y–z plane obtained using the Sellmeier relations for BIBO, where good agreement between the experimental data and theoretical calculation is evident. The SPOPO can be continuously tuned in the visible across the green-yellow-orange-red, from 480 to 710 nm, by changing the internal angle of the BIBO crystal between $\theta = 175°$ and 154°. The corresponding tuning range of the idler is from 3060 to 999 nm.

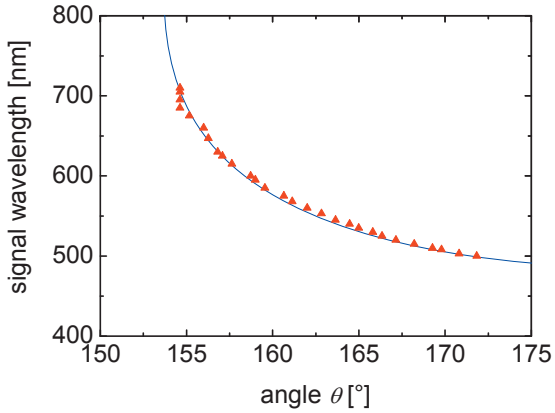

Figure 32 (online color at: www.lpr-journal.org) Visible signal tuning range of the BIBO femtosecond SPOPO as a function of internal angle in the optical y–z plane. The pump wavelength is 415 nm.

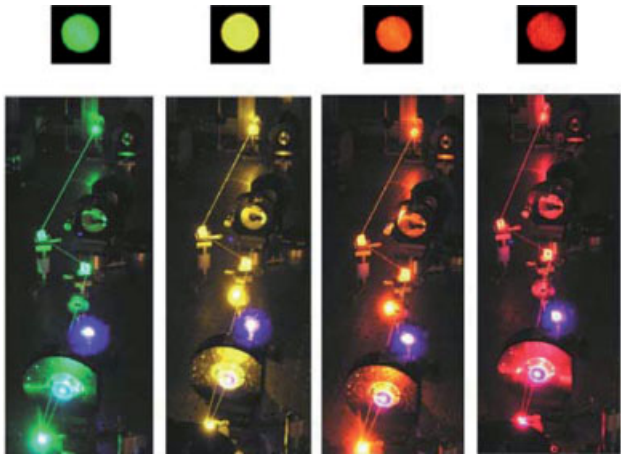

Figure 33 (online color at: www.lpr-journal.org) Photographs of the BIBO SPOPO, with intracavity GVD compensation, oscillating in green, yellow, orange and red.

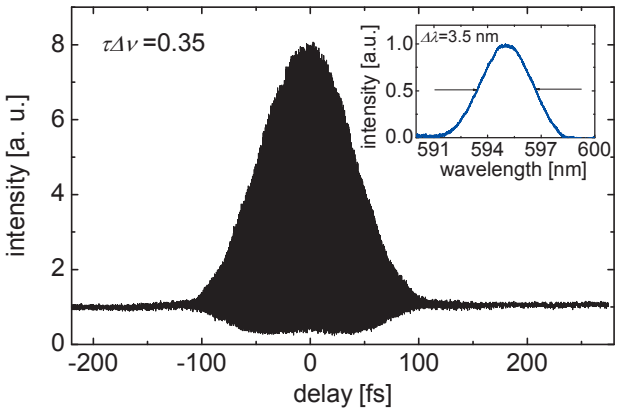

Figure 34 (online color at: www.lpr-journal.org) Typical interferometric autocorrelation and spectrum (inset) of the visible signal pulses at 595 nm with intracavity GVD compensation.

For a given crystal angle, wavelength tuning is also available through the variation of SPOPO cavity length. We typically obtain ~ 10 nm of signal tuning for a change in SPOPO cavity length of ~ 3 µm. The upper wavelength limit for the idler of 3060 nm is indicative of the good transmission of the thin BIBO crystal in this region. Photographs of the SPOPO operating across the green-yellow-orange-red range are shown in Fig. 33.

In order to optimize performance, we operated the SPOPO under different output coupling conditions by using plane mirrors (M3) of different reflectivities at the signal wavelength. The best performance was obtained with an 8% output coupler, where a maximum average signal power of 270 mW was extracted from the SPOPO at ~ 620 nm for 800 mW of blue pump power incident on the BIBO crystal. The SPOPO could provide > 150 mW across 500–700 nm, and > 200 mW across 530–650 nm. At the extremes of the tuning range towards 480 and 710 nm, a visible signal power > 100 mW was still available. The reduction in the signal power at the extremes of the tuning range is attributed to the increasing transmission of SPOPO mirrors away from the center of the tuning curve. With the 8% output coupler, the oscillation threshold was 200 mW (incident on the BIBO crystal), equivalent to a fundamental Ti:sapphire laser power of 650 mW. With a high reflector plane mirror in place of an output coupler, the SPOPO pump threshold was as low as 100 mW, corresponding to a fundamental Ti:sapphire power of 420 mW.

Temporal characterization of the visible signal pulses was performed using autocorrelation measurements in a 0.5-mm thick crystal of BBO cut for type-I phase matching at $\theta = 42^\circ$ and a UV-enhanced Si-photodiode. Without GVD compensation, the signal pulses were strongly chirped, with corresponding broadband double-peaked spectra, characteristic of self-phase modulation (SPM) [124]. Autocorrelation measurements were clearly indicative of chirped pulses, with duration of ~ 170 fs. Due to the effects of SPM, the corresponding spectrum had bandwidth as wide as ~ 15 nm (FWHM), resulting in a time-bandwidth product $\tau\Delta\nu \sim 2.2$, approximately seven times the transform limit for sech^2 pulse shape. We, therefore, implemented GVD compensation by introducing a pair of Brewster-cut fused silica prisms within the SPOPO cavity. Fig. 34 shows the resulting interferometric autocorrelation and spectrum of the visible signal pulses, corresponding to a duration of ~ 120 fs and a spectral bandwidth (FWHM) of ~ 3.5 nm. The time-bandwidth product is now $\tau\Delta\nu \sim 0.35$, indicating near-transform-limited sech^2-shaped pulses.

We note that a similar SPOPO was demonstrated in the 1990s on the basis of noncollinear interaction in BBO that both compensates the spatial walk-off and increases the spectral acceptance enabling the use of crystals as thick as 2 mm [125]. Under very similar pump conditions, the results obtained now with BIBO are, however, superior in terms of efficiency, output power level and wavelength coverage. The main advantage of using BIBO, however, is related to the higher effective nonlinearity, see Fig. 12, which permits collinear interaction, leading to easier cavity alignment and near copropagating pump, signal, and idler.

6.2. BIBO SPOPO for the UV

The tunability of the SPOPO described in the previous subsection can be extended into the UV by SHG of the visible signal pulses. Extracavity SHG in BIBO yielded tunability between 310 and 355 nm [126], but far higher efficiencies can be expected through intracavity SHG. Here, we present the results of intracavity SHG in the BIBO-based SPOPO described above, with BBO as the doubling crystal [127]. The choice of BBO is governed by its deeper UV transparency ($\sim$189 nm) compared to BIBO and higher d_{eff} for UV generation for fundamental wavelengths shorter than ~ 650 nm, see Fig. 8. The modified SPOPO configuration is shown in Fig. 35. The SPOPO is pumped by the

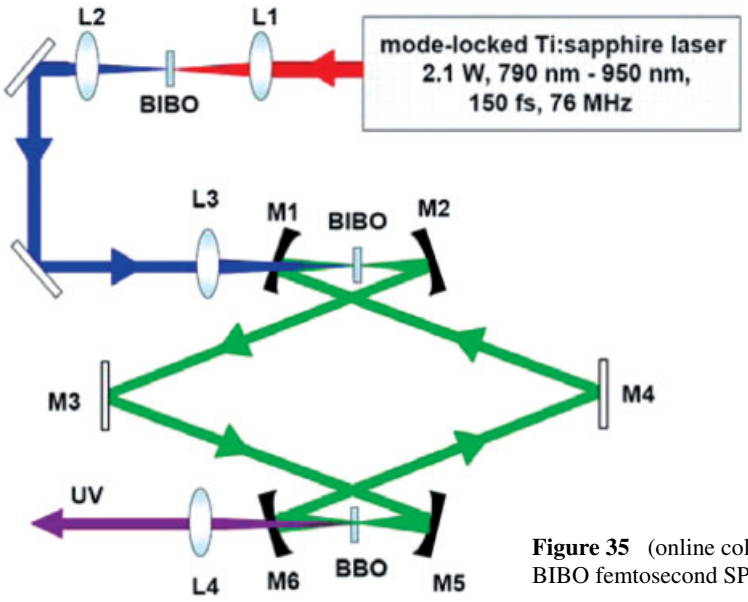

Figure 35 (online color at: www.lpr-journal.org) Configuration of the visible BIBO femtosecond SPOPO with intracavity SHG for the UV generation.

second harmonic of a Ti:sapphire laser at 415 nm, as before. The laser provides 2.1 W of average power at 830 nm in ∼150 fs pulses at 76 MHz. Single-pass frequency doubling in the same BIBO crystal (see previous subsection) provides 1.15 W of average power at 415 nm and a pulse duration of ∼180 fs. To maximize incident pump power, the focusing and collimating lenses, L1 and L2, are AR-coated ($R < 1\%$) in the blue.

The SPOPO resonator is modified by the inclusion of an additional focusing section to accommodate the doubling crystal. The cavity is now configured in a bifocal ring resonator, comprising four concave reflectors (*RC* = –100 mm) and two plane mirrors. The concave mirrors M1 and M2 provide the focus for the SPOPO crystal, whereas M5 and M6 allow focusing into the second-harmonic crystal. Due to geometrical constraints, the angle of incidence on the curved mirrors is limited to $< 7.5^\circ$ to minimize astigmatism. All mirrors are highly reflecting ($R > 99\%$) for the visible signal wavelengths over 500–700 nm. The mirrors M1 and M2 are also highly transmitting ($T > 90\%$) for the blue pump over 380–450 nm. The ring resonator allows the generation of the UV output in one direction through M6. To allow maximum UV extraction, M6 also has high, but variable transmission ($T \sim 70\%$ to 90%) over 250–350 nm.

The blue pump beam is focused with L3 to a beam waist radius, $w_0 \sim 25\,\mu$m, inside the SPOPO crystal. The nonlinear crystal for the SPOPO is BIBO, similar to that used in the previous subsection, but 0.4-mm thick. The BBO crystal used for SHG was 0.5-mm thick, cut at $\theta = 42^\circ$ for type-I phase matching, providing an effective nonlinear coefficient, $d_{\text{eff}} \sim 1.4$–1.8 pm/V, across the fundamental signal tuning range. The crystal faces were AR-coated for the signal over 500–700 nm ($R < 1\%$) and for the generated UV light over 250–350 nm ($R < 8\%$).

Wavelength tuning in the UV was achieved by continuous tuning of the SPOPO signal across the visible through angular rotation of the BIBO crystal and simultaneous angular tuning of the BBO SHG crystal. At each wavelength, the cavity was optimized to compensate for any lateral shifts due to angular tuning or changes in synchronous length in order to achieve maximum UV output. The SPOPO signal could be tuned across 500–710 nm by changing the internal BIBO crystal angle from $\theta = 171.5^\circ$ to 154.5°, with the corresponding UV wavelength range covering 250 to 355 nm for a change in the internal angle of the BBO crystal from $\theta = 52.3^\circ$ to 33.1°. The limit to the obtained tuning range in the UV was set by the overall reflectivity of the cavity mirrors at the signal wavelength. By using mirrors with broader reflectivity band and shorter pump wavelengths near 400 nm, full coverage across 230–360 nm should be readily attainable. A photograph of the frequency-doubled SPOPO is shown in Fig. 36.

The simultaneously recorded spectra of the visible signal and the corresponding second harmonic in the UV are shown in Fig. 37. As can be seen from Fig. 37a, the visible signal spectral widths typically vary between ∼ 3 nm and ∼ 3.5 nm. At shorter signal wavelengths in the green, however, the bandwidth is significantly broadened to ∼ 8 nm, which we attribute to the net SPOPO cavity dispersion conditions in this range in the absence of intracavity GVD compensation. Combined with SPM, this leads to spectral broadening and chirping of the signal pulses in the green. Nevertheless, the generated UV spectra exhibit consistent behavior, with bandwidths ranging from ∼ 0.5 nm to ∼ 1 nm across the tuning range. The bandwidth reduction from the visible to the UV is attributed to the limited SHG spectral acceptance of BBO.

The calculated spectral acceptance bandwidth for SHG in the 0.5-mm BBO crystal varies from ∼ 1 nm to ∼ 5 nm (at the fundamental) over the signal wavelength range of 500 to 700 nm, implying stronger spectral narrowing at shorter signal wavelengths. Accordingly, one would expect

Figure 36 (online color at: www.lpr-journal.org) Photograph of the blue-pumped BIBO femtosecond SPOPO oscillating in the red, with intracavity frequency doubling in BBO to provide output pulses in the UV.

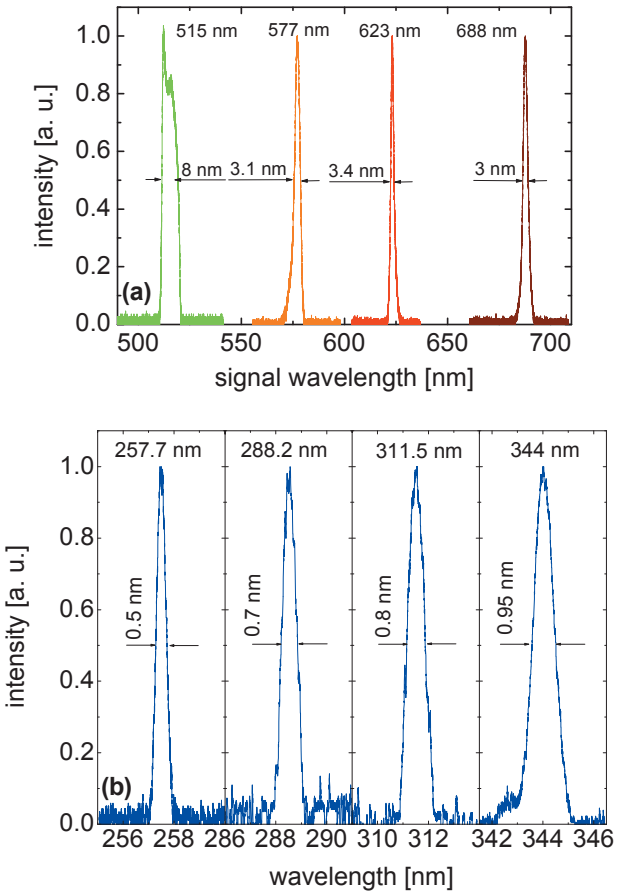

Figure 37 (online color at: www.lpr-journal.org) Typical spectra of the visible signal pulses across the SPOPO tuning range (a), and the corresponding generated second harmonic spectra in the UV (b).

stronger reduction in the UV spectral bandwidths towards the shorter wavelengths. This is qualitatively supported by the recorded spectra in Fig. 37b.

We were able to generate UV average powers in excess of 175 mW over ∼70% of the tuning range (275–350 nm) and more than 100 mW over ∼80% of the tuning range (270–355 nm). In the wavelength range of 255–270 nm, practical powers of 25 to 100 mW were still generated, with 5 mW available at 250 nm. We believe the decline in the generated UV power below 270 nm is mainly due to the spectral broadening and chirping of visible signal pulses in the green as described above. Together with the decrease in spectral acceptance for phase matching in BBO towards shorter wavelengths, this results in reduced UV power in these regions.

The highest UV average power was obtained at 323 nm. Fig. 38 is a plot of the generated UV power and conversion efficiency at 323 nm versus pump power at 415 nm. The generated UV power can be seen to increase almost linearly, reaching 225 mW at the maximum available blue power of 1.15 W, representing a conversion efficiency of

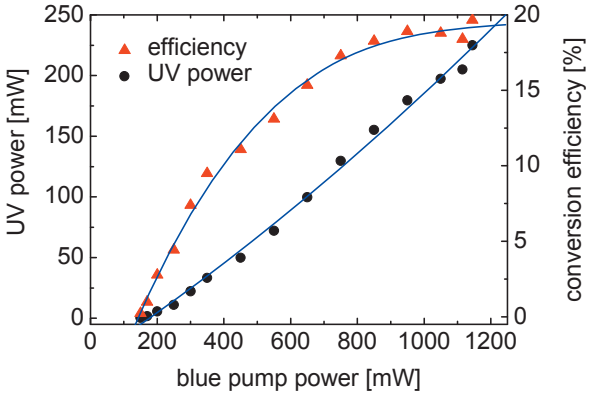

Figure 38 (online color at: www.lpr-journal.org) Variation of average UV output power and conversion efficiency at 323 nm with blue pump power at 415 nm.

19.7%. The UV power of 225 mW is close to the maximum visible signal power of 270 mW extracted directly from the SPOPO (see previous subsection), implying that

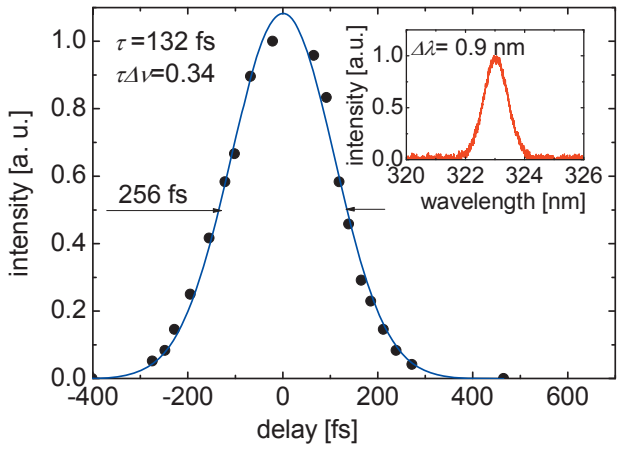

Figure 39 (online color at: www.lpr-journal.org) Cross-correlation trace, and spectrum (inset) of the generated UV pulses at 323 nm.

the intracavity SHG acts as an almost optimized nonlinear coupler for the signal. Given the linear rise in power and no evidence of saturation, we can expect higher UV output powers in excess of 225 mW with higher input pump powers.

The short lengths of BIBO and BBO crystals resulted in minimum beam distortion arising from the effects of spatial walk-off, tight focusing or cavity astigmatism, so that the UV output beam had close to a circular profile with a $M^2 < 1.1$. The blue pump power threshold for the frequency-doubled SPOPO was as low as 150 mW, equivalent to a fundamental Ti:sapphire laser power of 600 mW.

Temporal characterization of the generated UV pulses was performed using the cross-correlation technique and a GaAsP detector. The UV pulses were mixed with 150-fs Ti:sapphire fundamental pulses at 830 nm in a 0.5 mm thick type-I BBO crystal cut at $\theta = 26°$. The GVM in this crystal was taken into account in the evaluation of the pulse duration. A typical cross-correlation trace and the corresponding spectrum at 323 nm are shown Fig. 39, confirming a near-transform-limited pulse with a time-bandwidth product $\tau.\Delta\nu \sim 0.34$, assuming a sech^2 pulse shape. Across the UV tuning range, pulse durations of 132 to 250 fs were measured, with corresponding time-bandwidth products varying from ~ 0.34 to ~ 0.6.

7. Femtosecond OPGs and OPAs pumped near 800 nm

In this section, we present experimental results on one- and two-stage OPAs based on different combinations of BIBO crystals (type-I and type-II), seeded by a white-light continuum (WLC) or unseeded (OPG), in which the process is initiated by parametric fluorescence. These devices operate at 1 kHz and deliver tunable femtosecond pulses with high single pulse energy and peak intensity.

7.1. Broadly tunable type-II BIBO OPA

Many applications of amplified femtosecond sources generally require broad tunability, while some require high energy and very short pulses. Although several different system configurations and nonlinear crystals have been exploited in the past, at present the material of choice for use in near-IR OPG/OPAs, and in particular in commercial devices with 800 nm pumping, is type-II BBO [110]. This is due to several attractive features, the most important being the possibility to tune, even close to degeneracy, with almost constant signal and idler bandwidth. The same holds for type-II interaction in BIBO, as can be seen from Fig. 11, with the advantage of offering higher effective nonlinearity. For the oeo type-II interaction in BIBO, the nonlinear figure of merit that enters the exponential gain in Eq. (5), $\mathrm{FM} = d_{\mathrm{eff}}^2/n_{\mathrm{P}}n_{\mathrm{S}}n_{\mathrm{I}}$, is roughly twice that of BBO, and changes by less than $\pm 10\%$ across the whole tuning range (Fig. 11a).

It can be seen from Fig. 11b that, as with BBO, for a pump wavelength of 800 nm, BIBO also exhibits the property that the signal and idler waves travel in opposite directions relative to the pump, which ensures exponential growth of the parametric gain even beyond the pulse temporal walk-off length [109]. In accordance with Fig. 11b, in comparison to BBO, shorter crystals of BIBO should be used in the femtosecond regime, which somewhat diminishes the advantage of a higher effective nonlinearity. Nevertheless, the use of shorter crystals helps avoid undesirable higher-order nonlinear processes and better utilizes the transparency window of the material. Since, in the case of down-conversion, the limiting factor is the mid-IR cut-off edge, it can be expected that shorter crystals of BIBO will permit wider tunability. Indeed, idler absorption limits the tunability with BBO to below 3 µm, for example a maximum of 2.7 µm was reported in [128], or even shorter (2.5 µm) in commercial devices. On the other hand, the spectral range near 3 µm is very important for molecular spectroscopy. The transmission cut-off can be circumvented by employing other nonborate crystals such as KTP in a second stage, but the generation of short pulses in such materials is difficult [129].

To study broadly tunable OPA based on type-II BIBO, two uncoated samples were available, both cut at $\theta = 42°$ in the x–z optical plane, with an aperture of $7 \times 7\,\mathrm{mm}^2$ and thicknesses of 3 and 5 mm. The measured transparency for polarization parallel to the y principal optical axis (o-polarization with respect to the x–z plane), in particular near the long-wave edge, is indeed higher for the thinner crystal [82]. Comparing with BBO [130], one can conclude that although, for the same thickness, the absolute upper limits for the transmission are similar, BBO exhibits an absorption feature near 2.4 µm.

We compared BIBO and BBO in a modified setup comprising a commercial double-pass OPA seeded by WLC (Clark-MXR), shown in Fig. 40. The WLC is generated in a 2-mm thick sapphire plate, which is simultaneously used to achieve the correct polarization. A polarizer between the

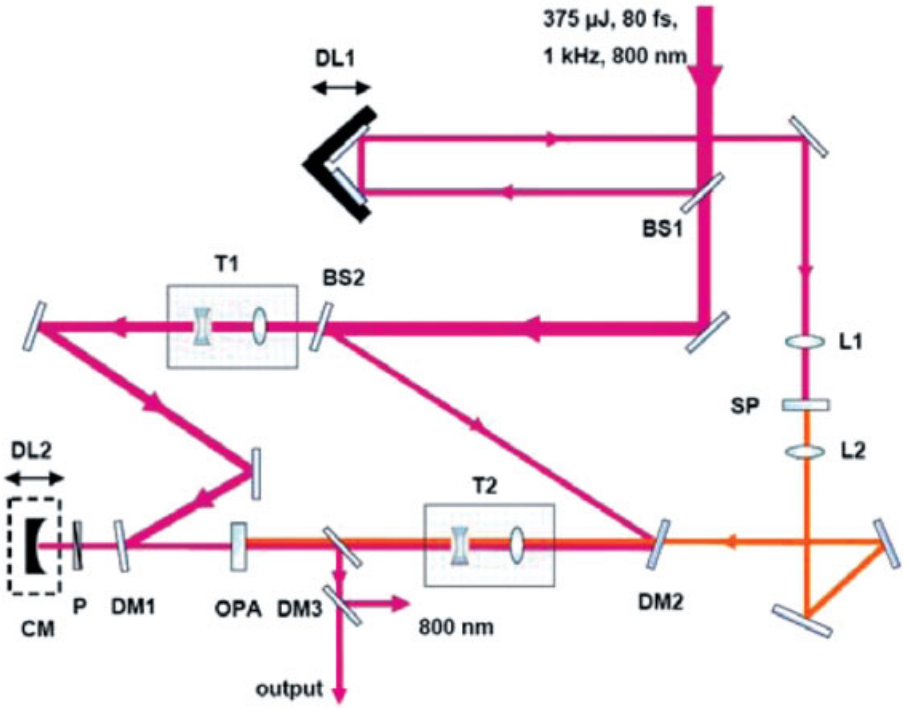

Figure 40 (online color at: www.lpr-journal.org) Experimental setup of the WLC-seeded type-II OPA: L, lenses, T, telescopes, BS, beam splitters, DM, dichroic mirrors, DL, delay lines, SP, sapphire plate, CM, curved mirror with 30 cm radius of curvature.

two passes through the nonlinear crystal serves to select the signal wavelength for seeding the second pass. The pump energy used for the second pass was 300 µJ. Finally, the signal and idler pulses are coupled out using a mirror slightly displaced in the uncritical direction.

Using a standard BBO crystal, 5 mm thick but AR-coated, the tunability extended from 1180 to 2500 nm with a maximum output level of 80 µJ (signal plus idler) for a pump energy of 375 µJ. Such overall conversion efficiencies (on the order of 20%) are typical for tunable femtosecond OPG/OPA based on type-II BBO [128]. The 5-mm thick BIBO crystal provided higher output energy than the 3-mm thick sample, but the temporal and spectral characteristics were not satisfactory. Specifically, depending on wavelength, the signal and idler pulses were either structured or longer than 200 fs, as a result of the pulse splitting and reconversion. Thus, it can be concluded that the larger GVM in BIBO, see Fig. 11b, certainly requires the use of shorter crystals than in the case of BBO.

With the 3-mm thick BIBO crystal, we were able to obtain sub-200 fs pulse durations throughout the whole tuning range (Fig. 41). The pulse duration was estimated by fitting cross-correlation traces obtained by SFG with a reference pulse at 800 nm, using a 0.7-mm thick type-I BBO crystal. Gaussian pulse shapes were assumed and the time-bandwidth product was estimated by measuring the pulse spectra with a multichannel analyzer equipped with a 128-element pyroelectric array. In principle, the range of pulse durations obtained with the 3-mm thick BIBO was similar to the results with the standard 5-mm thick BBO crystal, but the dependence on wavelength was different. The shorter signal and idler pulse durations obtained in the limits of

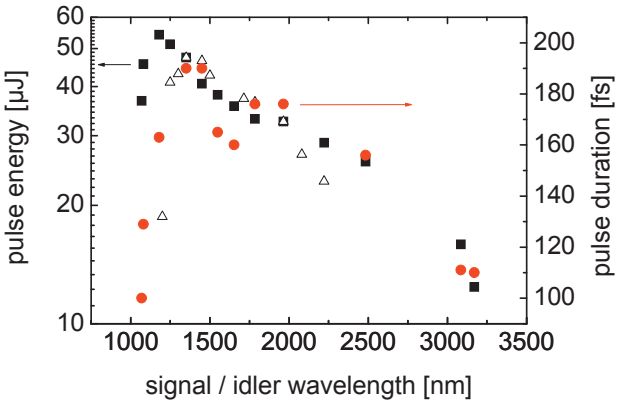

Figure 41 (online color at: www.lpr-journal.org) Pulse energy (full squares) and pulse duration (FWHM) assuming Gaussian pulse shapes (full circles) for the BIBO based OPA using a 3-mm thick sample. The open triangles show the energy obtained with the standard AR-coated 5-mm thick BBO crystal.

the tuning range in BIBO (Fig. 41) can be explained by the increasing acceptance bandwidth, see Fig. 11b.

The main advantage of BIBO appears to be the possibility to have a somewhat broader tuning range extending slightly beyond 3 µm, while under the same conditions the tuning with BBO had an upper limit of ≈ 2.5 µm, Fig. 41. Although the maximum energy level obtained with BIBO was on the same order of magnitude (80 µJ for signal plus idler), the internal conversion efficiency was clearly higher (more than 30% at maximum for the second pass), because this sample was uncoated.

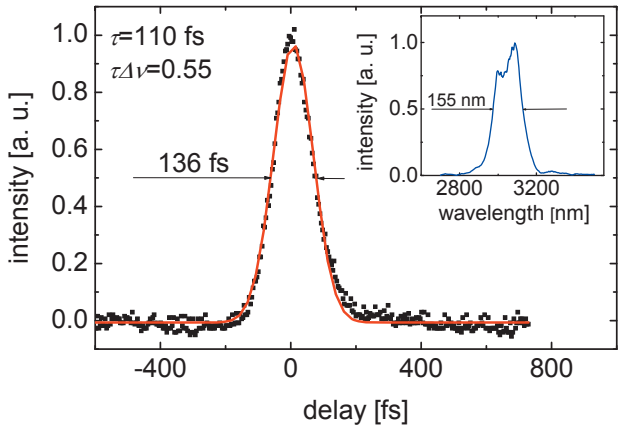

Figure 42 (online color at: www.lpr-journal.org) Cross-correlation trace of the idler pulses at 3050 nm obtained by SFG with a reference pulse at 800 nm (black symbols) and a Gaussian fit (red line). The inset shows the corresponding idler spectrum.

Fig. 42 shows a cross-correlation function of the idler pulses at 3050 nm (black symbols) from the FWHM of which (136 fs) a pulse duration of 110 fs is obtained by a fitting procedure (red curve). The time-bandwidth product is $\tau\Delta\nu = 0.55$, somewhat above the Fourier limit of 0.44 for Gaussian pulse shapes (it is ≈ 0.5 for the pump pulses). The pulses at the signal wave (1085 nm) are slightly shorter having a FWHM duration of 100 fs.

Note that the comparison of BIBO and BBO in this section was performed under the rather restricted conditions offered by an existing commercial device. In a different experiment, the use of two separate stages and a more powerful pump source resulted in 56% total (signal plus idler) internal conversion efficiency in the second BIBO stage, corresponding to about 1.1 mJ of total output energy at 1 kHz [131]. These results serve as a basis for the first commercial device of that kind based on BIBO.

7.2. High-energy type-II / type-I BIBO OPA

Enhancement of output energy from an OPA clearly requires more flexibility on the pumping conditions for the two stages and their separation. A well-known concept in multistage amplifiers (both laser and parametric) is to define the spectral properties and tune the wavelength through the first stage, then use a broadband amplifier in the second stage. This can be realized using a type-II BIBO crystal in the first and a type-I BIBO crystal in the second stage. Note that ooe type-I phase matching in BIBO is characterized by higher (≈ 1.3 times) effective nonlinearity than oeo type-II interaction, which is also almost constant ($< 3\%$ variation) across the whole tuning range, see Fig. 10a.

The experimental setup for such a high-power OPA is shown in Fig. 43. The OPA is pumped by a home-made Ti:sapphire amplifier system that provides pulses of 135 fs duration (Gaussian shape assumption) with an energy of up to 12 mJ [132]. A maximum pump pulse energy of 5 mJ (average power of 5 W) was used, limited by the available aperture of the nonlinear crystals. The central wavelength of the pump pulses was near 807 nm and their spectral width corresponded to a time-bandwidth product of 0.62.

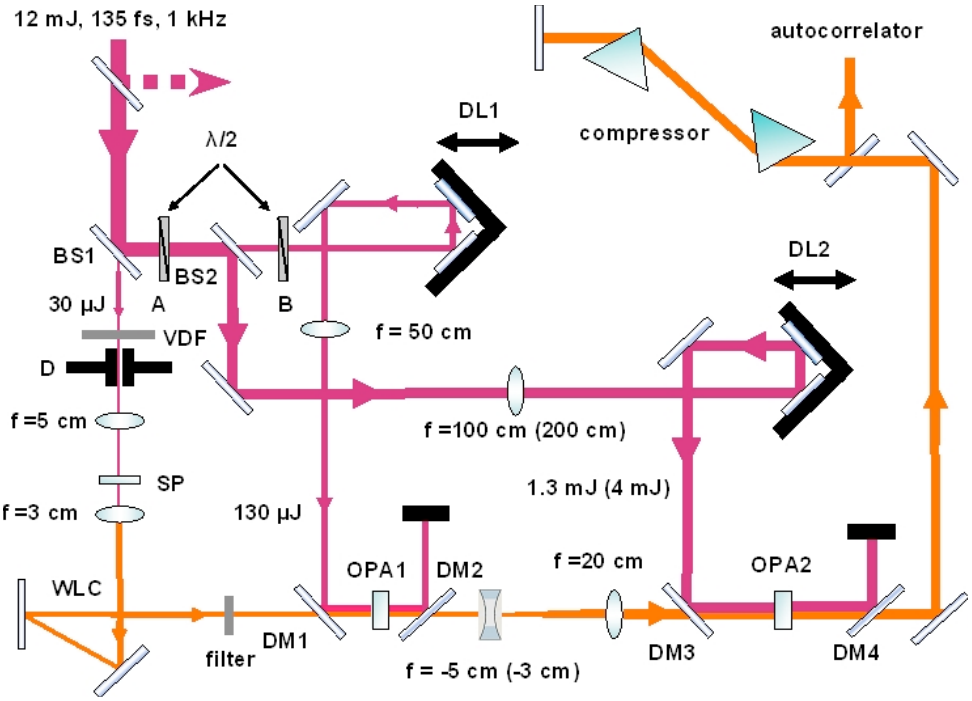

Figure 43 (online color at: www.lpr-journal.org) Schematic of the experimental setup: OPA1 and OPA2, first and second OPA stages, BS, beam splitters, DL, delay lines, D, diaphragm, VDF, variable density filter, SP, sapphire plate. The parameters in brackets refer to the high-power version; A and B denote two possible positions of the same half-wave plate ($\lambda/2$).

Using the beam splitter, BS1, the fundamental pulse energy is divided into two parts. The main part is reserved for pumping the two OPA stages, and a small part is directed to the WLC generation line. After passing through a variable-density filter (VDF) and a diaphragm, less than 20 µJ is focused into a 2-mm thick sapphire plate to produce a stable, single-filament WLC. A second lens is used after the sapphire plate for imaging the WLC onto the first stage BIBO crystal. The Stokes spectral portion of the WLC, for seeding the first OPA stage at the signal wavelength, is selected using a thin long-pass filter (Fig. 43). The part of the fundamental power, which is reflected from BS1, is divided by the second beam splitter, BS2, into two parts for pumping the two stages of the OPA. The dichroic mirrors, DM1-DM4, highly reflective ($R > 99\%$) for the pump and highly transmitting ($T > 90\%$) for the signal and idler wavelengths, are used for collinear recombination and separation of the beams. In the first stage we employed the 3-mm thick type-II BIBO crystal described in the previous subsection. The type-I BIBO crystal available for the second stage was 6-mm thick, also uncoated, with an aperture of $10 \times 10\,\text{mm}^2$. It was cut at $\theta = 11.4^\circ$ in the x–z principal plane.

The first OPA stage was pumped with an energy of 130 µJ and the position of the type-II BIBO crystal was adjusted in such a way that it was as close as possible to, but sufficiently far in front of, the focus of the $f = 50\,\text{cm}$ pump lens (Fig. 43), in order to avoid OPG operation. The output of the first OPA stage (signal plus idler) amounted to several µJ, depending on wavelength. The second BIBO crystal was placed about 45 cm away from the first stage. Without any additional polarization elements, the second OPA stage could be seeded either only by the amplified signal or only by the generated idler in the first OPA stage. This is a consequence of the fact that different types of interaction are used in the two OPA stages. Initially, we attempted seeding of the second OPA stage at the signal wavelength. In this case, the half-wave plate (Fig. 43) is in position A in order to rotate the pump polarization from horizontal to vertical, that is perpendicular to the polarization of the WLC, for both OPA stages.

In the low-energy regime of this experiment, the second OPA stage was pumped by 1.3 mJ and the pump beam was loosely focused by an $f = 100\,\text{cm}$ lens (Fig. 43). Its shape at the position of the BIBO crystal was slightly elliptical with larger diameter in the horizontal plane. The spot size resulted in a peak axial intensity of $\approx 25\,\text{GW/cm}^2$. The telescope between the two stages consisted of two lenses of $f = -5\,\text{cm}$ and $f = 20\,\text{cm}$ (Fig. 43). In this case, it was possible to avoid direct seeding of the second stage by the WLC, which occurs at slightly different wavelengths and pump delay (for the second stage) across the whole tuning range, by appropriate imaging of the WLC source with the $f = 3\,\text{cm}$ collimating lens after it (Fig. 43). The diameter of the seed beam in the position of the second OPA stage was on the order of 4–5 mm. The maximum output energy (signal plus idler) was about 350 µJ near $\lambda_S = 1200\,\text{nm}$, decreased to about 300 µJ at shorter wavelengths ($\lambda_S = 1170\,\text{nm}$) and to 260 µJ close to degeneracy. Thus, the maximum conversion efficiency for this stage was about 27%, or $\approx 34\%$ intrinsic efficiency, taking into account that the crystal is uncoated.

The temporal and spectral characterization was performed by autocorrelation measurements using SHG in a 0.1-mm thick type-I BBO crystal and a multichannel analyzer (see previous subsection). We also recorded autocorrelation traces after transmitting the signal pulse through the prism pair (double-pass) depicted in Fig. 43. This compressor consisted of two 59° SF11 prisms aligned for minimum deviation (about 80% overall transmission), with vertical offset for input/output decoupling. This glass material is suitable only for the signal pulses and so we took care to have a minimum glass path, operating just in the vicinity of the apex, by translating the second prism together with the retroreflector relative to the first prism. The separation between the prisms was optimized by monitoring THG in air or continuum generation in a fused silica plate using an $f = 10\,\text{cm}$ lens.

We characterized the low-power mode of operation at two signal wavelengths: $\lambda_S = 1200$ and 1400 nm. At $\lambda_S = 1400\,\text{nm}$, the wavelength dependence of the parametric gain bandwidth is only weakly pronounced for both stages. In comparison to operation near $\lambda_S = 1200\,\text{nm}$, the spectral acceptance is narrower for the first stage and broader for the second stage. Near 1200 nm, the shortest pulses obtained directly from the OPA were 105 fs (FWHM, assuming Gaussian pulse shapes), roughly 20% shorter than the pump pulses, and the spectral width (26 nm) resulted in a time-bandwidth product of $\tau\Delta\nu = 0.57$, very similar to that of the pump pulses.

Applying the prism compressor, we were able to shorten the signal pulses down to 92 fs, which resulted in improvement of the time-bandwidth product down to $\tau\Delta\nu = 0.5$. The autocorrelation trace, the Gaussian fit, and the spectrum are shown in Fig. 44a. The performance of the OPA at $\lambda_S = 1400\,\text{nm}$ was very similar. In general, the optimum prism separation was critically dependent on the alignment of the OPA. Hence, given the modest compression factors achieved, we did not implement the compressor in the high-power regime.

In order to study the potential for energy scaling, the pump energy for the second stage was increased to 4 mJ. Exchanging the beam splitters, it was possible to preserve the same pumping conditions for the WLC generation and the first OPA stage. The focal length of the lens used for pumping the second stage was increased to 200 cm, with the distance from this lens to the second OPA stage being about 100 cm. Simultaneously, the negative lens of the telescope used for expansion of the seed beam from the first OPA stage (Fig. 43) was substituted by another lens with $f = -3\,\text{cm}$, in order to better match the pump beam cross-section at the position of the second OPA stage. The pump beam completely filled the aperture of the BIBO crystal used in the second OPA stage. Its spatial distribution was somewhat elliptical but very close to Gaussian, with the corresponding fits resulting in a FWHM (intensity) of

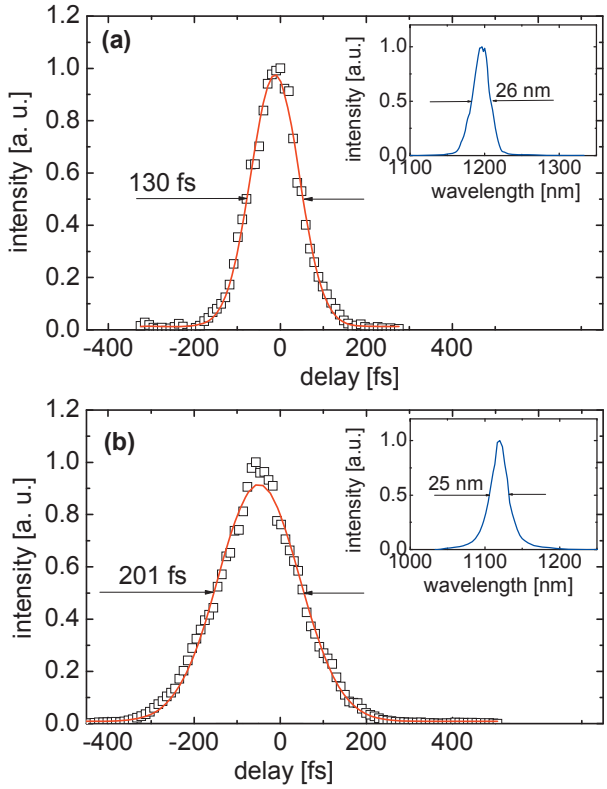

Figure 44 (online color at: www.lpr-journal.org) Autocorrelation trace (symbols) and Gaussian fit (curve) of the compressed signal pulse at 1200 nm from the low-power OPA (a). The inset shows the corresponding spectrum. Autocorrelation trace (symbols) and Gaussian fit (curve) of the signal pulse at 1120 nm from the high-power OPA with seeding at the signal wave (b). The inset shows the corresponding spectrum.

10.1 mm in the horizontal and 6.5 mm in the vertical plane. This results in a peak on-axis intensity of $\sim 40\,\mathrm{GW/cm^2}$.

By continuing to seed with the signal pulse from the first OPA stage, the maximum energy obtained from the second OPA stage reached 1.1 mJ (signal plus idler) near $\lambda_S = 1200\,\mathrm{nm}$. The output was also somewhat elliptical with horizontal and vertical beam diameters of ~ 7 and ~ 4.5 mm, respectively. The signal spectra recorded had a short-wave shoulder, and the autocorrelation traces indicated the presence of satellite pulses and/or a longer pedestal. This was a consequence of simultaneous direct seeding of the second OPA stage by the WLC, at the same position of the delay lines. This effect was absent only in the limits of the tuning range, for signal wavelengths approaching 1100 nm. Fig. 44b shows the recorded signal spectrum (inset) and the corresponding autocorrelation function at $\lambda_S = 1120\,\mathrm{nm}$, where the total output energy (signal plus idler) amounted to 1 mJ, corresponding to an intrinsic conversion efficiency of $\approx 32\%$ for the second stage. The deconvolved pulse duration, assuming a Gaussian pulse shape, was ~ 140 fs (FWHM), resulting in a time-bandwidth product of $\tau\Delta\nu = 0.85$.

At longer signal wavelengths, the contribution of the direct seed from the WLC stage continuously increased and near 1300 nm it became the main factor in determining the output energy from the second OPA stage. In the high-power regime, it was not possible to eliminate this effect by modifying the imaging of the WLC and the seed from the first stage, because of the large gain bandwidth of the second stage. The restrictions are also related to the fact that the second OPA stage is operated at relatively high gain. One possibility to avoid this is to introduce an intermediate OPA stage, but this would greatly increase complexity. The second possibility, which is more elegant, is to seed the second OPA stage only by the idler generated in the first OPA stage. This was realized by simple translation of the half-wave plate to position B in Fig. 43, and rotation of the ooe type-I BIBO crystal by 90°. Thus, the WLC has the same extraordinary polarization (in the horizontal plane) as the pump for the second OPA stage, and so no phase matching is possible.

In general, seeding at the idler wavelength produced an energy output that was roughly 80% of the total output when seeding at the signal wavelength. Thus, near $\lambda_S = 1200\,\mathrm{nm}$, the total output energy when seeding with the idler from the first OPA stage amounted to 850 µJ. Towards degeneracy the energy declined to roughly 600 µJ. The spectra measured at two signal-idler pairs are shown in Fig. 45a. In Fig. 45b the corresponding autocorrelation traces with their FWHM are presented. The latter were well fitted by Gaussian profiles. The resulting pulse durations were almost constant, varying only from 133 to 139 fs, that is very close to the pump-pulse duration. The time-bandwidth products near degeneracy (see Fig. 45b) were also very close to the product for the pump pulses, but away from degeneracy they were slightly larger. The values correspond to roughly 1.5–2 times the Fourier limit for Gaussian pulses.

7.3. High-power sub-30 fs pulses with type-I / type-I BIBO OPA

Extremely short high-energy laser pulses in the near-IR are of special interest for a variety of applications in nonlinear optics and time-domain spectroscopy. Generation of pulses as short as 14.5 fs at 1.5 µm and with energies of about 12 µJ (signal plus idler) has been previously reported using BBO [133]. Further scaling of such a system is limited by the damage threshold of the fiber used for the spectral broadening of the pump pulses in the compressor stage. Also, 200-µJ, 15-fs phase-stable pulses at 1.5 µm were produced by DFG of a hollow-fiber broadened supercontinuum followed by two-stage BBO-based OPA pumped by 50-fs pulses. Beside the complex setup, the need to generate broadband supercontinuum in this work makes the availability of short pump pulses (not much longer than 50 fs) essential [134]. In a noncollinear, blue pumped OPA, sub-50 fs idler pulses tunable across the spectral range of

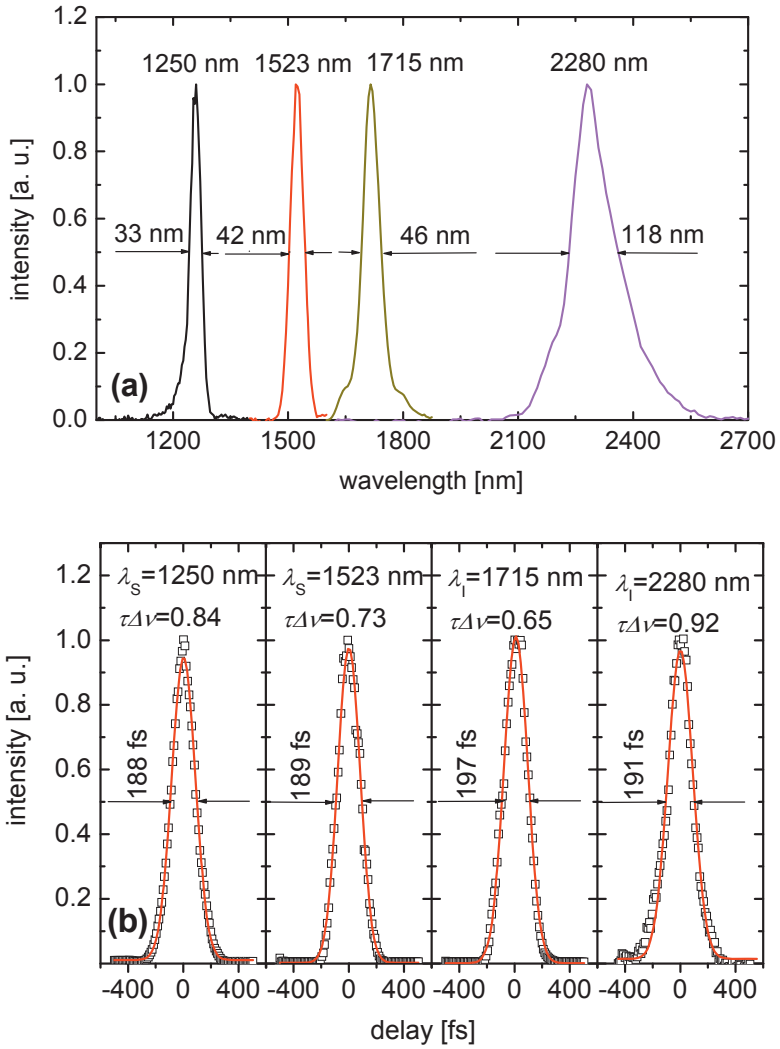

Figure 45 (online color at: www.lpr-journal.org) Spectra of the high-power OPA with idler seeding, recorded for two signal-idler pairs at a total output energy of 600 µJ (near degeneracy) and 800 µJ (away from degeneracy) (a). Autocorrelation traces (symbols) and Gaussian fits (curves) with FWHM for the signal and idler pulses (b), corresponding to the spectra from (a). The time-bandwidth products are also given in the figure.

900–1600 nm, with microjoule energy level [135,136], have been generated. More recently, with a quasi-collinear BBO OPA, 8.5-fs pulses at 1.6 µm have been obtained using a deformable mirror in the compression stage, but the energy did not exceed 3 µJ [137].

In all these experiments, BBO was deployed as the nonlinear crystal. From the analysis of the spectral bandwidth properties in Sect. 4, it is clear that ooe type-I BIBO is an ideal candidate for obtaining very short pulses when pumping near 800 nm. Here, we present experimental results using such crystals in both stages of a collinear OPA seeded by WLC. The setup, shown in Fig. 46, is similar to that in Fig. 43, using the same pump source at 807 nm and 1 kHz, adjusted to a pulse duration of ∼150 fs. The pulse energy used is about 1.8 mJ. The crystals deployed in both stages are 3 mm thick, uncoated BIBO cut at $\theta = 11.4°$ in the x–z plane, the second sample having an aperture of $10 \times 10\,\mathrm{mm}^2$.

The beam splitter, BS1, transmits only a small fraction of the total pump energy to the WLC generation line. The main portion of the fundamental power, which is reflected from BS1, is divided by the second beam splitter, BS2, into two parts for pumping the two stages of the OPA. About 200 µJ of the fundamental pulse energy is focused onto the first BIBO stage using an $f = 50$ cm lens. The characterization of the generated signal and idler pulses was performed using a SHG frequency-resolved optical gating (SHG FROG) technique [138].

Spectral and temporal behavior of the WLC amplified in the first stage strongly depends on the signal wavelength. For $1150\,\mathrm{nm} < \lambda_S < 1300\,\mathrm{nm}$, well-defined spectra with a 30–100-nm bandwidth, increasing with wavelength, and pulse energies exceeding 5 µJ, are achieved. Starting from 70 fs near 1150 nm, the signal pulses become shorter down to 40 fs with increasing wavelength, which is to be expected given the closer group velocity matching with the pump, see Fig. 10b. At signal wavelengths exceeding 1300 nm, the behavior changes dramatically: Firstly, the WLC energy decreases, and in order to produce sufficient signal energy for seeding the second OPA stage, the pump intensity should be increased by moving the crystal closer to the focal point. Secondly, because of the broader spec-

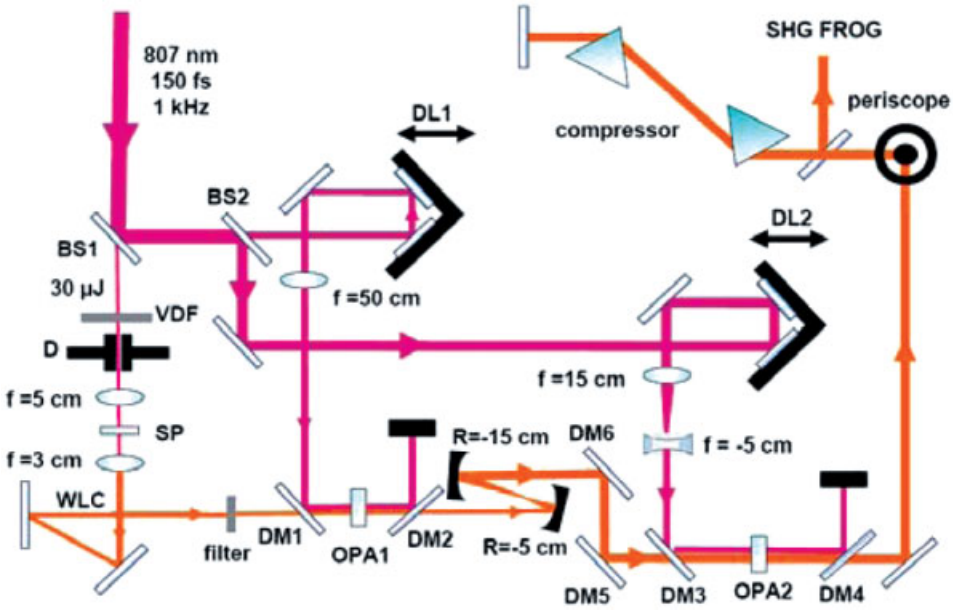

Figure 46 (online color at: www.lpr-journal.org) Schematic of the experimental set-up: OPA1 and OPA2, first and second OPA stages, BS, beam splitters, DL, delay lines, D, diaphragm, VDF, variable density filter, SP, sapphire plate, WLC, white-light continuum, DM, dichroic mirrors.

tral acceptance of BIBO in this range (see GVM between signal and idler in Fig. 10b), smooth wavelength tuning is no longer possible and a broad spectrum with limited tunability near ∼1400 nm is selected by the crystal. At this wavelength, the negligible GVD of BIBO (∼ 33 fs^2/mm), see also Fig. 14, results in near transform-limited signal pulses with a duration as short as ∼ 18 fs without using any compression.

For the amplification of the generated signal pulses from the first stage, about 1.6 mJ of pump pulse energy is delivered to the second OPA stage. By using a 3:1 Galilean lens telescope in the pump beam path, the pump diameter is expanded to about 8 mm to avoid crystal damage. Also, using an all-reflective 1:3 telescope in the signal beam path, the seed beam diameter is adjusted to about 6 mm. In order to avoid the complications arising from the simultaneous amplification of the signal and idler pulses in the second stage, two dichroic mirrors, DM5 and DM6, which have high reflectivity ($R > 99\%$) for the signal and high transmission ($T > 90\%$) for the idler are used to suppress the idler. The amplified signal pulses in the second stage nearly follow the behavior of the seed pulses from the first stage. Typical spectra of the amplified signal pulses after the second stage are shown in Fig. 47. As can be seen, for signal wavelengths shorter than 1200 nm, where the GVM still determines the gain bandwidth (see Fig. 14), the signal spectra are about 30 nm broad. On the other hand, for wavelengths in the 1200 nm $< \lambda_S <$ 1300 nm range, where the parametric gain bandwidth drastically increases, spectral widths of 80–120 nm are obtained for the signal, which support sub-30 fs transform-limited pulses.

Across the tuning range of 1150 nm $< \lambda_S <$ 1300 nm more than 400 μJ (signal plus idler) of pulse energy is produced in the second stage, corresponding to an internal conversion efficiency of 30% in this stage. In order to compress the signal pulses, we applied the same prism-pair

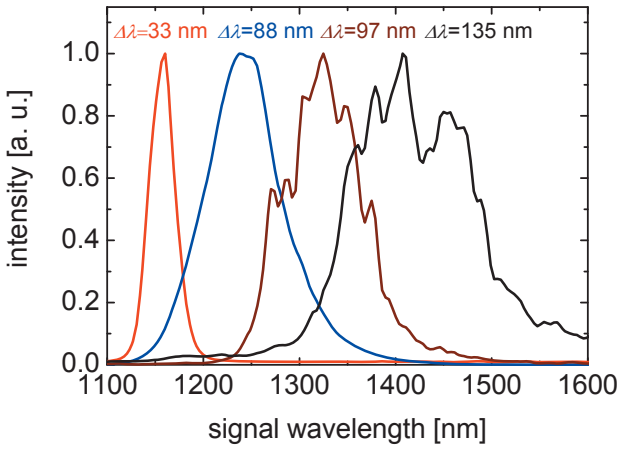

Figure 47 (online color at: www.lpr-journal.org) Typical spectra of the amplified near-IR signal pulses across the tuning range.

compressor from the previous subsection with a separation of 50–70 cm, depending on wavelength. Figs. 48a and b show, respectively, the experimental result and retrieved 128 × 128 points SHG-FROG traces, recorded with a 25-μm thick type-I BBO crystal cut at $\theta = 44°$, for a typical compressed signal pulse near 1300 nm. Figs. 48c and d show the retrieved temporal and spectral intensity and corresponding phase profiles (FROG error 0.009). The retrieved pulse duration of 25 fs (FWHM) corresponds to nearly bandwidth-limited pulses (time-bandwidth product of $\tau\Delta\nu = 0.31$). Note the almost constant phase in time.

Unfortunately, such high-energy signal pulses were obtained only over a limited spectral range near 1300 nm [139]. Tuning towards 1400 nm was accompanied with difficulties related to the suppression of the OPG effect [140] and such tuning extension would probably require the addition of an

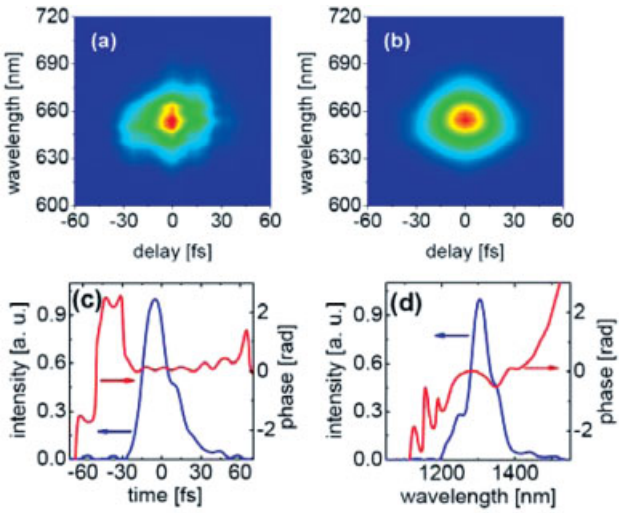

Figure 48 (online color at: www.lpr-journal.org) Typical FROG measurement of the compressed signal pulse: amplitude of measured FROG trace (128 × 128 pixels) (a), retrieved FROG trace in amplitude (b), intensity and phase as a function of time (c), and spectral intensity and phase (d).

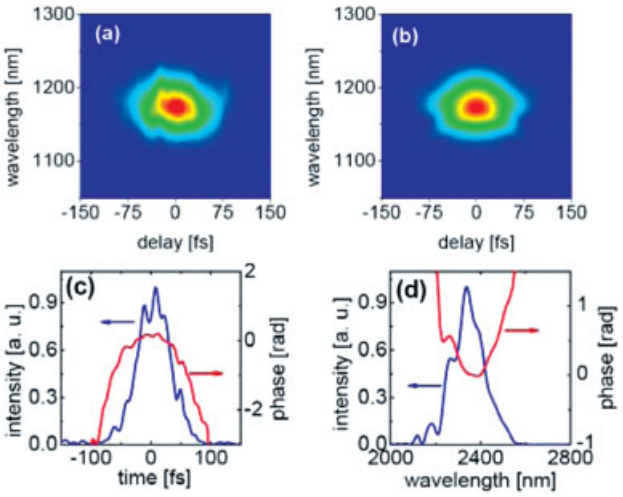

Figure 49 (online color at: www.lpr-journal.org) Typical FROG measurement of the uncompressed idler pulse. (Explanations similar to Fig. 48, only the FROG error is 0.008).

intermediate amplification stage for improved optimization, which would result in increased complexity.

We also measured the idler pulses generated in the second stage in the spectral range characterized by high output energy [140]. A typical SHG FROG measurement at ∼2300 nm is shown in Fig. 49, representing a nearly transform-limited pulse with a duration of 55 fs and a spectral width of 160 nm, with a corresponding time-bandwidth product of $\tau\Delta\nu \sim 0.5$. In principle, the idler pulses are negatively chirped and cannot be further compressed by a conventional prism-pair compressor.

7.4. Ultrabroadband WLC amplification in BIBO

The technique commonly used to obtain ultrabroadband (more than one octave) coherent radiation is based on white-light generation in transparent materials using femtosecond lasers [141]. However, the achievable pulse energies of single filament WLC sources at 1 kHz repetition rate are still very low (typically tens of nanojoules), which limits their applicability. The concept of ultrabroadband coherent amplification (or generation, when starting from parametric superfluorescence) relies on OPA at achromatic phase-matching condition, defined by zero GVM between idler and signal pulses along the direction of the signal wavevector [110]. In the case of collinear type-I interaction, this condition is always fulfilled near degeneracy ($\lambda_S \approx \lambda_I$), but the bandwidth can be further enhanced if the GVD of the signal and idler waves also vanishes [142, 143], as in the case of BIBO, see Sect. 4. For a number of birefringent nonlinear crystals, this ultrabroad gain bandwidth occurs at some specific pump wavelength [143], not necessarily within the operating spectral range of technologically established lasers. For instance, in BBO this situation is realized for a pump wavelength λ_P around 716 nm, see Table 5, far from the 800 nm spectral range in which high-power femtosecond Ti:sapphire-based laser systems at kilohertz repetition rates operate with high stability. As shown recently, similar conditions can also be realized in periodically poled materials such as PPKTP, where the optimum pump wavelength is around 900 nm [144].

Here, we present results of ultrabroadband OPA in ooe type-I BIBO. Since continua generated from 800 nm exhibit strongly decreasing intensity towards 1600 nm, we used the anti-Stokes part of the WLC generated at longer pump wavelengths as seed. The OPA is pumped by a commercial Ti:sapphire amplifier system (SPITFIRE, Spectra-Physics), which provides pulses of 45 fs duration (Gaussian shape assumption) with an energy of up to 2 mJ. For this experiment, a total of 0.7 mJ was utilized, distributed among the OPG used to pump the WLC generator, the pump beam for the BIBO-based OPA, and the probe beam (Fig. 50).

An additional BBO-based OPG (TOPAS, Light Conversion Ltd.) was used as the pump source for the WLC seed. The pulses at the idler wave near 2.1 µm had duration of 50 fs (FWHM). Several microjoules were focused onto a 3-mm thick YAG plate. YAG was chosen because it combines high damage resistivity and nonlinear index of refraction [58]. A variable neutral density filter was used to precisely adjust the pump level in order to obtain stable single filament. After re-collimation, the 2.1-µm beam was blocked using Ho:YAG laser reflecting mirrors, and the WLC was recombined with the pump beam at 800 nm for the BIBO-OPA stage.

The uncoated 3- and 5-mm thick BIBO crystals employed in the OPA were cut at $\theta = 11.4°$ in the x–z plane. The average pump intensity ($\frac{1}{2}$ of the peak on-axis level) at 800 nm was 60 GW/cm^2. After the crystals, the residual pump radiation was blocked by a mirror transmitting the amplified WLC, which was then characterized by an

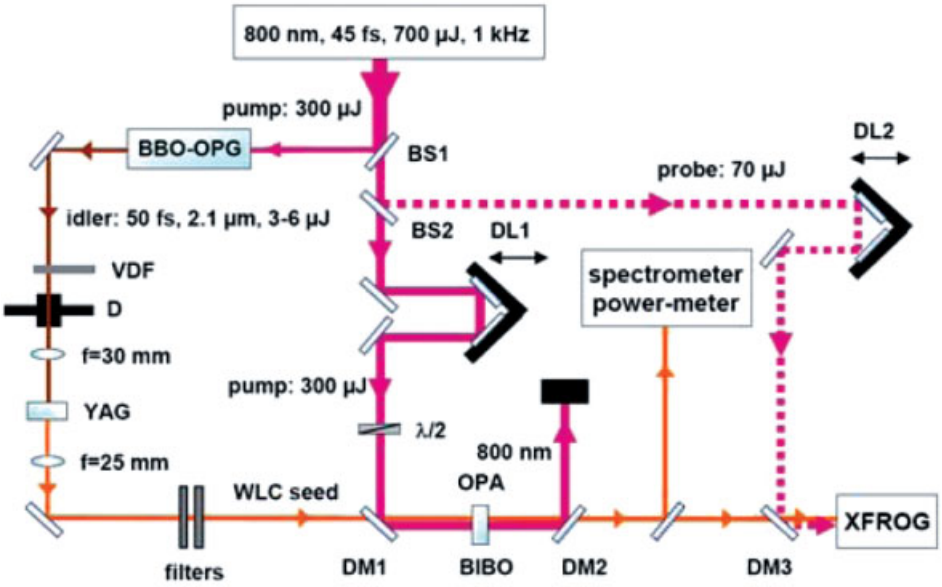

Figure 50 (online color at: www.lpr-journal.org) Schematic of the experimental setup: BS, beam splitters, DL, delay lines, D, diaphragm, VDF, variable density filter, WLC, white-light continuum, DM, dichroic mirrors, filters: Ho:YAG mirrors reflecting the 2.1 µm pump, XFROG: cross-correlation FROG based on SFG.

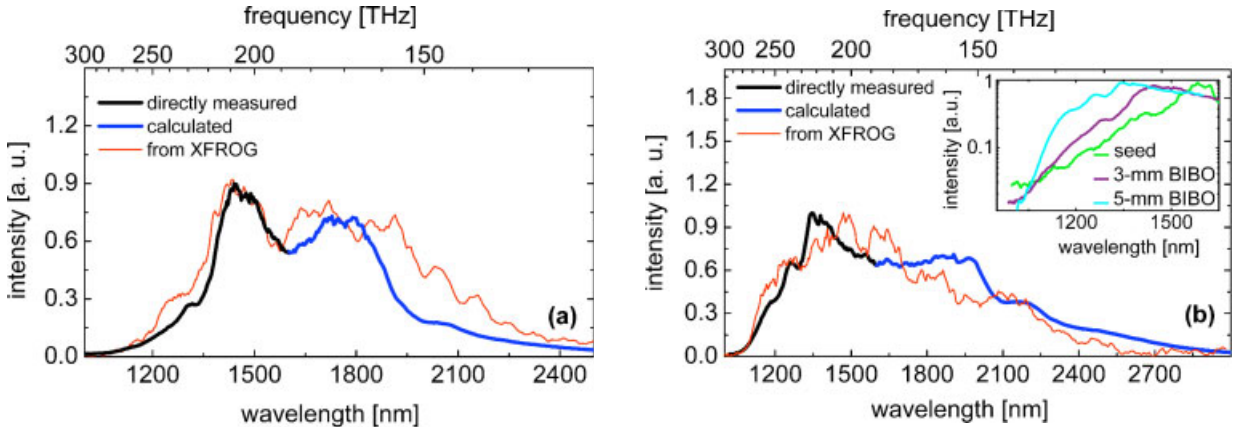

Figure 51 (online color at: www.lpr-journal.org) Spectra of the WLC amplified in 3-mm thick (a) and 5-mm thick (b) BIBO: measured by the InGaAs spectrometer (black curves), reconstructed from the time-integrated XFROG trace (thin red curves) and computed from the Manley-Rowe relation (blue curves). The inset in (b) is a comparison of the spectra of the WLC seed generated in YAG (green line), and the amplified WLC in the 3-mm thick (purple line) and 5-mm thick (cyan line) BIBO crystals.

InGaAs spectrometer and a power meter. Finally, using a fraction of the fresh pump beam as a probe (gate) pulse, XFROG (cross-correlation FROG based on SFG in a 10- µm thick, type-I BBO crystal) measurements of the parametrically generated radiation were performed. The latter were used to reconstruct the entire spectrum and the integral pulse duration for the amplified WLC, as well as to obtain rough information about the phase-modulation. Care was taken to ensure collinear amplification in the BIBO crystals.

Typical energies achieved for the amplified WLC were 30 and 50 µJ for the 3- and 5-mm thick BIBO crystals, respectively. These values were obtained for pump delays that simultaneously provided ultrabroad bandwidths of the amplified WLC. Thus, the maximum intrinsic conversion efficiency was 20% for the 5-mm thick BIBO. The amplified WLC spectra in the case of 3- and 5-mm thick BIBO are shown in Figs. 51a and b, respectively. The partial spectrum up to 1600 nm (thick black curves) was directly recorded by an InGaAs-based spectrometer, while the complete spectrum shown by the red curves was reconstructed from the XFROG trace recorded with a spectrometer and Si-detector array, see Fig. 53. Finally, the thick blue curves in Fig. 51 show the portion of the amplified spectrum (> 1600 nm) which was calculated from that directly measured below 1600 nm, using the Manley-Rowe relation. The obtained amplification bandwidth was ~ 80 THz for the 3-mm thick BIBO, and it increased to ~ 100 THz in the case of the 5-mm thick BIBO.

The FWHM of the cross-correlation functions (Figs. 52a and b) recovered from the XFROG measurement were 84 and 105 fs for the 3- and 5-mm thick BIBO crystals, respectively, and so the corresponding amplified WLC pulse

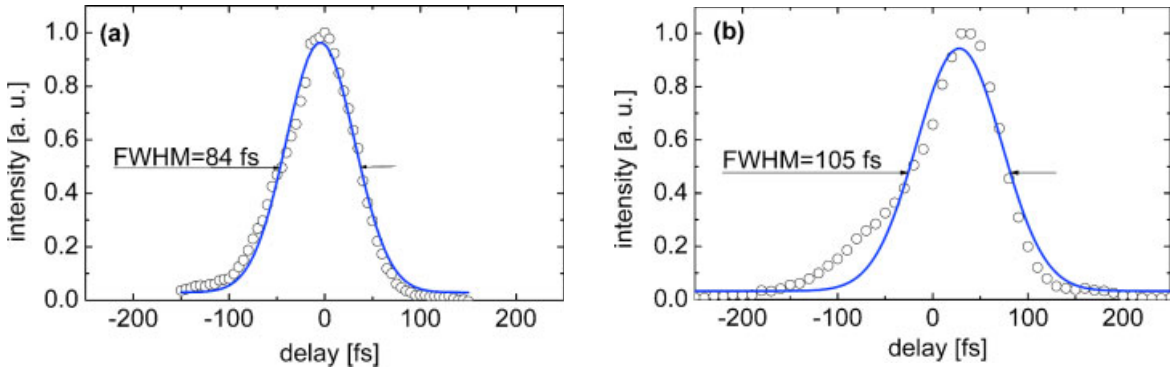

Figure 52 (online color at: www.lpr-journal.org) Cross-correlation functions with Gaussian fits of the amplified WLC in the 3-mm thick (a) and 5-mm thick (b) BIBO. The FWHM indicated corresponds to the Gaussian fits to the cross-correlation traces.

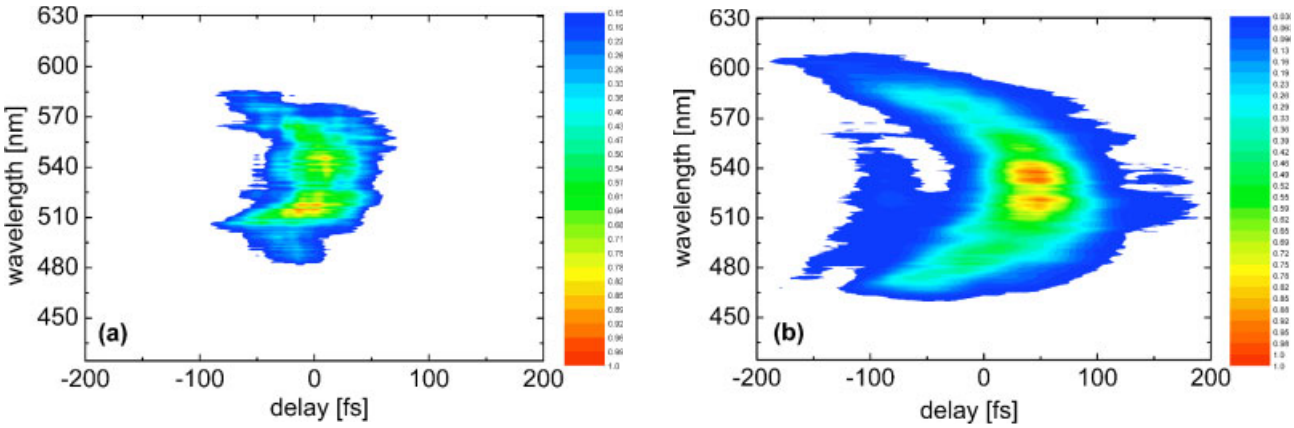

Figure 53 (online color at: www.lpr-journal.org) XFROG traces of the WLC amplified in the 3-mm thick (a) and 5-mm thick (b) BIBO using probe pulses at 800 nm for the SFG.

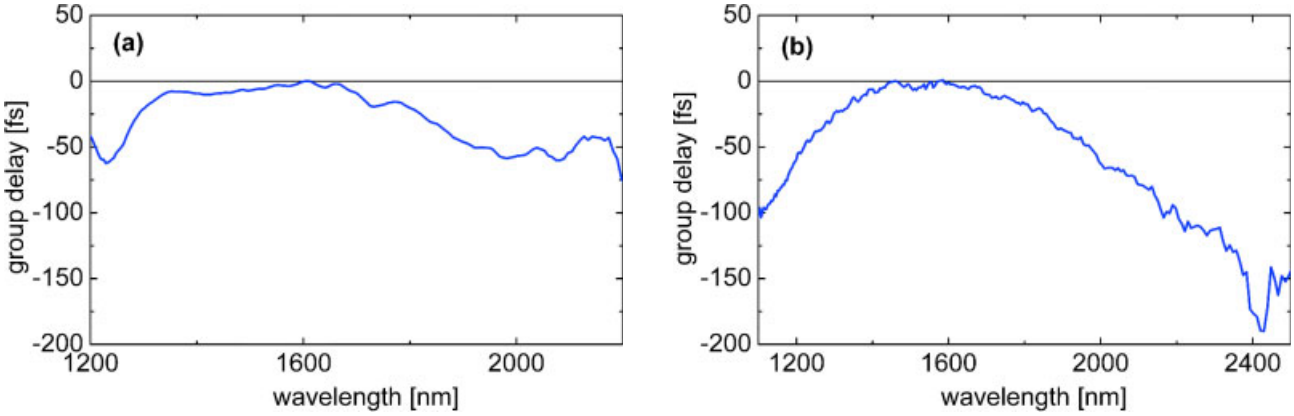

Figure 54 (online color at: www.lpr-journal.org) Evaluation of the group delay versus wavelength for the 3-mm thick (a) and 5-mm thick (b) BIBO calculated from the XFROG traces in Fig. 53 using the center of gravity for each cross-section corresponding to a fixed sum-frequency wavelength.

durations (FWHM intensity) are ~ 70 fs and ~ 95 fs, 1.4 and 1.9 times longer than the pump pulses at 2.1 µm, respectively. A Gaussian pulse shape assumption was used for this rough estimate, the same as for the pump pulses. The time-bandwidth product, thus, amounts to 5.6 and 9.5 for the 3- and 5-mm thick BIBO crystals, respectively.

The simultaneous increase in the spectral width and pulse duration for the thicker BIBO crystal can only be

explained by considering chirp effects. In that case, the increasing temporal walk-off between the pump and amplified pulses results in spectral broadening. The WLC seed level did not allow direct characterization of its temporal and spectral properties. However, from estimates of GVD in all the optical elements used (including the YAG and BIBO crystals), we conclude that the main source of chirp is the BIBO crystal itself. This is not unexpected since this material exhibits the lowest bandgap. Since the zero GVD is near the 1600-nm degeneracy point, the chirp produced by GVD in BIBO has opposite sign for the signal and idler frequencies, as can be seen in Fig. 54. While this satisfies the requirement for energy conservation in the case of OPA pumped by a monochromatic pump it is clear that compensation of such chirp in subsequent pulse compression schemes will not be trivial.

7.5. Ultrabroadband WLC generation in BIBO

The conclusion from the previous subsection concerning the main source of chirp when amplifying WLC in type-I BIBO naturally leads to the question whether the much simpler OPG configuration can be used for direct generation of such broad WLC. To this end, we studied the same two uncoated BIBO crystals of length 3 and 5 mm, using the same pump source with an incident pulse energy of 260 μJ, but without seeding. The same diagnostics and analysis techniques were used as in the case of OPA. Only collinear output was analyzed; in the case of OPG, the noncollinear geometry is undesirable, because different spectral components propagate in different directions.

Most measurements in this subsection were performed with average pump intensities of 100 GW/cm^2 for the 3-mm thick crystal, and 60 GW/cm^2 for the 5-mm thick sample. The WLC energies, measured after blocking the pump beam, were 8 and 12 μJ for the 3- and 5-mm thick BIBO crystals, respectively. It was not possible to further increase the pump intensity in the case of the thicker sample, because higher-order nonlinear effects were observed (non-phase-matched continuum generation). However, with the shorter crystal, it was possible to raise the pump intensity to 150 GW/cm^2 without any detrimental effects. This led to a total output energy of 15 μJ. Taking into account the transmission of the optics and the Fresnel reflections at the crystal faces, this corresponds to an internal conversion efficiency of $\sim 7\%$.

Fig. 55 shows the measured OPG output energy for the 3- and 5-mm thick BIBO crystals, respectively, as a function of the internal angle of the pump beam relative to the normal to the crystal surface. Increasing internal angle corresponds to decreasing phase matching angle, θ, but a direct relation is avoided here because of the inevitable inaccuracy of the crystal cut angle, which could be of the same order as the angular changes studied. As can be expected, at some maximum phase-matching angle, in this case corresponding almost to normal incidence, there is no phase matching and the output energy drops to zero.

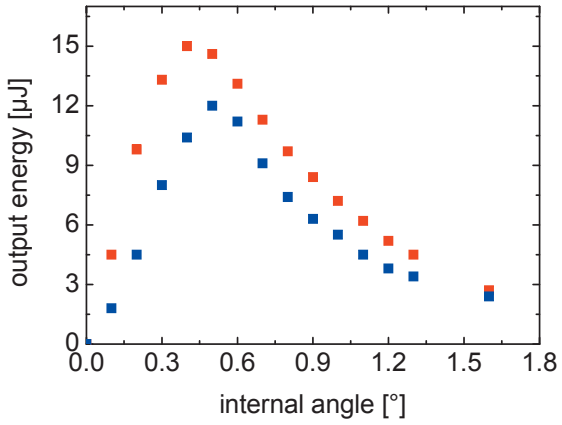

Figure 55 (online color at: www.lpr-journal.org) OPG output energy obtained with the 3-mm thick (red symbols) and 5-mm thick (blue symbols) BIBO crystals versus internal phase-matching angle relative to normal incidence. The average pump intensity (1/2 of the peak on-axis level) is 150 GW/cm^2 and 60 GW/cm^2, respectively.

Figs. 56a and b show the OPG spectra, recorded for the 3- and 5-mm thick BIBO crystals. The dependence of the output spectra on phase-matching angle is in agreement with the theoretical predictions for parametric gain, which were calculated directly from Eq. (5). While the calculations for Fig. 15 and Table 5 were at an exact phase-matching angle or period, here the phase-matching angle was varied for a fixed pump wavelength of $\lambda_P = 800$ nm. In contrast to the analytical approximation used in Fig. 14, where the bandwidth is calculated only for the one wave assuming a single-peaked gain function, from the simulations in Fig. 57 it can be seen that the actual gain bandwidth can be further increased when the spectral gain profiles for the signal and idler waves merge. Note that the phase-matching angle for which this happens is slightly lower than the one corresponding to degeneracy ($\theta \sim 11^\circ$ for $\lambda_P = 800$ nm).

The broadest parametric gain occurs before the two spectra have completely merged. It extends roughly from 1.15 to 2.4 μm. The additional bandwidth enhancement achieved in this way is up to $\sim 50\%$ when compared to the values given in terahertz in Table 5. In fact, the broadest parametric gain (depending on its definition, that is the acceptable dips in the spectral distribution) does not necessarily occur for the magic pump wavelength: Both the pump wavelength and the phase-matching angle can slightly deviate near the values specified in Table 5, to achieve maximum bandwidths [143–145].

With increasing incidence angle in Fig. 56, the spectra undergo broadening, with the widest spectrum at a relative internal angle of $\sim 0.4^\circ$, corresponding to the broadest parametric gain. With further increase in the incidence angle (decrease of the phase-matching angle, θ), the spectra tend to become narrower again, as can be expected for a phase-matching angle deviating from that corresponding to degeneracy. The main qualitative difference in the spectra

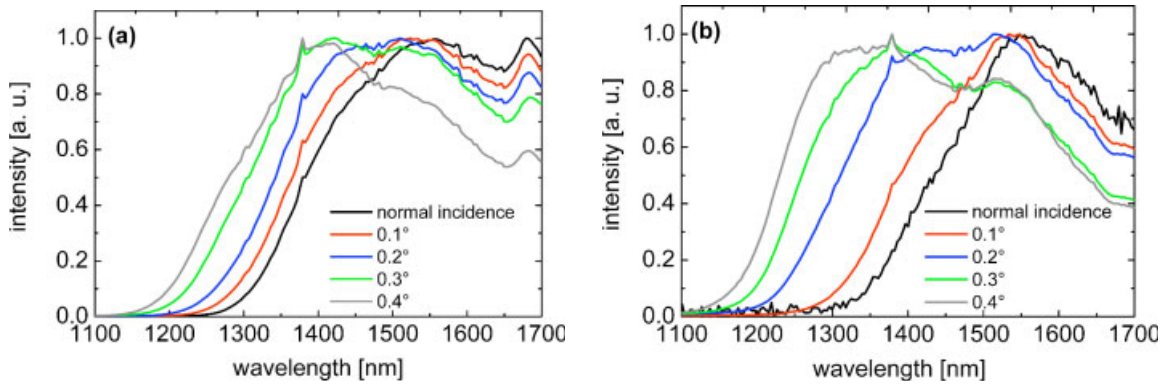

Figure 56 (online color at: www.lpr-journal.org) OPG spectra obtained with the 3-mm thick (a) and 5-mm thick (b) BIBO crystals, recorded with an InGaAs spectrometer at five different internal angles of the pump beam. The pump intensity is 100 GW/cm^2 (a) and 60 GW/cm^2 (b).

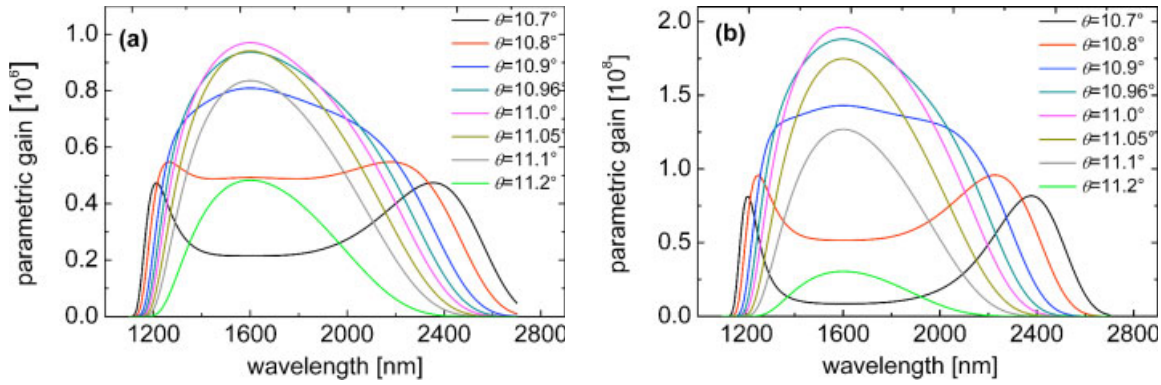

Figure 57 (online color at: www.lpr-journal.org) Parametric gain of BIBO for collinear-type ooe interaction at $\lambda_P = 800$ nm, calculated for several fixed phase-matching angles close to degeneracy ($\theta \approx 11^\circ$). The crystal length, 3 mm (a) and 5 mm (b), and the pump intensity, 100 GW/cm^2 (a) and 60 GW/cm^2 (b), correspond to the experimental conditions in Fig. 56.

obtained with the 3- and 5-mm thick BIBO samples is the decreasing intensity above 1500 nm, observed only for the thicker crystal. For the thinner crystal, the spectral intensity remains almost constant above 1500 nm up to the detection limit of the InGaAs array.

The spectral extent of the WLC is slightly larger for the 5-mm thick BIBO crystal, which can be attributed to the increasing role of the GVM with the pump pulse, leading to chirp formation, as will be seen in the XFROG traces. However, considering the roughly 200 times higher gain in Fig. 57b in comparison to Fig. 57a, it can be concluded that in the spectral range where the spectral gain bandwidth is determined by higher-order dispersion terms, the effect of the gain coefficient, Γ, is rather weak [111, 142]. Figs. 58–60 show the output spectra (a), the XFROG traces (b), and the cross-correlation functions with the gate pulse obtained by integration of the XFROG traces (c) for these three cases. The spectral portions up to 1600 nm shown by the red curves in Figs. 58a–60a, are from direct measurements with the InGaAs spectrometer. The black curves in the same figures show the spectra reconstructed from the XFROG traces, which were recorded with a spectrometer with a Si-detector array. Finally, the portions of the amplified spectra above 1600 nm, shown by blue lines in Figs. 58a–60a, were calculated using the Manley-Rowe relation. In all three cases the correspondence between the two methods used to recover the spectral information is fairly satisfactory. Taking, as a measure, the spectra derived from the XFROG traces, the spectral extension of the generated WLC at the 0-level is roughly 135 THz in all three cases.

The shape of the XFROG traces in Figs. 58b-60b is similar to that obtained in the analogous OPA experiments. In principle, this result confirms our estimates that the phase modulation observed at the OPA output is not caused by the WLC generator or some passive optical elements, but rather by the BIBO crystal itself. The same can be obviously expected in the OPG case. Since the zero GVD point is very close to the point separating the signal and idler branch, opposite chirp is observed in the two branches, see Fig. 61. On the other hand, an opposite sign of the chirp is in any case a condition imposed by the energy conservation law in three-wave interactions, at least under the assump-

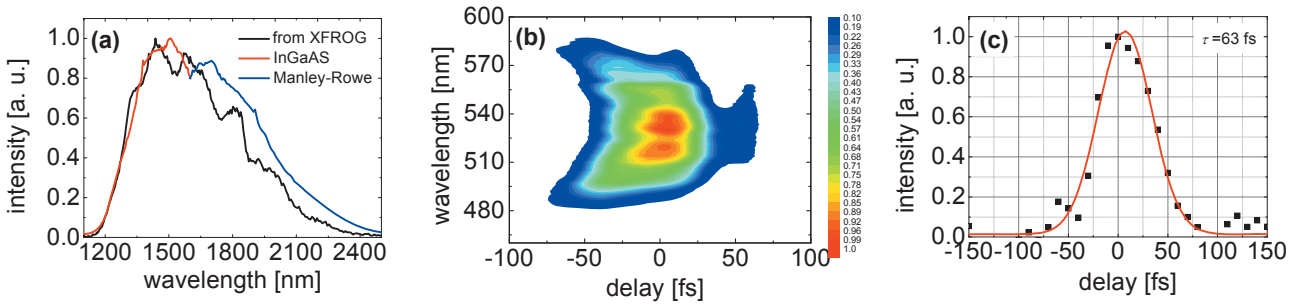

Figure 58 (online color at: www.lpr-journal.org) Spectrum (a), XFROG trace, (b) and cross-correlation function with Gaussian fit, (c) of the OPG output with the 3-mm- thick BIBO crystal; pump intensity: 100 GW/cm^2.

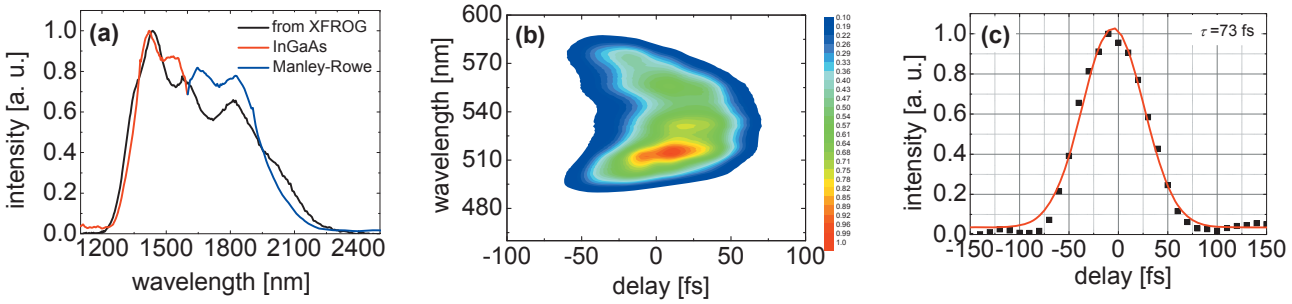

Figure 59 (online color at: www.lpr-journal.org) Spectrum (a), XFROG trace, (b) and cross-correlation function with Gaussian fit, (c) of the OPG output with the 5-mm- thick BIBO crystal; pump intensity: 60 GW/cm^2.

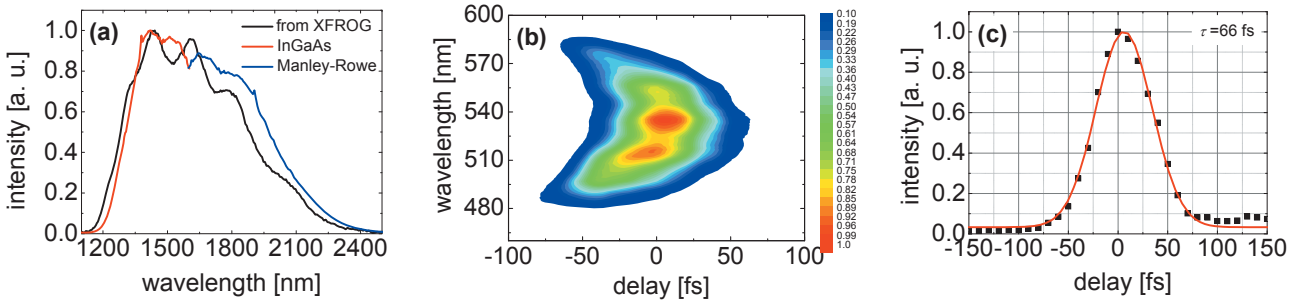

Figure 60 (online color at: www.lpr-journal.org) Spectrum (a), XFROG trace, (b) and cross-correlation function with Gaussian fit, (c) of the OPG output with the 3-mm- thick BIBO crystal; pump intensity: 150 GW/cm^2.

tions stated in Sect. 4. The chirp is more pronounced with increasing parametric gain (conversion efficiency).

As can be seen from Figs. 58c–60c, the integrated cross-correlation functions are well fitted by Gaussian profiles. Since the autocorrelation function of the pump pulses was also analyzed using such a pulse shape, we deconvolved the cross-correlation traces under the same assumption. The resulting integral WLC pulse durations are indicated in the figures as τ (FWHM intensity). The obtained pulse durations are shorter than in the OPA case. The shortest pulse duration, 63 fs, was measured for the 3-mm thick crystal pumped at 100 GW/cm^2. As can be expected, this occurs at the lowest conversion efficiency. The calculated time-bandwidth products are roughly 10 times above the Fourier limit for Gaussian pulse shapes: $\tau\Delta\nu \sim 4.2$ for Fig. 58, ~ 4.7 for Fig. 59, and ~ 5 for Fig. 60.

We performed an additional series of experiments to establish the effect of pump-pulse duration on OPG performance. An analogous pump source at 800 nm, delivering pulses of 100 fs duration, was employed. Typical pump energies incident on the crystals were 300 µJ. At similar pump intensities, the output energy from both the 3- and 5-mm thick BIBO crystals was doubled. In terms of spectral bandwidth, pulse duration, and time-bandwidth products, the

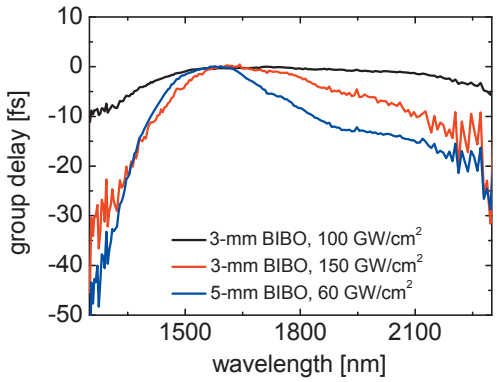

Figure 61 (online color at: www.lpr-journal.org) Group delay derived from the XFROG traces for the three cases depicted in Figs. 58–60.

results were similar to those described above. The integral pulse durations in this case were shorter than the pump pulses and the chirp was not particularly well pronounced.

Finally, in other to obtain a more complete picture of the potentially achievable energy level with this technique, we added a second stage to the BIBO OPG using 3-mm thick crystals in both stages, in a setup very similar to that depicted in Fig. 46. The 1-kHz repetition rate pump system was the same as described in Sects. 7.2 and 7.3, adjusted to 140 fs pulse duration. The first stage was pumped by 170 μJ, but at tighter focusing to achieve OPG operation. Its output was then amplified in the second stage OPA, pumped with about 800 μJ of pump energy. The mirrors of the all-reflective telescope between the two stages, see Fig. 46, were modified to a 3:1 configuration in order to reduce the beam cross-section in the second stage and by using metallic mirrors, both signal and idler were applied for seeding the second stage. The telescope for the pump beam to the second stage was also modified by using lenses of $f = 30$ cm and $f = -5$ cm, in order to similarly reduce its size. XFROG was again used for the characterization of the amplified WLC pulses, applying a 10- μm thick type-I BBO crystal. However, since in this case the pump pulses near 807 nm were longer than the pulse duration of the amplified WLC, we implemented an interference filter in one arm of a SHG autocorrelator to select 80-fs long gate pulses at 1300 nm with a spectral width (FWHM) of about 40 nm for the SFG process. The gate pulses themselves were measured independently by SHG FROG.

A maximum output energy of 115 μJ was obtained from the second stage, thus reaching internal conversion efficiencies close to 17%. In terms of energy, the improvement in comparison to the maximum values obtained with the WLC OPG described previously is almost 8-fold. The obtained integral pulse durations were on the order of 170 fs. The spectral extension of ∼ 100 THz (FWHM), achieved by alignment of the two stages at slightly different angles, leads to a time-bandwidth product of 17, which is 38 times above the Fourier limit for Gaussian pulse shapes. As can

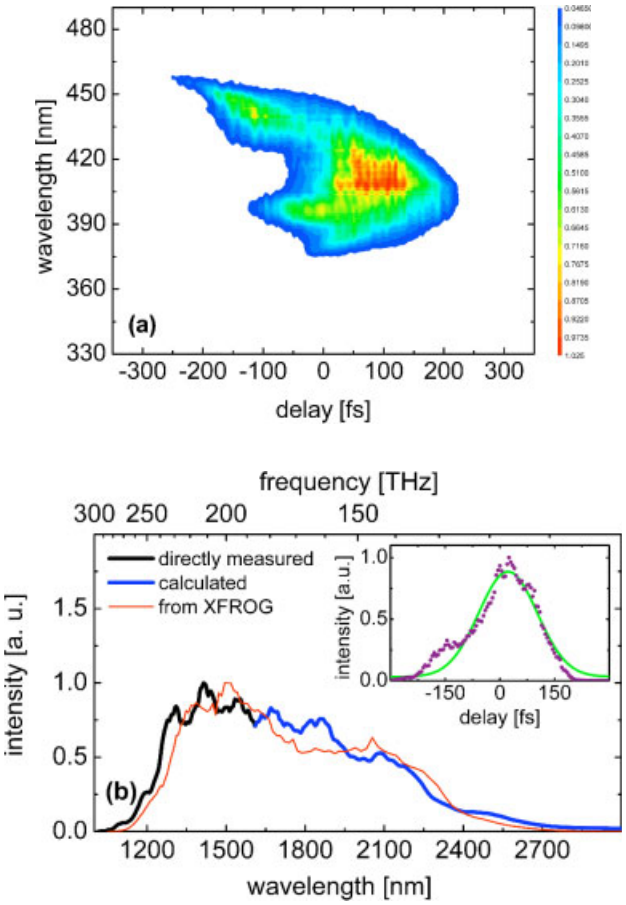

Figure 62 (online color at: www.lpr-journal.org) XFROG trace (a) and spectra (b), with notations similar to Figs. 58–60. The inset in (b) shows the integrated cross-correlation function with Gaussian fit of the ultrabroadband OPG / OPA system.

be seen from the XROG trace in Fig. 62a, negative chirp is observed above 1600 nm, as well as pronounced positive chirp below degeneracy.

We have reconstructed and compared the spectrum of the output pulses using integration over time of the XFROG trace (Fig. 62b, red curve), direct measurement with the InGaAs spectrometer up to 1600 nm (black curve), and calculation of the idler spectrum from conservation of energy – Manley-Rowe relation (blue curve). As can be seen from Fig. 62b there is a good agreement between the different methods. Further steps towards compression of the produced amplified WLC employing a scheme with a deformable mirror for simultaneous compensation of both negative and positive chirp are currently under investigation.

8. Conclusions

In this review paper, we have summarized the properties of BIBO relevant to nonlinear frequency conversion based

on second-order susceptibility of the material, analyzed in detail the phase-matching configurations with special emphasis on the spectral acceptance and parametric gain bandwidth, important parameters for ultrashort (femtosecond) laser pulses, and presented experimental results on efficient generation of femtosecond pulses in different spectral regions (from the UV to the near-IR) and in different energy scales (low power pulses at ∼ 100 MHz repetition rates and high power pulses at a repetition rate of 1 kHz).

We have demonstrated the generation of high-repetition-rate femtosecond pulses with wide tunability across the 375–435 nm in the blue spectral range at average power up to 830 mW with conversion efficiency in excess of 50% using simple single-pass SHG in BIBO with a mode-locked Ti:sapphire fundamental laser at 76 MHz. A conversion efficiency of 23% has been achieved for SHG at 782 nm of a low-power (65 mW average power at the fundamental) femtosecond Er-fiber laser/amplifier operating at 56 MHz, preserving the pulse duration of ∼ 60 fs. Using intracavity SHG of a near-IR PPLN SPOPO, we have achieved average powers as much as 260 mW for 1.51 W of Ti:sapphire pump at 17.2% efficiency with tuning range for the second harmonic across 665–785 nm in the red spectral range. Moreover, convenient wavelength tuning across the full range is achieved simply by varying the SPOPO cavity delay without adjustment of any other parameters such as the PPLN crystal temperature, BIBO phase-match angle, or pump wavelength.

We have reported the generation of widely tunable high-repetition-rate femtosecond pulses across the entire visible range of 480–710 nm by developing a SPOPO based on BIBO, and achieved wavelength extension to 250–355 nm in the UV using intracavity SHG of the visible signal pulses in BBO. Combined with the tunability of the fundamental Ti:sapphire laser, the approach provides an exceptionally versatile and continuously tunable source of high-repetition-rate (76 MHz) femtosecond pulses from the UV to near-IR across 250–3000 nm.

BIBO possesses a unique combination of excellent properties for broadband parametric amplification when pumped near 800 nm in a collinear geometry. In this case, higher-order dispersion terms determine the parametric gain bandwidth, which can be extremely broad. In addition, the group velocity matching with the pump ensures long interaction lengths and high efficiency even for femtosecond pulse durations. Hence, BIBO is a very promising candidate for a wide range of femtosecond down-conversion schemes based on Ti:sapphire laser as the pump source. We realized several such schemes in the high-power regime at a repetition rate of 1 kHz.

We have exploited BIBO in a 800-nm-pumped, femtosecond, two-stage, type-II OPA, and demonstrated efficient and tunable operation at 1 kHz with certain advantages (extension to the 3- µm spectral range) over BBO. The shortest pulses obtained were on the order of 100–110 fs. Using two BIBO crystals (type-II and type-I) in a two-stage femtosecond OPA, we were able to increase the output energy by roughly 5 times in comparison to previous work with BBO at 1 kHz repetition rate. The maximum energy obtained for a signal wavelength of 1200 nm was 1.1 mJ (signal plus idler), and the tunability extended from 1.1 to 2.9 µm. Using a two-stage broadband (type-I – type-I) BIBO OPA with WLC seeding, and pumping with 150-fs pulses near 800 nm at 1 kHz, we generated sub-30 fs signal pulses near 1300 nm after compression, at energies exceeding 200 µJ. The corresponding idler pulses near 2.3 µm had durations of 55 fs without compression and energies exceeding 100 µ J.

We have demonstrated ultrabroadband optical parametric amplification and generation in the near-IR with WLC energy as high as 50 µJ in the case of OPA, and 15 µJ in the case of the simpler OPG scheme. These values correspond to internal conversion efficiency of 20% and 7%, respectively. In all cases, the integral pulse durations achieved are in the sub-100-fs range, and the spectral extension covers an octave. This is the first time such WLC has been generated or amplified by a second-order nonlinear process in the femtosecond time scale.

The unique and versatile nonlinear optical properties of BIBO combined with the frequency conversion methods described in this review provide efficient and widely tunable ultrafast sources across the UV, visible and near-IR, offering the advantages of simplicity, practicality, high average power, high intensity and pulse energy, and convenient operation at room temperature.

Acknowledgements We acknowledge financial support from the German-Bulgarian exchange programme (DAAD grants D/05/11319 and D/07/00333, and Bulgarian Ministry of Science and Education NSF Grants D01-81/2006, D01-619/2007, and D01-1174/2008), from the EU within Laserlab Europe (contract RII3-CT-2003-506350), and partial support from the Spanish Ministry of Education and Science through the Consolider Program (CSD2007-00013). The research leading to these results has received funding from the European Community's Seventh Framework Programme FP7/2007-2011 under grant agreement No. 224042.

Valentin Petrov was born in Plovdiv, Bulgaria, in 1959. He received the M. Sc. degree in nuclear physics from University of Sofia, Bulgaria, in 1983, and the Ph. D. degree in optical physics from the Friedrich-Schiller-University, Jena, Germany, in 1988. He joined the Max-Born-Institute for Nonlinear Optics and Ultrafast Spectroscopy (MBI) in Berlin, Germany, in 1992. His research interests include ultrashort light pulses, laser physics, nonlinear optics, and optical materials. He has coauthored more than 230 papers in scientific journals.

Masood Ghotbi received his Ph. D. degree in physics from Amirkabir University of Technology, Tehran, Iran, in 2006. After a two-year postdoctoral stay at the Institute of Photonics Sciences (ICFO), Barcelona, Spain, he joined the Max-Born-Institute for Nonlinear Optics

and Ultrafast Spectroscopy (MBI), Berlin, Germany in 2007. His research interests include nonlinear optics, laser physics and ultrashort pulses. His current research program is focused on the generation of high-energy, ultrashort pulses in the near-IR and also VUV spectral ranges.

Omid Kokabee was born in Gonbadekavoos, Iran, in 1982. He received the B. Sc. degree in Applied Physics from Sharif University of Technology in Tehran, Iran, in 2005. He is currently pursuing the Ph. D. degree in Photonics at Institute of Photonic Sciences (ICFO) in Barcelona, Spain. His research is mainly focused on Ultrashort Nonlinear Optics and High-Power lasers.

Adolfo Esteban Martin was born in Madrid, Spain, in 1978. He received his B. Sc., M. Sc. in photonics, and Ph. D. degree in physics from the Universitat de València (UV), Valencia, Spain, in 2001, 2003, and 2006, respectively. His Ph. D. research was on experimental generation and characterization of spatial patterns in nonlinear resonators. Since 2007, he has been a Juan de la Cierva (JdC) postdoctoral researcher in the Optical Parametric Oscillators group at Institute of Photonic Sciences (ICFO) in Barcelona, Spain. Currently, his work is focused on novel ultrafast optical sources for the visible and infrared.

Frank Noack was born in Jena, Germany, in 1958. He received the Diploma and Ph. D. degree in physics from the Friedrich-Schiller-University, Jena, in 1983 and 1989. Since 1992 he has worked at the Max-Born-Institute for Nonlinear Optics and Short Pulse Spectroscopy in Berlin-Adlershof. His current research interests are generation and amplification of ultrashort light pulses in a broad spectral range and techniques for measurement and control of pulse parameters.

Alexander Gaydardzhiev was born in Gabrovo, Bulgaria, in 1982. He received the M. Sc. degree in physics from Sofia University, Bulgaria and is currently pursuing his Ph. D. degree in laser physics at the same university. His doctoral work is focused on white-light generation and amplification through parametric processes in the near-infrared spectral region. His research interests include nonlinear optics, femtosecond science and solid-state laser development.

Ivaylo Nikolov was born in Yambol, Bulgaria in 1977. He received the M. Sc. degree in Physics in 1999 and Ph. D. degree in laser physics in 2006 from Sofia University. His research interests include laser physics, solid-state lasers, ultrashort pulses and nonlinear optics.

Pancho Tzankov was born in Sofia, Bulgaria, in 1974. He received a M. Sc. degree in laser physics and technology from Sofia University, Bulgaria, in 1997, and a Ph. D. degree in physical chemistry from the Technical University of Munich, Germany, in 2003. After a three-year postdoctoral stay at the Max-Born-Institute for Nonlinear Optics and Ultrafast Spectroscopy, Berlin, Germany, in 2006 he joined Quantronix Corporation, East Setauket, New York, USA, where he is currently a research and development manager for nonlinear optics. His research interests include nonlinear optics, laser physics, and their applications.

Ivan Buchvarov was born in Pavel Banya, Bulgaria, in 1960. He received the M. Sc. degree in applied physics and the Ph. D. degree in physics from Sofia University, Bulgaria, in 1984 and 1994, respectively. He is currently associate professor in Sofia University. His research interests include ultrashort laser pulse generation, ultrafast phenomena in molecular systems and nonlinear optics. Since 1996 he has been the project leader of 13 research and development projects with both American and European partners in industry as well as in academia.

Kentaro Miyata was born in Hokkaido, Japan, in 1982. He received the M. Sc. degree in Physics from Chitose Institute of Science and Technology (CIST), Hokkaido, Japan, in 2007. He is currently working toward the Ph. D. degree at CIST, focusing on third-order nonlinear frequency conversions in inorganic crystals.

Andrzej Majchrowski was born in 1952 in Warsaw, Poland. He received his M. Sc. degree in chemistry from Warsaw Technical University in 1976, and the Ph. D. degree in materials engineering in 1989 from Military University of Technology (MUT) in Warsaw. He is the head of the crystal growth laboratory at Institute of Applied Physics, MUT. He researches single crystal growth of oxide materials, such as borates, niobates, tungstates, sillenites, and phosphates as opto-electronic materials. He is a coauthor of over 100 papers published in scientific journals.

Ivan Kityk was born in Lviv, Ukraine in 1957. He received the M. Sc. degree in solid-state spectroscopy from Lviv University, Ukraine, in 1979. He worked from 1994 to 2008 in the Institute of Physics, J. Dlugosz University, in Czestochowa (Poland). Since 2008 he has been a professor in the Physical Chemistry Department of Silesian Technological University (Poland). His research interests include design and exploration of novel nonlinear optical materials, including inorganic and organic compounds. He has coauthored more than 280 papers in scientific journals.

Fabian Rotermund was born in Seoul, Korea, in 1967. He received the diploma degree in Physics from the University of Regensburg, Germany, in 1997, and the Ph. D. degree in Physics from the Technical University of Berlin, Germany, in 2000. Currently, he is an associate professor in the Physics Department and Division of Energy Systems Research at Ajou University, Suwon, Korea. His research interests include ultrafast lasers and amplifiers, nonlinear optics, and nanophotonics.

Edward Michalski was born in Mosciska, Poland, in 1951. He received the Ph. D. degree in materials science from Military University of Technology (MUT), Warsaw, Poland in 1981. Currently he is a Professor of Materials Science at MUT, where he lectures physics, crystallography and physical properties related to the crystal structure. He is a member of the Committee of Crystallography, Polish Academy of Sciences. His research interests include X-ray diffraction of different materials (single crystals, powders, epitaxial films, liquid crystals), especially theory and measurements of X-ray diffuse scattering from polytype crystals with stacking faults and X-ray orientation of single crystals for special cuts.

Majid Ebrahim-Zadeh is an Institucio Catalana de Recerca i Estudis Avancats (ICREA) Professor at the Institute of Photonic Sciences (ICFO), Barcelona, Spain. He has been active in experimental nonlinear optics for over 20 years and he has made major contributions to the advancement of frequency-conversion sources and optical parametric oscillators (OPOs) from the continuous-wave to femtosecond time-scales. He has published over 300 technical papers, including 12 major book chapters and reviews, has coedited 2 books, and has presented over 50 invited papers at major international conferences. He has served as chair and member of technical program committees of various conferences, on the Joint Council on Quantum Electronics, International Council on Quantum Electronics, the Steering Committee of the Conference of Lasers and Electro-Optics (USA), and as advisory editor and topical editor of *Optics Letters*. He is a Fellow of the Optical Society of America.

References

[1] H. Hellwig, J. Liebertz, and L. Bohaty, Linear optical properties of the monoclinic bismuth borate BiB_3O_6, J. Appl. Phys. **88**, 240–244 (2000).
[2] Z.-P. Wang, B. Teng, C.-L. Du, X.-G. Xu, K. Fu, G.-B. Xu, J.-Y. Wang, and Z.-S. Shao, Frequency doubling property of the low symmetric nonlinear optical crystal BIBO, Acta Phys. Sin. **52**, 2176–2184 (2003).
[3] C. Du, Z. Wang, J. Liu, X. Xu, B. Teng, K. Fu, J. Wang, Y. Liu, and Z. Shao, Efficient intracavity second-harmonic generation at 1.06 µm in a BiB_3O_6 (BIBO) crystal, Appl. Phys. B **73**, 215–217 (2001).
[4] Z. Wang, C. Du, B. Teng, X. Xu, K. Fu, G. Xu, J. Wan, Z. Shao, and X. Yang, Diode-laser-array end-pumped 1 W CW Nd:YVO_4/BIBO green laser, J. Mod. Opt. **50**, 1253–1258 (2003).
[5] Z. Zhang, H. M. Tan, L. L. Gao, B. S. Wang, J. G. Miao, and J. Y. Peng, Intra-cavity second harmonic generation with Nd:YVO_4/BIBO laser at 542 nm, Opt. Commun. **267**, 487–490 (2006).
[6] C. Czeranowsky, E. Heumann, and G. Huber, All-solid-state continuous-wave frequency-doubled Nd:YAG – BiBO laser with 2.8-W output power at 473 nm, Opt. Lett. **28**, 432–434 (2003).
[7] S. Dong, J. Wang, Z. Wang, J. Zhang, B. Teng, Z. Shao, X. Lin, R. Li, and Z. Xu, Growth of large size and high quality bismuth triborate crystal and its frequency conversions, J. Chin. Ceram. Soc. **31**, 836–841 (2003).
[8] Q. Zheng and L. Zhao, Efficient blue laser generation at 473 nm by a BIBO crystal, Opt. Laser Technol. **36**, 449–451 (2004).
[9] F. Li, Y. Sun, and K. Zhang, LD end-pumped Nd:YAG/BIBO TEM_{00} mode blue laser, Acta Sin. Quantum Opt. **12**, 231–233 (2006).
[10] Q. Zheng, L. Zhao, and S. Dong, High efficient blue laser generation at 473 nm by BIBO crystal, Chin. J. Laser **31**, 1031–1032 (2004).
[11] F. Jia, Q. Xue, Q. Zheng, Y. Bu, and L. Qian, 2.41 W compact efficient CW blue light generation by intra-cavity frequency doubling of a compact Nd:YAG laser, Opt. Laser Technol. 39, 1081–1083 (2007).
[12] Y. Lü, X. Zhang, Z. Yao, and F. Zhang, 6.2-W deep blue light generation by intracavity frequency-doubled Nd:$GdVO_4$ using BIBO, Chin. Opt. Lett. **5**, 407–408 (2007).
[13] J. Gao, X. Yu, X. D. Li, F. Chen, K. Zhang, R. P. Yan, J. H. Yu, and Y. Z. Wang, 456-nm deep-blue laser generation by intracavity frequency doubling of Nd:$GdVO_4$ under 879-nm diode pumping, Laser Phys. **19**, 111–114 (2009).
[14] J. Gao, X. Yu, F. Chen, X. Li, R. Yan, K. Zhang, J. Yu, and Y. Wang, 12.0-W continuous-wave diode-end-pumped Nd:$GdVO_4$ laser with high brightness operating at 912-nm, Opt. Express **17**, 3574–3580 (2009).
[15] C. Du, S. Ruan, Y. Yu, and Z. Wang, High-power intracavity second-harmonic generation of 1.34 µm in BiB_3O_6 crystal, Opt. Express **13**, 8591–8595 (2005).
[16] R. Sarrouf, T. Badr, and J. J. Zondy, Intracavity second-harmonic generation of diode-pumped continuous-wave, single frequency 1.3 µm Nd:$YLiF_4$ lasers, J. Opt. A, Pure Appl. Opt. **10**, 104011-1–10 (2008).
[17] L. S. Cruz and F. C. Cruz, External power-enhancement cavity versus intracavity frequency doubling of Ti:sapphire lasers using BIBO, Opt. Express **15**, 11913–11921 (2007).
[18] M. Thorhauge, J. L. Mortensen, P. Tidemand-Lichtenberg, and P. Buchhave, Tunable intra-cavity SHG of CW Ti:sapphire lasers around 785 nm and 810 nm in BiBO-crystals, Opt. Express **14**, 2283–2288 (2006).
[19] M. Thorhauge, J. L. Mortensen, P. Tidemand-Lichtenberg, P. Buchhave, and J. R. Rasmussen, 100 mW of blue light at 405 nm from intracavity doubling of CW Ti:sapphire laser utilising BIBO-crystal, Proc. SPIE **6190**, 61900F-1–11 (2006).

[20] C. Petridis, M. Ghotbi, A. Scaria, G. R. Fayaz, and M. Ebrahim-Zadeh, Tunable, All-Solid-State, Continuous-Wave Source for the Blue using BiB_3O_6, Conference on Lasers and Electro-Optics CLEO'05, Baltimore (MD), USA, 2005, paper JTuC21, in: CLEO/QELS Tech. Digest CD-ROM.
[21] R. Hartke, E. Neumann, G. Huber, M. Kühnelt, and U. Steegmüller, Efficient green generation by intracavity frequency doubling of an optically pumped semiconductor disk laser, Appl. Phys. B **87**, 95–99 (2007).
[22] A. Petersen and R. Lane, Second harmonic operation of diode-pumped Rb vapor lasers, Proc. SPIE **7005**, 700529-1–5 (2008).
[23] A. B. Petersen and R. J. Lane, A diode-pumped Rb laser at 398 nm, Proc. SPIE **6871**, 68711Q-1–5 (2008).
[24] G. K. Samanta and M. Ebrahim-Zadeh, Continuous-wave, single-frequency, solid-state blue source for the 425–489 nm spectral range, Opt. Lett. **33**, 1228–1230 (2008).
[25] Z. Chen, B. Lu, Z. Xu, W. Zhuang, C. Yu, D. Yu, K. Huang, X. Chen, and J. Chen, Second harmonic 423-nm laser generated by BIBO crystal for calcium optical frequency standard, Chin. Opt. Lett. **6**, 317–319 (2008).
[26] T. Schmitt, A. Deninger, F. Lison, and W. Kaenders, Recent advances in non-linear frequency conversion of high-power, single-mode diode lasers, Proc. SPIE **5707**, 16–22 (2005).
[27] V. Ruseva and J. Hald, Generation of UV light by frequency doubling in BIBO, Opt. Commun. **236**, 219–223 (2004).
[28] S. Kobtsev and V. Lunin, Resonant doubler with a 2-THz automatic quasi-smooth scan range for widely tunable CW single-frequency lasers, Proc. SPIE **6455**, 645517-1–8 (2007).
[29] S. Kobtsev and A. Zavyalov, Efficient second-harmonic generation of CW radiation in an external optical cavity using non-linear crystal BIBO, Proc. SPIE **6610**, 66100P-1–5 (2008).
[30] S. Maeda, Y. Tabata, H. Kumagai, and A. Kobayashi, Single-frequency 389-nm CW coherent light source for optical pumping of metastable ^{3}He atoms, Proc. SPIE **6875**, 68751B-1–8 (2008).
[31] X. H. Fu, H. H. Tan, Y. M. Li, E. J. Hao, G. Shen, and L. S. Qian, Efficient generation of a CW 593.5-nm laser by intracavity sum-frequency mixing with a BiB_3O_6 (BIBO) crystal, Laser Phys. **17**, 1345–1348 (2007).
[32] T. Liu, H. Tan, and L. Gao, Intracavity sum-frequency mixing with BIBO in 593 nm laser, Acta Photon. Sin. **36**, 1195–1197 (2007).
[33] E. Herault, F. Balembois, P. Georges, and T. Georges, 1064 nm Nd:YVO_4 laser intracavity pumped at 912 nm and sum-frequency mixing for an emission at 491 nm, Opt. Lett. **33**, 1632–1634 (2008).
[34] S. Zou, P. Li, L. Wang, M. Chen, and G. Li, 980 nm Yb-doped single-mode fiber laser and its frequency-doubling with BIBO, Appl. Phys. B **95**, 685–690 (2009).
[35] C. Du, B. Teng, Z. Wang, J. Liu, X. Xu, G. Xu, K. Fu, J. Wang, Y. Liu, and Z. Shao, Actively Q-switched intracavity second-harmonic generation at 1.06 μm in BiB_3O_6 crystal, Opt. Laser Technol. **34**, 343–346 (2002).
[36] M. Peltz, J. Bartschke, A. Borsutzky, R. Wallenstein, S. Vernay, T. Salva, and D. Rytz, Harmonic generation in bismuth triborate (BiB_3O_6), Appl. Phys. B **81**, 487–495 (2005).
[37] S. Johansson, S. Bjurshagen, C. Canalias, V. Pasiskevicius, F. Laurell, and R. Koch, An all solid-state UV source based on a frequency quadrupled, passively Q-switched 946 nm laser, Opt. Express **15**, 449–458 (2007).
[38] O. Kimmelma, I. Tittonen, and S. C. Buchter, Short pulse, diode pumped, passively Q-switched Nd:YAG laser at 946 nm quadrupled for UV production, J. Europ. Opt. Soc., Rapid Publ. **3**, 08008–1-5 (2008).
[39] B. Jungbluth, M. Vierkoetter, M. Hoefer, J. Loehring, D. Oberbeckmann, and D. Hoffmann, Design and characterization of a rugged and compact setup for widely tunable harmonic generation in the ultraviolet, Proc. SPIE **6455**, 645502-1–10 (2007).
[40] Y. Bi, H.-B. Zhang, Z.-P. Sun, Z.-R.-G.-T. Bao, H.-Q. Li, Y.-P. Kong, X.-C. Lin, G.-L. Wang, J. Zhang, W. Hou, R.-N. Li, D.-F. Cui, Z.-Y. Xu, L.-W. Song, P. Zhang, J.-F. Cui, and Z.-W. Fan, High-power blue light generation by external frequency doubling of an optical parametric oscillator, Chin. Phys. Lett. **20**, 1957–1959 (2003).
[41] X. C. Lin, H. B. Zhang, H. Q. Li, Y. P. Kong, Y. Bi, Z. P. Sun, and Z. Y. Xu, Continuous tuning high power blue light by frequency doubling in BiB_3O_6 crystals, Proc. SPIE **6028**, 60280C-1–6 (2005).
[42] O. Kimmelma and I. Tittonen, Passively Q-switched Nd:YAG pumped UV lasers at 280 and 374 nm, Opt. Commun. (2009), doi:10.1016/j.optcom.2009.04.004.
[43] M. Peltz, J. Bartschke, A. Borsutzky, R. Wallenstein, S. Vernay, T. Salva, and D. Rytz, Bismuth triborate (BiB_3O_6) optical parametric oscillators, Appl. Phys. B **80**, 55–60 (2005).
[44] B. Teng, S. Dong, Y. Ding, Z. Wang, J. Wang, R. Mao, Z. Zhai, Z. Yu, X. Sun, and P. Ma, BiB_3O_6 nanosecond optical parametric oscillator, Acta Opt. Sin. **28**, 1998–2001 (2008).
[45] K. Kato, Parametric oscillation in BiB_3O_6 pumped at 1.0642 μm, Proc. SPIE **6455**, 645512-1–5 (2007).
[46] Z. Wang, B. Teng, K. Fu, X. Xu, R. Song, C. Du, H. Jiang, J. Wang, Y. Liu, and Z. Shao, Efficient second harmonic generation of pulsed laser radiation in BiB_3O_6 (BIBO) crystal with different phase matching directions, Opt. Commun. **202**, 217–220 (2002).
[47] B. Teng, J. Wang, Z. Wang, H. Jiang, X. Hu, R. Song, H. Liu, Y. Liu, J. Wei, and Z. Shao, Growth and investigation of a new nonlinear optical crystal: bismuth borate BiB_3O_6, J. Cryst. Growth **224**, 280–283 (2001).
[48] B. Teng, J. Wang, Z. Wang, H. Jiang, R. Song, H. Liu, X. Hu, Y. Liu, J. Wei, and Z. Shao, Research on crystal growth and properties of a new nonlinear optical crystal: Bismuth borate BiB_3O_6, Chin. Sci. Bull **46**, 1783–1785 (2001).
[49] B. Teng, J. Wang, Z. Wang, H. Jiang, H. Liu, X. Hu, S. Dong, Y. Liu, and Z. Shao, Crystal growth, structure and properties of bismuth triborate BiB_3O_6 crystal, Sci. China E **45**, 19–26 (2002).
[50] B. Teng, J. Wang, Z. Wang, X. Hu, H. Jiang, H. Liu, X. Cheng, S. Dong, Y. Liu, and Z. Shao, Crystal growth, thermal and optical performance of BiB_3O_6, J. Cryst. Growth **233**, 282–286 (2001); Corrigendum: **240**, 331 (2002).
[51] M. Ghotbi, Z. Sun, A. Majchrowski, E. Michalski, I. V. Kityk, and M. Ebrahim-Zadeh, Efficient third harmonic gener-

ation of microjoule picosecond pulses at 355 nm in BiB_3O_6, Appl. Phys. Lett. **89**, 173124-1–3 (2006).
[52] Z. Wang, C. Du, B. Teng, X. Xu, G. Xu, K. Fu, J. Wang, and Z. Shao, Third harmonic generation property of 1064 nm in nonlinear optical crystal BiB_3O_6 of low symmetry, Acta Opt. Sin. **23**, 1300–1305 (2003).
[53] Z. Sun, M. Ghotbi, and M. Ebrahim-Zadeh, Widely tunable picosecond optical parametric generation and amplification in BiB_3O_6, Opt. Express **15**, 4139–4148 (2007).
[54] M. Ghotbi and M. Ebrahim-Zadeh, 990 mW average power, 52% efficient, high-repetition-rate picosecond-pulse generation in the blue with BiB_3O_6, Opt. Lett. **30**, 3395–3397 (2005).
[55] M. Ebrahim-Zadeh, Ultrafast frequency-conversion sources for the visible and ultraviolet based on BiB_3O_6, Proc. SPIE **6451**, 645106-1–16 (2007).
[56] V. Petrov, M. Ghotbi, P. Tzankov, F. Noack, I. Nikolov, I. Buchvarov, and M. Ebrahim-Zadeh, Optical parametric generation of high-energy femtosecond pulses in the 1–3 µm spectral range using BiB_3O_6, Proc. SPIE **6455**, 64550C-1–12 (2007).
[57] M. Ebrahim-Zadeh, Efficient ultrafast frequency-conversion sources for the visible and ultraviolet based on BiB_3O_6, IEEE J. Sel. Top. Quantum Electron. **13**, 679–691 (2007).
[58] V. Petrov, A. Gaydardzhiev, I. Nikolov, I. Buchvarov, P. Tzankov, and F. Noack, The application of the monoclinic BiB_3O_6 nonlinear crystal in ultrafast laser technology, Proc. SPIE **6875**, 68750X-1–15 (2008).
[59] C. Xiong and W. J. Wadsworth, Polarized supercontinuum in birefringent photonic crystal fibre pumped at 1064 nm and application to tuneable visible/UV generation, Opt. Express **16**, 2438–2445 (2008).
[60] E. Herault, M. Lelek, F. Balembois, and P. Georges, Pulsed blue laser at 491 nm by nonlinear cavity dumping, Opt. Express **16**, 19419–19426 (2008).
[61] J. Peng, J. Miao, Y. Wang, B. Wang, H. Tan, L. Qian, and X. Ma, Passive stabilization of a passively mode-locked Nd:$GdVO_4$ laser by inverse saturable absorption, Opt. Commun. **281**, 141–145 (2008).
[62] K. Miyata, T. Mikami, N. Umemura, and K. Kato, Direct third-harmonic generation in BiB_3O_6, Proc. SPIE **6875**, 687518-1–5 (2008).
[63] K. Miyata, N. Umemura, and K. Kato, Phase-matched pure $\chi^{(3)}$ third-harmonic generation in noncentrosymmetric BiB_3O_6, Opt. Lett. **34**, 500–502 (2009).
[64] J. Rothhardt, S. Hädrich, J. Limpert, and A. Tünnermann, 80 kHz repetition rate high power fiber amplifier flat-top pulse pumped OPCPA based on BIB_3O_6, Opt. Express **17**, 2508–2517 (2009).
[65] R. Fröhlich, L. Bohaty, and J. Liebertz, Die Kristallstruktur von Wismutborat, BiB_3O_6, Acta Crystallogr. C, Cryst. Struct. Commun. **40**, 343–344 (1984).
[66] Z. Lin, Z. Wang, C. Chen, and M.-H. Lee, Mechanism for linear and nonlinear optical effects in monoclinic bismuth borate (BiB_3O_6) crystal, J. Appl. Phys. **90**, 5585–5590 (2001).
[67] D. A. Roberts, Simplified characterization of uniaxial and biaxial nonlinear optical crystals: A plea for standardization of nomenclature and conventions, IEEE J. Quantum Electron. **28**, 2057–2074 (1992).
[68] H. Hellwig, J. Liebertz, and L. Bohaty, Exceptional large nonlinear optical coefficients in the monoclinic bismuth borate BiB_3O_6 (BIBO), Solid State Commun. **109**, 249–251 (1999).
[69] V. G. Dmitriev, G. G. Gurzadyan, and D. N. Nikogosyan, Handbook of Nonlinear Optical Crystals, Third Revised Edition (Springer, Berlin, 1999).
[70] M. Ghotbi and M. Ebrahim-Zadeh, Optical second harmonic generation properties of BiB_3O_6, Opt. Express **12**, 6002–6019 (2004).
[71] N. Umemura, K. Miyata, and K. Kato, New data on the optical properties of BiB_3O_6, Opt. Mater. **30**, 532–534 (2007).
[72] N. Umemura, S. Banerjee, K. Miyata, F. Tanno, and K. Kato, Thermo-Optic Dispersion Formula for BiB_3O_6, Conference on Lasers and Electro-Optics CLEO'05, Baltimore (MD), USA, 2005, paper JTuC18, in: CLEO/QELS Tech. Digest CD-ROM.
[73] P. Tzankov and V. Petrov, Effective second-order nonlinearity in acentric crystals with low symmetry, Appl. Opt. **44**, 6971–6985 (2005).
[74] J. Kroupa, D. Kasprowicz, A. Majchrowski, E. Michalski, and M. Drozdowski, Optical properties of bismuth triborate (BIBO) single crystals, Ferroelectrics **318**, 77-82 (2005).
[75] D. Xue, K. Betzler, H. Hesse, and D. Lammers, Origin of the large nonlinear coefficients in bismuth borate BiB_3O_6, phys. stat. sol. (a) **176**, R1–R2 (1999).
[76] D. Xue, K. Betzler, and H. Hesse, Calculation of second-order nonlinear optical behaviors of a new borate crystal: BiB_3O_6, Chem. Res. **11**(2), 1–4 (2000).
[77] D. Xue, K. Betzler, H. Hesse, and D. Lammers, Nonlinear optical properties of borate crystals, Solid State Commun. **114**, 21–25 (2000).
[78] A. H. Reshak, S. Auluck, and I. V. Kityk, Experimental and theoretical investigations of the first and second order optical susceptibilities of BiB_3O_6 single crystal, Appl. Phys. A **91**, 451–457 (2008).
[79] R. Ochrombel, Temperaturabhängige optische, elektrooptische und piezoelektrische Untersuchungen ausgewählter azentrischer Kristalle, Ph. D. Dissertation, The Faculty of Mathematics and Natural Sciences, University of Cologne, Germany (2007).
[80] L. Huang, G. Zhang, C. Huang, Y. Wei, and M. Wei, The principal refractive indices and thermal coefficients of BiB_3O_6 crystal, Acta Photon. Sin. **35**, 1005–1007 (2006).
[81] P. Becker, J. Liebertz, and L. Bohaty, Top-seeded growth of bismuth triborate, BiB_3O_6, J. Cryst. Growth **203**, 149–155 (1999).
[82] M. Ghotbi, M. Ebrahim-Zadeh, V. Petrov, P. Tzankov, and F. Noack, Efficient 1 kHz optical parametric amplification in BiB_3O_6 pumped at 800 nm, Opt. Express **14**, 10621–10626 (2006).
[83] V. Wesemann, J. A. L'Huillier, L. K. Friess, P. A. V. Loewis of Menar, G. Bitz, A. Borsutzky, R. Wallenstein, T. Salva, S. Vernay, and D. Rytz, Optical properties of BiB_3O_6 with different phase matching orientations, Appl. Phys. B **84**, 453–458 (2006).
[84] H. R. Xia, L. X. Li, B. Teng, W. Q. Zheng, G. W. Lu, H. D. Jiang, and J. Y. Wang, Raman scattering from bismuth triborate, J. Raman Spectrosc. **33**, 278–282 (2002).
[85] P. Becker and L. Bohaty, Thermal expansion of bismuth borate, Cryst. Res. Technol. **36**, 1175–1180 (2001).

[86] S. Miller, F. Rotermund, G. Xu, F. Noack, V. Panyutin, and V. Petrov, Polarization-dependent nonlinear refractive index of BiB_3O_6, Opt. Mater. **30**, 1469–1472 (2008).
[87] A. Gaydardzhiev, I. Nikolov, I. Buchvarov, V. Petrov, and F. Noack, Ultrabroadband operation of a femtosecond optical parametric generator based on BiB_3O_6 in the near-IR, Opt. Express **16**, 2363–2373 (2008).
[88] D. N. Nikogosyan, Nonlinear Optical Crystals: A Complete Survey (Springer, New York, 2005).
[89] K. Zhang, X. Chen, and X. Wang, Review of study on bismuth triborate (BiB_3O_6) crystal, J. Synth. Cryst. **34**, 438–443 (2005).
[90] E. M. Levin and C. L. McDaniel, The system Bi_2O_3-B_2O_3, J. Am. Ceram. Soc. **45**, 355–360 (1962).
[91] J. Liebertz, Crystal growth from melts of high viscosity, Prog. Crystal Growth Charact. **6**, 361–369 (1983).
[92] J. Liebertz, Metrik und Raumgruppe von BiB_3O_6, Z. Kristallogr. **158**, 319 (1982).
[93] B. Teng, J. Wang, S. Dong, X. Hu, Z. Wang, Z. Shao, and Y. Liu, Determining the optimal growth orientation of BiB_3O_6 crystal, J. Synth. Cryst. **33**, 751–754 (2004).
[94] B. Teng, Z. Wang, H. Jiang, X. Cheng, H. Liu, X. Hu, S. Dong, J. Wang, and Z. Shao, Anisotropic thermal expansion of BiB_3O_6, J. Appl. Phys. **91**, 3618–3620 (2002).
[95] J. Yang and M. Dolg, First-principles electronic structure study of the monoclinic crystal bismuth triborate BiB_3O_6, J. Phys. Chem. **110**, 19254–19263 (2006).
[96] J. Yang and M. Dolg, Computational investigation of the Bi lone-pairs in monoclinic bismuth triborate BiB_3O_6, Phys. Chem. Chem. Phys. **9**, 2094–2102 (2007).
[97] L. Li, B. Teng, S. Dong, L. Xu, C. Li, J. Huang, and J. Wang, Raman spectra of a nonlinear optical crystal: bismuth triborate, J. Funct. Mater. **33**, 673–674 (2002).
[98] A. A. Kaminskii, P. Becker, L. Bohaty, K. Ueda, K. Takaichi, J. Hanuza, M. Maczka, H. J. Eichler, and G. M. A. Gad, Monoclinic bismuth triborate BiB_3O_6 – a new efficient $\chi^{(2)} + \chi^{(3)}$ – nonlinear crystal: multiple stimulated Raman scattering and self-sum-frequency lasing effects, Opt. Commun. **206**, 179–191 (2002).
[99] A. V. Egorysheva, V. I. Burkov, Yu. F. Kargin, V. G. Plotnichenko, and V. V. Koltashev, Vibrational spectra of crystals of bismuth borates, Cryst. Rep. **50**, 127–136 (2005) [transl. from Kristallografiya **50**, 135–144 (2005)].
[100] D. Kasprowicz, T. Runka, M. Szybowicz, P. Ziobrowski, A. Majchrowski, E. Michalski, and M. Drozdowski, Characterization of bismuth triborate single crystal using Brillouin and Raman spectroscopy, Cryst. Res. Technol. **40**, 459–465 (2005).
[101] A. Gössling, T. Möller, W.-D. Stein, P. Becker, L. Bohaty, and M. Grüninger, Phonon modes of monoclinic BiB_3O_6, phys. stat. sol. (b) **242**, R85–R87 (2005).
[102] J. Yang and M. Dolg, First-principles calculation of vibrational frequencies for monoclinic tribismuth borate BiB_3O_6, Z. Kristallogr. **222**, 449–458 (2007).
[103] B. Teng, J. Wang, X. Cheng, Z. Wang, H. Jiang, S. Dong, Y. Liu, and Z. Shao, Growth defects in BiB_3O_6 crystals observed with white-beam synchrotron topography, J. Cryst. Growth **235**, 407–410 (2002).
[104] J. H. Jang, I. H. Yoon, and C. S. Yoon, Cause and repair of optical damage in nonlinear optical crystals of BiB_3O_6, Opt. Mater. **31**, 781–783 (2009).
[105] S. Haussühl, L. Bohaty, and P. Becker, Piezoelectric and elastic properties of the nonlinear optical material bismuth triborate, BiB_3O_6, Appl. Phys. A **82**, 495–502 (2006).
[106] B. Teng, J. Wang, S. Dong, X. Hu, and Z. Wang, Determining the optimum growth orientation of BiB_3O_6 crystal, J. Cryst. Growth **275**, e615–e618 (2005).
[107] M. V. Hobden, Phase-matched second-harmonic generation in biaxial crystals, J. Appl. Phys. **38**, 4365–4372 (1967).
[108] Z. Wang, G. Xu, J. Liu, D. Hu, X. Xu, J. Wang, and Z. Shao, Noncollinear second-harmonic generation in BiB_3O_6, J. Opt. Soc. Am. B **21**, 1348–1353 (2004).
[109] R. Danielius, A. Piskarskas, A. Stabinis, G. P. Banfi, P. Di Trapani, and R. Righini, Traveling-wave parametric generation of widely tunable, highly coherent femtosecond light pulses, J. Opt. Soc. Am. **10**, 2222–2232 (1993).
[110] G. Cerullo and S. De Silvestri, Ultrafast optical parametric amplifiers, Rev. Sci. Instrum. **74**, 1–18 (2003).
[111] A. Birmontas, A. Piskarskas, and A. Stabinis, Dispersion anomalies of tuning characteristics and spectrum of an optical parametric oscillator, Sov. J. Quantum Electron. **13**, 1243–1246 (1983) [transl. from Kvantovaya Elektron. (Moscow) **10**, 1881–1884 (1983)].
[112] X. Liu, D. Deng, M. Li, D. Guo, and Z. Xu, Retracing behavior of the phase-matching angle of nonlinear crystals in optical parametric oscillators, J. Appl. Phys. **74**, 2989–2991 (1993).
[113] V. Petrov, F. Noack, P. Tzankov, M. Ghotbi, M. Ebrahim-Zadeh, I. Nikolov, and I. Buchvarov, High-power femtosecond optical parametric amplification at 1 kHz in BiB_3O_6 pumped at 800 nm, Opt. Express **15**, 556–563 (2007).
[114] M. S. Webb, D. Eimerl, and S. P. Velsko, Wavelength insensitive phase-matched second-harmonic generation in partially deuterated KDP, J. Opt. Soc. Am. B **9**, 1118–1127 (2007).
[115] A. Major, V. Barzda, P. A. E. Piunno, S. Musikhin, and U. J. Krull, An extended cavity diode-pumped femtosecond Yb:KGW laser for applications in optical DNA sensor technology based on fluorescence lifetime measurements, Opt. Express **14**, 5298-5294 (2006).
[116] A. Brenier, I. V. Kityk, and A. Majchrowski, Evaluation of Nd^{3+}-doped BiB_3O_6 (BIBO) as a new potential self-frequency conversion laser crystal, Opt. Commun. **203**, 125–132 (2002).
[117] T. Harimoto, Y. Takeuchi, and M. Fujita, Spectral properties of second-harmonic generation at 800 nm in a BiB_3O_6 crystal, Opt. Express **12**, 811–816 (2004).
[118] M. Ghotbi, M. Ebrahim-Zadeh, A. Majchrowski, E. Michalski, and I. V. Kityk, High-average-power femtosecond pulse generation in the blue using BiB_3O_6, Opt. Lett. **29**, 2530–2532 (2004).
[119] L. E. Nelson, S. B. Fleischer, G. Lenz, and E. P. Ippen, Efficient frequency doubling of a femtosecond fiber laser, Opt. Lett. **21**, 1759–1761 (1996).
[120] M. A. Arbore, M. M. Fejer, M. E. Fermann, A. Hariharan, A. Galvanauskas, and D. Harter, Frequency doubling of femtosecond erbium-fiber soliton lasers in periodically poled lithium niobate, Opt. Lett. **22**, 13–15 (1997).
[121] K. Miyata, F. Rotermund, and V. Petrov, Efficient frequency doubling of a low-power femtosecond Er-fiber laser in BiB_3O_6, IEEE Photon. Technol. Lett (2009), in press.

[122] M. Ghotbi, A. Esteban-Martin, and M. Ebrahim-Zadeh, Ti:Sapphire-pumped Infrared Femtosecond Optical Parametric Oscillator Based on BiB_3O_6, Conference on Lasers and Electro-Optics CLEO'07, Baltimore (MD), USA, 2007, paper JWA31, in: CLEO/QELS Tech. Digest CD-ROM.
[123] A. Esteban-Martin, O. Kokabee, and M. Ebrahim-Zadeh, Efficient, high-repetition-rate, femtosecond optical parametric oscillator tunable in the red, Opt. Lett. **33**, 2650–2652 (2008).
[124] M. Ghotbi, A. Esteban-Martin, and M. Ebrahim-Zadeh, BiB_3O_6 femtosecond optical parametric oscillator, Opt. Lett. **31**, 3128–3130 (2006).
[125] G. M. Gale, M. Cavallari, T. J. Driscoll, and F. Hache, Sub-20-fs tunable pulses in the visible from an 82-MHz optical parametric oscillator, Opt. Lett. **20**, 1562–1564 (1995).
[126] M. Ghotbi, A. Esteban-Martin, and M. Ebrahim-Zadeh, Tunable High-Repetition-Rate Femtosecond Pulse Generation in the Ultraviolet with BiB_3O_6, Conference on Lasers and Electro-Optics CLEO'06, Long Beach (CA), USA, 2006, paper JThC70, in: CLEO/QELS Tech. Digest CD-ROM.
[127] M. Ghotbi, A. Esteban-Martin, and M. Ebrahim-Zadeh, Tunable, high-repetition-rate, femtosecond pulse generation in the ultraviolet, Opt. Lett. **33**, 345–347 (2008).
[128] M. Nisoli, S. De Silvestri, V. Magni, O. Svelto, R. Danielius, A. Piskarskas, G. Valiulis, and A. Varanavicius, Highly efficient parametric conversion of femtosecond Ti:sapphire laser pulses at 1 kHz, Opt. Lett. **19**, 1973–1975 (1994).
[129] U. Emmerichs, S. Woutersen, and H. Bakker, Generation of intense femtosecond optical pulses near 3 µm with a kilohertz repetition rate, J. Opt. Soc. Am. B **14**, 1480–1483 (1997).
[130] D. Eimerl, L. Davis, S. Velsko, E. K. Graham, and A. Zalkin, Optical, mechanical, and thermal properties of barium borate, J. Appl. Phys. **62**, 1968–1983 (1987).
[131] P. Tzankov, M. Roth, Y. Kong, and Z. Sartania, Spatio-Temporal Characterization of the Signal Pulse-Shortening in Type II Optical Parametric Amplifier using BBO and BIBO Crystals, Conference on Lasers and Electro-Optics CLEO'08, San Jose (CA), USA, 2008, paper CTuE3, in: CLEO/QELS Tech. Digest CD-ROM; see also www.quantronixlasers.co .
[132] P. Tzankov and O. Steinkellner, High-Energy Ti:Sapphire Laser System at 1 kHz optimised for Efficient Frequency Conversion, Conference on Lasers and Electro-Optics, CLEO/Europe-EQEC'05, Munich, Germany, 2005, paper CA8-1-TUE, in: CLEO/Europe-EQEC 2005 Conference Digest CD-ROM.
[133] M. Nisoli, S. Stagira, S. De Silvestri, O. Svelto, G. Valiulis, and A. Varanavicius, Parametric generation of high-energy 14.5-fs light pulses at 1.5 µm, Opt. Lett. **23**, 630–632 (1998).
[134] C. Vozzi, G. Cirmi, C. Manzoni, E. Benedetti, F. Calegari, G. Sansone, S. Stagira, O. Svelto, S. De Silvestri, M. Nisoli, and G. Cerullo, High-energy, few-optical-cycle pulses at 1.5 µm with passive carrier-envelope phase stabilization, Opt. Express **14**, 10109–10116 (2006).
[135] E. Riedle, M. Beutter, S. Lochbrunner, J. Piel, S. Schenkl, S. Spörlein, and W. Zinth, Generation of 10 to 50 fs pulses tunable through all of the visible and the NIR, Appl. Phys. B **71**, 457–465 (2000).
[136] C. Manzoni, D. Polli, and G. Cerullo, Two-color pump-probe system broadly tunable over the visible and the near infrared with sub-30 fs temporal resolution, Rev. Sci. Instrum. **77**, 023103-1–9 (2006).
[137] D. Brida, G. Cirmi, C. Manzoni, S. Bonora, P. Villoresi, S. De Silvestri, and G. Cerullo, Sub-two-cycle light pulses at 1.6 µm from an optical parametric amplifier, Opt. Lett. **33**, 741–743 (2008).
[138] D. J. Kane and R. Trebino, Characterization of arbitrary femtosecond pulses using frequency-resolved optical gating, IEEE J. Quantum Electron. **29**, 571–579 (1993).
[139] M. Ghotbi, M. Beutler, V. Petrov, and F. Noack, High energy, short pulse generation in the near-infrared using BIBO, Proc. SPIE **7138**, 71381T-1–6 (2008).
[140] M. Ghotbi, M. Beutler, V. Petrov, A. Gaydardzhiev, and F. Noack, High energy, sub-30 fs near-IR pulses from a broadband optical parametric amplifier based on collinear interaction in BiB_3O_6, Opt. Lett. **34**, 689–691 (2009).
[141] A. Brodeur and S. L. Chin, Ultrafast white-light continuum generation and self-focusing in transparent condensed media, J. Opt. Soc. Am. B **16**, 637–650 (1999).
[142] B. Bareika, A. Birmontas, G. Dikchyus, A. Piskarskas, V. Sirutkaitis, and A. Stabinis, Parametric generation of picosecond continuum in near-infrared and visible ranges on the basis of a quadratic nonlinearity, Sov. J. Quantum Electron. **12**, 1654–1656 (1982) [transl. from Kvantovaya Elektron. (Moscow) **9**, 2534–2536 (1982)].
[143] S. N. Orlov, E. V. Pestryakov, and Yu. N. Polivanov, Optical parametric amplification with bandwidth exceeding an octave, Quantum Electron. **34**, 477–481 (2004) [transl. from Kvantovaya Elektron. (Moscow) **34**, 477–481 (2004)].
[144] M. Tiihonen, V. Pasiskevicius, A. Fragemann, C. Canalias, and F. Laurell, Ultrabroad gain in an optical parametric generator with periodically poled $KTiOPO_4$, Appl. Phys. B **85**, 73–77 (2006).
[145] P. Tzankov, I. Buchvarov, and T. Fiebig, Broadband optical parametric amplification in the near UV-VIS, Opt. Commun. **203**, 107–113 (2002).